UNIVERSITAT POLITÈCNICA DE CATALUNYA
BARCELONATECH
Escola Superior d'Enginyeries Industrial,
Aeroespacial i Audiovisual de Terrassa

BACHELOR FINAL THESIS

Study on the viability of transfer trajectories to the stability region around L4 and L5 Lagrange Points in the Earth-Sun system

Document:

Report

Author:

Sanchez García, Alejandro

Director/Co-director:

Rovira, Adrià / Farrés, Ariadna

Degree:

Bachelor's degree in Aerospace Technology Engineering

Examination session:

Spring, 2023

Abstract

In the present thesis a study is done regarding the viability and optimization of trajectories to get to the stability region around Lagrange points L4 and L5 from the Earth, specifically from periodic orbits around Lagrange points L1 and L2, in the frame of the circular restricted three-body problem of the Earth-Sun system. The trajectory of a spacecraft inside this stability region around L4 and L5 does not leave it for 1000 years or more and without the necessity of any maneuver, i.e. without fuel consumption. Furthermore, this region offers good positions to observe the Sun, and with that to be able to understand and predict the behaviour of possible space weather events, such as solar flares or coronal mass ejections. This is the set of reasons why this stability region is of scientific interest, so that the objective of the present thesis is to study how to get there in the most optimal way possible. Therefore, the unstable invariant manifolds that arise from the periodic orbits around L1 and L2 are the paths to consider as starting points for the transfer trajectories up to L4 and L5, as they take advantage of the dynamic nature of the circular restricted three-body problem. Once the stability region, the types of trajectories around L4 and L5 and the unstable invariant manifolds have been defined, it has been found that it is possible to reach L4 and L5 with a delta-V budget to perform the impulsive maneuvers of around 260 m/s, with times of flight between 8.5 and 9 years. However, it is possible to decrease the time of flight if the delta-V budget is increased, achieving 6-year transfers with delta-V budgets of around 400 m/s or 4-year transfers with delta-V budgets of around 550 m/s. These results show that there is a large variety of trajectories to choose to get to the equilibrium points L4 and L5, all them comparable, in flight times as well as in delta-V budget, to both current and past interplanetary missions. Therefore, it has been seen that there are lots of reasonable possibilities to send a satellite or a set of missions to these stability regions, in order to carry out observations of the Sun and research about space weather without needing to perform station-keeping maneuvers such as in L1 and L2 during the mission period.

Resum

En aquesta tesi es realitza un estudi sobre la viabilitat i optimització de les trajectòries per arribar a la regió d'estabilitat al voltant dels punts de Lagrange L4 i L5 des de la Terra, concretament des d'òrbites periòdiques al voltant dels punts de Lagrange L1 i L2, en el marc del problema circular i restringit dels tres cossos del sistema Terra-Sol. La trajectòria d'un satèl·lit dins de la regió d'estabilitat al voltant de L4 i L5 no l'abandona durant 1000 anys o més i sense la necessitat de cap maniobra, és a dir, sense el consum de combustible. A més, aquesta regió ofereix bones posicions per dur a terme observacions del Sol, i per així poder entendre i predir el comportament de possibles esdeveniments meteorològics espacials, així com erupcions solars o ejeccions de massa coronal. Aquest és el conjunt de raons pel qual aquesta regió d'estabilitat és d'interès científic, de manera que l'objectiu de la tesi és estudiar com arribar-hi de la forma més òptima possible. Així doncs, les varietats invariants inestables que sorgeixen de les òrbites periòdiques al voltant de L1 i L2 són els camins que es consideren com a punts de partida per a les trajectòries de transferència cap a L4 i L5, ja que aprofiten la naturalesa dinàmica del problema circular i restringit dels tres cossos. Un cop definida la regió d'estabilitat, els tipus de trajectòries al voltant de L4 i L5 i les varietats invariants inestables, s'ha trobat que és possible arribar a L4 i L5 amb un pressupost de delta-V per a realitzar les maniobres impulsives d'aproximadament 260 m/s, amb temps de vol d'entre 8.5 i 9 anys. Tot i així, és possible reduir el temps de vol si el pressupost de delta-V es veu incrementat, oferint transferències de 6 anys amb delta-V de 400 m/s o de 4 anys amb delta-V de 550 m/s. Aquests resultats mostren que hi ha una gran varietat de trajectòries a escollir per arribar als punts d'equilibri L4 i L5, tots ells comparables, tant en temps de vol com en pressupost de delta-V, a missions interplanetàries tan actuals com passades. Així doncs, s'ha vist que hi ha moltes possibilitats raonables per enviar un satèl·lit o un conjunt de missions a aquestes regions d'estabilitat, per dur a terme observacions del Sol i recerca sobre meteorologia espacial sense la necessitat de fer maniobres orbitals com s'han de fer a L1 i a L2 durant el període de la missió.

Contents

List of Figures

List of Tables

Acronyms

ACE Advanced Composition Explorer. 8

ASI Agenzia Spaziale Italiana. 65

CME Coronal Mass Ejections. 3, 8

CR3BP Circular Restricted Three-Body Problem. 2–31, 34, 35, 40, 41, 43, 45, 47, 48, 65, III, V

CSA Canadian Space Agency. 8

DSCOVR Deep Space Climate Observatory. 2, 8

ER3BP Elliptical Restricted Three-Body Problem. 6

ESA European Space Agency. 8, 65, 71–73

GGS Global Geospace Science. 8

JPL Jet Propulsion Laboratory. 10, 19, 34, 41, 73, VIII

Juice Jupiter Icy Moons Explorer. 65

JWST James Webb Space Telescope. 2, 8, 65

NASA National Aeronautics and Space Administration. 2, 7, 8, 19, 34, 41, 65, 71–73, V, VIII

NSSDCA NASA Space Science Data Coordinated Archive. 10, 72

PSD Practical Stability Domains. 26, 33–40, 42, 43, 45–63, 66, 69, 70, III–VIII

RPS Region of Practical Stability. 1, 3, 4, 26, 31, 32, 44, 48, 59, 65

RST Roman Space Telescope. 8

SOHO Solar and Heliospheric Observatory Satellite. 2, 8

STEREO Solar TErrestrial RElations Observatory. 8, 72

STM State Transition Matrix. 27–30, 43, 45

Chapter 1

Introduction

1.1 Aim of the project

The aim of the present thesis is to carry out an in-depth study regarding transfer trajectories to the stability region around the Lagrange Points L4 and L5 of the Earth-Sun system, analysing and developing different possible approaches these orbits can take, their trade-offs, pros and cons, and possible optimizations. This project may be considered as a complementary continuation to Aitor Urruticoechea's final thesis *Study and optimization of transfer orbits to the L4 and L5 Lagrange Points of the Earth-Sun system* [1] where he studied and proposed new routes from the Earth's vicinity to periodic orbits around the Lagrange Points L4 and L5. The present thesis also studies trajectories to the Lagrange points L4 and L5, however, instead of going to periodic orbits around these points, the present thesis focuses on getting to the region of practical stability (RPS), named as the *Practical Stability Domains*. These are regions where the trajectory of a spacecraft does not leave the vicinity of L4 or L5 for more than 1000 years with no station keeping required, i.e. no fuel is required [2].

1.2 Justification

For many years, ancients wanted to understand and describe the motion of the planets of the Solar System. After many years of observations and thanks to new mathematical models, the Two-Body problem helped to determine the motion of a planet, a natural or artificial satellite, etc. around another celestial body. However, as the name of the problem states, this mathematical situation only considers the gravitational attraction between two bodies, while neglects the perturbations from others. Then, a more realistic scenario is achieved when considering the gravitational attraction between more than two bodies. If three bodies are considered, the Three-Body problem is obtained. This one is more difficult to solve since it has no analytical solutions, but if one of the three bodies is considered to have an insignificant mass compared with the others (as an artificial satellite compared with a planet or a moon) and the orbits of the two massive bodies around each other are approximated to circular orbits (this is a good approximation for the almost circular planetary

orbits in the Solar System), the Circular Restricted Three-Body Problem (CR3BP) is obtained. From it, some interesting features can be found, and some of them are very useful for research space missions [3] [4].

When considering the CR3BP of the Earth-Sun system (or other pairs of celestial bodies), five equilibrium points, named as the Lagrange points, are found. Lagrange points L1 and L2 have always been of great interest due to their proximity to Earth and to their dynamical properties. In fact, spacecrafts from a large variety of missions have been inserted into periodic and quasi-periodic orbits around these points. L1 offers an uninterrupted view of the Sun, making it a good location to monitor it. It is also a good point from where to image the part of the Earth illuminated by the Sun. Thanks to these properties, missions such as the Solar and Heliospheric Observatory Satellite (SOHO) and the Deep Space Climate Observatory (DSCOVR) are located at L1. Regarding L2, it is a suitable location to observe and study deep space, and it is located directly behind the Earth as seen from the Sun. Missions such as the James Webb Space Telescope (JWST) and the Gaia probe are orbiting L2 [2] [5] [6].

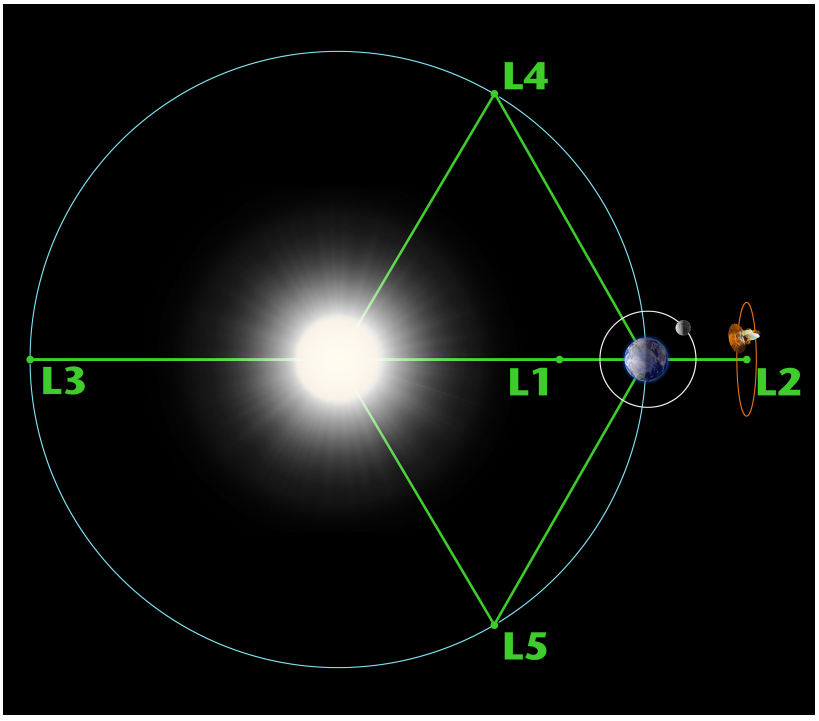

Figure 1.1: Location of the Lagrange points in the Earth-Sun system. Credit: NASA [6].

Nevertheless, both L1 and L2 are unstable points. This means that a spacecraft will tend to abandon its orbit around any of these points if a perturbation is applied. In order to avoid it, the spacecraft needs to do some minor station keeping maneuvers to maintain its orbit, for which some fuel is required. However, the equilibrium characteristics of the Lagrange points make a spacecraft need very reduced amounts of fuel [6] [7].

Although L1 and L2 are locations of great interest as already shown, the present thesis focuses on the Lagrange points L4 and L5. These two points are stable, meaning that a spacecraft will remain in their vicinity over time without the need to perform station keeping maneuvers, i.e. no fuel is required, the reason why these locations are starting to become of interest [2]. And regarding scientific purposes, as L4 and L5

are located ahead and behind the Earth in its orbit, respectively, they offer side views of the surface of the Sun. This could help to better understand how space weather events such as Solar Flares, Coronal Mass Ejections (CME), etc. initiate and propagate through space, also improving space weather event forecasting capabilities. In fact, the speed of CME could be more accurately measured, and a probe at L5 would be able to monitor the part of the Sun's surface that is rotating towards the Earth, helping to predict CME [2]. Some mission concepts have already been thought, as placing simultaneously two satellites, one in L4 and the other in L5, in order to track the evolution of Sun spots, geomagnetic storms, space weather events, etc. [8].

Unfortunately, L4 and L5 are locations difficult to reach due to the long flight times required, as they are very far from Earth [2] [8]. But it is due to the great scientific interest of these points that in the present thesis the most optimal transfers to reach these regions from the Earth's vicinity are going to be studied.

As mentioned earlier, Aitor Urruticoechea has already studied similar transfers from the Earth to L4 and L5 in his thesis [1], but he declared periodic orbits around these points as the destinations. Now, in the present thesis, the RPS of L4 and L5 is the destination. A spacecraft shall get into any of the initial conditions that define the RPS, from the Earth, and without the need of station keeping maneuvers it will be able to maintain itself in the vicinity of L4 or L5 for thousands of years, carrying out its mission. Then, both thesis will be covering two different ways to reach L4 and L5.

Finally, before finishing this section, it is important to note that recent mission concepts and studies are considering solar sail propulsion to reach L4 and L5. This is due to the fact that the vicinity of these points can be reached in a reasonable amount of time when using this propulsion system [2] [8]. However, the present thesis will focus on common high-thrust chemical propulsion systems, i.e. impulsive maneuvers will be considered instead of low-thrust maneuvers (such as solar sails or ionic propulsion), so the obtained results may not be as reasonable as with solar sails.

1.3 Scope

The present thesis will include:

- **Introduction to the CR3BP:** An introductory overview of concepts and its mathematical formulation.
- **Definition of the RPS around L4 and L5:** Finding of the RPS around L4 and L5 by solving numerically the problem and selecting the initial conditions that belong to the RPS.
- **Characterization of the orbits in the RPS:** Understanding and classifying the type of orbits in the RPS by solving the equations of the problem for every initial condition.
- **Selection of the starting orbits around L1 and L2:** The selection and characterization of the optimal orbits around L1 and L2 as the starting points to go to the RPS around L4 and L5.
- **Study of the optimal transfers to the RPS:** The study of the optimal transfers from L1 and L2 or from the Earth to the RPS around L4 and L5, according to the required impulses.

The present thesis will not include:

- The study of the periodic orbits around L4 and L5.
- The study on the return trajectories from L4 and L5 to L1 and L2 or to the Earth.
- The extension of the planar problem to a 3D problem.
- The definition of the characteristics of the spacecraft's propulsion system to perform the impulses or the definition of the spacecraft itself.

The following deliverables will be included:

- Project Charter.
- Final thesis report.
- Budget.
- Appendix or appendices with the programs and codes used.

1.4 Requirements

Some of the basic specifications and constraints to consider for the final solution are described in this section:

- **Implementation of a numerical solver:** A code shall be written in order to propagate in time the initial conditions of the trajectory of a spacecraft, by numerically solving the CR3BP.
- **Validation of the orbits and trajectories:** Every orbit or trajectory shall be checked by making sure that its Jacobi constant does not change with time (the energy of the orbit has to remain constant) if no impulses are performed. Also, for those orbits that are periodic, its periodicity shall also be checked.
- **Identification of the orbits and trajectories:** Every orbit or trajectory shall be well mapped, and the data that represent the position of an object over time shall be accurately saved.
- **Finding the optimal transfers to the RPS:** The optimal transfers to L4 or L5 shall be those with the minimum ΔV required, considering all the impulses that a spacecraft may need to perform, and those that take advantage of the natural dynamics of the system (invariant manifolds).

For all the algorithms and calculations, a minimum precision of 10^{-8} is desired in order to validate all the results.

Chapter 2

Introduction to the CR3BP

In this chapter, some theoretical concepts such as the definition and historical background of the problem as well as its applications are going to be presented in order to familiarize with the CR3BP. The mathematical formulation and other physical features are also going to be presented to understand the dynamics of the problem.

2.1 Background and concepts

For many years, ancients wanted to understand and describe the motion of the planets of the Solar System. Many observations and studies were done, but it was not possible until the publication of the *Philosophiae Naturalis Principia Mathematica* physics book by Isaac Newton back in 1687, where he stated the Newton's law of gravitation. With that and the planetary motion laws postulated by Johannes Kepler earlier in the 17th century, named the Kepler's Laws, the motions of the planets and their moons were finally described [9].

The three laws of planetary motion postulated by Kepler have been useful in order to approximate the motion of a planet, natural or artificial satellite, etc. around another celestial body. However, these laws do not consider the gravitational interactions between various planets, which would result in perturbing the motion of the two studied bodies. Therefore, the Kepler laws are also called the Two-Body problem.

When considering more than two bodies under their gravitational attractions, a more general problem is found, which would result in more accurate motion description if solving it. It is the case of the Three-Body problem, for example, but it is more difficult to solve as analytical solutions can not be obtained [3]. This problem considers the motion described by three gravitational sources such as planets or stars interacting gravitationally between them, and the objective is to find a solution that describes their motion over time [10]. As mathematicians have been trying to solve this Three-Body problem, some interesting solutions to specific cases of the problem have been found [11].

One specific case of the problem is the **Restricted Three-Body Problem**. In this case, of all the three masses that are considered, one of them is supposed to be of negligible mass, enough to not influence the

motion of the other two masses, which can be orbiting around their common center of mass in elliptical orbits (**ER3BP**) or in circular orbits (**CR3BP**). This could be associated to the case of a satellite moving around the Earth-Moon or Earth-Sun systems [4].

In the present thesis, the CR3BP is going to be the background of all statements. Although considering that the third mass is extremely small compared to the other two masses and that these two masses orbit their common center of mass in circular orbits seem to be restrictive assumptions, this problem is a good approximation for most important physical situations: the mass of a satellite can be neglected in front of the masses of natural satellites, planets or stars, and most of the planetary orbits around the Sun can be considered to be approximately circular, as their eccentricities are almost 0 [12]. For instance, the orbital eccentricities of Venus, Earth, Jupiter, Saturn, Uranus and Neptune are all less than 0.06, while those of Mercury and Mars are of 0.206 and 0.094, respectively [13]. The circular assumption may not be a good approximation for Mercury, though.

In general, this CR3BP problem was firstly studied by Leonhard Euler and Joseph-Louis Lagrange, who found three explicit formulas for families of orbits in 1767 and two in 1772, respectively. Euler also introduced a synodic (rotating) coordinate system in 1772, and Carl Gustav Jakob Jacobi discovered an integral of motion in this coordinate system back in 1836, known as the Jacobi integral. Also, it is important to state that in 1890 Henri Poincaré discovered chaotic dynamics. With that, he claimed that all the solutions to the Three-Body problem can not be known with the same level of detail as obtained with the solutions to the Two-Body problem, but that with numerical integration finite segments of approximate orbits can be nonetheless obtained, which is useful when planning space missions [4] [11].

In the CR3BP some points exist in space where objects tend to stay there. In these points, the gravitational attraction of the two large masses equals the centripetal force required by the third small mass to move with them. These are the Lagrange points, named after the Italian-French mathematician Joseph-Louis Lagrange, as he firstly theorised the existence of these regions of space back in 1772. The gravitational attraction of the two large masses produce regions of both attraction and repulsion in these points. Therefore, satellites need reduced amounts of fuel in order to remain in these positions, moving in a relative position with respect to both large bodies [6] [7].

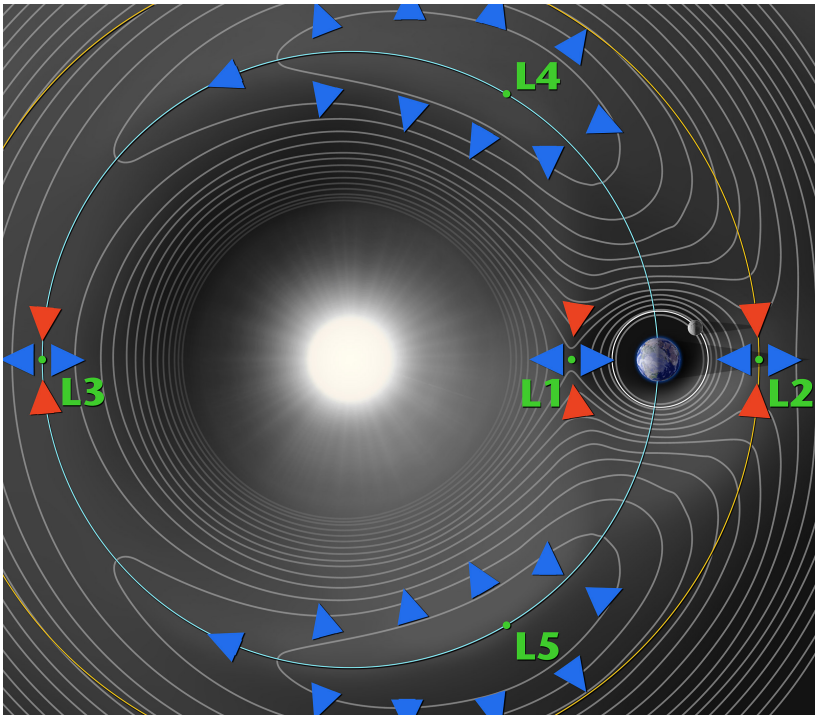

Figure 2.1: Gravity potential of the Earth-Sun system. Credit: NASA [6]. Lagrange points L4 and L5 are located in hilltops, while L1, L2 and L3 are located in saddles. Blue arrows show repulsion forces and red arrows show attraction forces [14].

In fact, in a system of two large masses, a third small mass can orbit in a pattern with them in five different Lagrange points. From these five points, the first three ones (L1, L2 and L3) are located along the line that connects the two large masses and are unstable, meaning that spacecrafts tend to abandon their orbit around the equilibrium point if a perturbation is applied. The other two points (L4 and L5) are located in forward and backward positions relative to the orbit of the second largest body around the first largest body, forming two equilateral triangles with the two large masses at their vertices. These equilibrium points, in difference with the first three ones, are stable if the mass ratio between the largest and the second largest masses exceeds 24.96, meaning that a spacecraft will remain in the vicinity of L4 or L5. When a spacecraft falls off from them, it gets more and more speed, gaining the effect of the Coriolis force. This force sends the satellite into a stable orbit around L4 or L5. This stability condition is satisfied for the Earth-Sun system, the Earth-Moon system and other pairs of celestial bodies in the Solar System. Objects orbiting the Lagrange points L4 or L5 are called Trojans and, in fact, the first Trojan asteroids were found in 1906 in the Jupiter-Sun system, confirming the theory of these Lagrange points [6] [7].

2.2 Space applications

As mentioned before, there are five Lagrange points for every pair of celestial bodies in the Solar System. In this report, the Lagrange points of the Earth-Sun system are the ones to be studied.

Lagrange point L1 is located at approximately 1.5 million km [7] from the Earth in direction towards the Sun. Therefore, it offers an uninterrupted view of the Sun and it is a good location to monitor it. In fact, the solar

wind reaches L1 about an hour before reaching Earth [5]. The SOHO is located at L1 [6]. The DSCOVR is also located at L1, as it is a good position to image the sunlit part of the Earth, too. Other current spacecrafts at L1 are the Advanced Composition Explorer (ACE), which is studying matter comprising energetic particles from the solar wind among others, and the Global Geospace Science (GGS) WIND satellite, which is studying the radio waves and plasma in the solar wind and in the Earth's magnetosphere [15] [16].

Lagrange point L2 is located also at approximately 1.5 million km [7] from the Earth, but in the opposite direction from L1 (i.e. radially outwards). Then, it offers a suitable location to observe and study deep space, as it is directly behind the Earth as seen from the Sun. As a satellite at L2 does not have to orbit the Earth, it does not sweep in and out of the planet's shadow. Then, all the effects the spacecraft suffer from heating up and cooling down that could distort it are avoided, making L2 an optimal position to observe the Universe [5]. All of that is performed while staying in a fixed position relative to the Earth, making the communications between Earth ground stations and the satellite easier [6]. L2 is home of the NASA/ESA/CSA JWST and the ESA Gaia probe (a mission to measure positions, distances and motions of stars to construct the most precise 3D space catalogue ever [17]), and it will be the future home of the ESA Euclid mission (to study dark energy and dark matter), the ESA PLATO mission (to study rocky exoplanets), the ESA ARIEL mission (to study exoplanets atmospheres) and the NASA RST (an infrared space telescope designed to study dark energy, exoplanets, galaxies, etc. [18]), among others [15].

Lagrange point L3 is approximately located where the Earth will be in half its orbital period, i.e. half a year, so it is in an opposite location to the Earth, being in a permanently hidden position by the Sun. Although it may be useful to observe the far side of the Sun and events not visible from Earth, no known objects are located there [5] [6] [15].

And finally, Lagrange points L4 and L5 are 60° ahead and behind the Earth, respectively, in the Earth's orbit around the Sun [7]. As mentioned earlier, for the Earth-Sun system these Lagrange points are stable and resistant to gravitational perturbations. Therefore, dust and asteroids accumulate in these regions, and a spacecraft is able to orbit L4 or L5 without drifting away into interplanetary space [5]. Besides Trojan asteroids discovered orbiting around L4 and L5, the Solar TErrestrial RElations Observatory - Ahead (STEREO A) and Behind (STEREO B) passed near these points back in 2009, respectively, imaging their regions to try to find material left over from the origins of the Solar System [19] while performing their mission of monitoring the Sun and solar phenomena, such as CME, in heliocentric orbits gradually pulling them farther ahead and behind the Earth, respectively [20]. Also, the planned ESA Vigil mission to monitor space weather [21] is designed to be located at L5, the trailing Lagrange point, allowing the Vigil spacecraft to predict arrival times at Earth and any effect from solar flares, CME, geomagnetic storms, etc. [15].

These uses and applications that can be carried out at the Lagrange points L4 and L5 and the fact that both locations are stable, meaning that a spacecraft can remain in their vicinity without the need to perform fuel-requiring maneuvers, are making them locations of interest. However, L4 and L5 are locations difficult to reach from the Earth, as they are far away and long flight times are required to get there [2] [8]. These are the reasons to study and optimize the transfer trajectories up to these equilibrium points from the Earth.

2.3 Equations of motion

From a mathematical point of view, it is interesting to start describing the problem by defining its equations of motion.

2.3.1 Problem restrictions

As stated previously, the CR3BP focuses on two main restrictions [14] [22]:

- **Restricted problem:** One of the three masses is assumed to be negligibly small compared with the other two masses, which are called the primary bodies (major primary m_1 and minor primary m_2):

$$m << m_2 < m_1$$

  Then, the small mass m does not have any effect on the motion of the primary bodies.

- **Circular problem:** The primary masses are rotating on circular orbits around their common center of mass or barycenter, with a constant angular velocity of:

$$\omega = \sqrt{\frac{G(m_1 + m_2)}{d^3}} = constant \tag{2.1}$$

  Where $d = r_{12} = constant$ is the mutual distance between the primaries.

2.3.2 Synodic reference frame

In order to obtain the equations of motion, a non-inertial reference frame xyz is considered. This reference frame co-rotates with the system of the two primaries at the constant angular velocity ω of the system. Its origin is located at the center of mass or barycenter G of the two primaries, with the x-axis pointing towards m_2, the y-axis lying on the orbital plane and the z-axis being perpendicular to both of them and pointing towards the direction of the rotation, completing the right-handed reference system (see Figure 2.2) [14] [22].

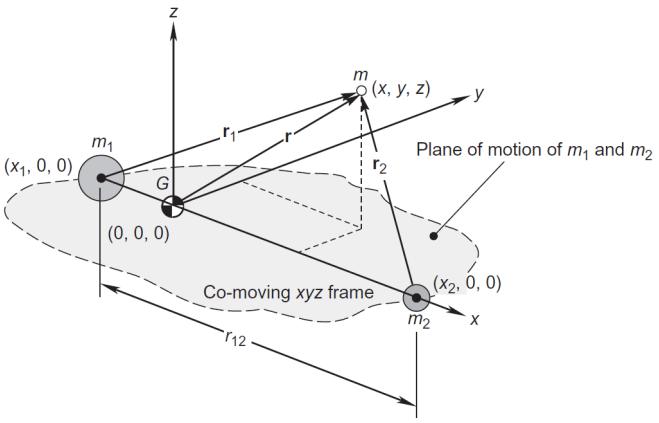

Figure 2.2: Synodic reference frame. Credit: Curtis, H. [22]

In this rotating frame, the primary masses m_1 and m_2 seem to be at rest. Then, the force of gravity acting on each one is balanced by the centrifugal force that is necessary to maintain its circular orbit around the system's barycenter [22].

2.3.3 Dimensionless variables

When defining the equations of motion of the problem it is usually common to do it in dimensionless variables. Therefore, the masses of the two primaries can be normalized by their total mass $M = m_1 + m_2$, which is chosen as the unit of mass, in the following way [14] [23]:

$$\mu := \frac{m_2}{m_1 + m_2}$$
$$1 - \mu = \frac{m_1}{m_1 + m_2}$$

For the Earth-Sun system, m_1 refers to the Sun, while m_2 to the Earth. According to NSSDCA's fact sheets:

$$m_1 = 1.9885 \times 10^{30} \text{ kg [24]}$$
$$m_2 = 5.9722 \times 10^{24} \text{ kg [25]}$$

Then, it would result: $\mu = 3.00336 \times 10^{-6}$.

However, the normalized mass μ from JPL [26] is the one that is going to be used in the following sections of this study that require numerical calculations:

$$\boxed{\mu = 3.05420 \times 10^{-6}} \tag{2.2}$$

The differences with the previous value may be due to JPL considering other mass sources for the parameter in order to make it more accurate to represent the Earth-Sun system.

Then, all distances can also be normalized with the unit of length: the constant mutual distance between the primaries $d = r_{12}$ [23]. Again, this value is taken from JPL [26]:

$$\boxed{d^* = r_{12} = 149.597871 \times 10^6 \; km}$$

And finally, the time can also be normalized. The unit of time is that which makes the orbital period T of both primary masses around their barycenter be 2π [23]:

$$\boxed{t^*} = \frac{T}{2\pi} = \boxed{5.022635 \times 10^6 \; s}$$

This value is also taken from JPL data [26].

All this makes the angular velocity of the system (Equation (2.1)) become unity, and from that, it turns out

that the universal constant of gravitation also becomes $G = 1$ [23] [27].

And finally, it is important to know the coordinates where the two primaries are located in dimensionless units: x_1 and x_2. The expression of the barycenter's position of a system of two masses is the following:

$$\mathbf{R_G} = \frac{m_1\mathbf{R_1} + m_2\mathbf{R_2}}{m_1 + m_2} \tag{2.3}$$

It is known that, from the barycenter's position (see Figure 2.2):

$$\mathbf{R_G} = (0\ 0\ 0)^T \qquad \mathbf{R_1} = (x_1\ 0\ 0)^T \qquad \mathbf{R_2} = (x_2\ 0\ 0)^T$$

Then, applying Equation (2.3):

$$m_1 x_1 + m_2 x_2 = 0 \tag{2.4}$$

And as the mutual distance between the primaries is r_{12}, the following relation can be found:

$$x_2 - x_1 = r_{12} \tag{2.5}$$

With Equations (2.4) and (2.5) and normalizing the distances with d^*, the following coordinates are found:

$$x_1 = -\mu$$
$$x_2 = 1 - \mu$$

Now that both primaries m_1 and m_2 are positioned in the synodic reference frame, the equations of motion of the third negligibly small mass m moving due to the gravitational fields of m_1 and m_2 can be found.

2.3.4 Obtaining the equations

With the help of Figure 2.2, it can be seen that the position vectors of the secondary mass m relative to the primaries m_1 and m_2 are the following. The position vector of m relative to the barycenter is also shown [22]:

$$\mathbf{r_1} = \begin{pmatrix} x - x_1 \\ y \\ z \end{pmatrix} = \begin{pmatrix} x + \mu \\ y \\ z \end{pmatrix} \qquad \mathbf{r_2} = \begin{pmatrix} x - x_2 \\ y \\ z \end{pmatrix} = \begin{pmatrix} x + \mu - 1 \\ y \\ z \end{pmatrix} \qquad \mathbf{r} = \begin{pmatrix} x \\ y \\ z \end{pmatrix} \tag{2.6}$$

As the synodic reference frame is rotating with an angular velocity $\mathbf{\Omega} = \omega\,\hat{\mathbf{k}}$, the velocity vector of m relative to inertial space is:

$$\dot{\mathbf{r}} = \mathbf{v_G} + \mathbf{\Omega} \times \mathbf{r} + \mathbf{v_{rel}} \tag{2.7}$$

Where $\mathbf{v_G}$ is the inertial velocity vector of the barycenter and $\mathbf{v_{rel}}$ is the vector of the relative velocity of m with respect to the rotating reference frame:

$$\mathbf{v_{rel}} = (\dot{x}\ \dot{y}\ \dot{z})^T \tag{2.8}$$

Then, the absolute acceleration of m relative to inertial space, accounting for the angular velocity of the rotating frame, has to consider the tangential and normal acceleration terms, the Coriolis term and the relative term:

$$\ddot{\mathbf{r}} = \mathbf{a_G} + \dot{\mathbf{\Omega}} \times \mathbf{r} + \mathbf{\Omega} \times (\mathbf{\Omega} \times \mathbf{r}) + 2\mathbf{\Omega} \times \mathbf{v_{rel}} + \mathbf{a_{rel}} \tag{2.9}$$

Where $\mathbf{a_G}$ is the inertial acceleration of the barycenter. For a couple of bodies, the velocity of their barycenter $\mathbf{v_G}$ is constant, so $\mathbf{a_G} = 0$. Then, as seen before, the angular velocity of the system in the CR3BP is constant, so the angular acceleration $\dot{\mathbf{\Omega}} = 0$. Then, the last equation is simplified to the following:

$$\ddot{\mathbf{r}} = \mathbf{\Omega} \times (\mathbf{\Omega} \times \mathbf{r}) + 2\mathbf{\Omega} \times \mathbf{v_{rel}} + \mathbf{a_{rel}} \tag{2.10}$$

Where $\mathbf{a_{rel}}$ is the relative acceleration of m measured with respect to the rotating reference frame, as with $\mathbf{v_{rel}}$:

$$\mathbf{a_{rel}} = (\ddot{x}\ \ddot{y}\ \ddot{z})^T \tag{2.11}$$

Substituting the angular velocity, the position vector and the relative velocity and acceleration vectors into Equation (2.10), the following is obtained:

$$\ddot{\mathbf{r}} = (\omega\,\hat{\mathbf{k}}) \times \Big[(\omega\,\hat{\mathbf{k}}) \times (x\,\hat{\mathbf{i}} + y\,\hat{\mathbf{j}} + z\,\hat{\mathbf{k}})\Big] + 2\,(\omega\,\hat{\mathbf{k}}) \times (\dot{x}\,\hat{\mathbf{i}} + \dot{y}\,\hat{\mathbf{j}} + \dot{z}\,\hat{\mathbf{k}}) + (\ddot{x}\,\hat{\mathbf{i}} + \ddot{y}\,\hat{\mathbf{j}} + \ddot{z}\,\hat{\mathbf{k}})$$

Operating and rearranging terms, the inertial acceleration vector yields [22]:

$$\ddot{\mathbf{r}} = \begin{pmatrix} \ddot{x} - 2\omega\dot{y} - \omega^2 x \\ \ddot{y} + 2\omega\dot{x} - \omega^2 y \\ \ddot{z} \end{pmatrix} \tag{2.12}$$

Now that the inertial acceleration vector is known, it can be related with the Newton's second law for the secondary mass m. As this mass is moving due to the gravitational fields of m_1 and m_2, the next relation can be stated [22]:

$$m\ddot{\mathbf{r}} = \mathbf{F_1} + \mathbf{F_2} \tag{2.13}$$

Where $\mathbf{F_1}$ and $\mathbf{F_2}$ are the gravitational forces that the secondary mass receives from the first and second primaries, respectively:

$$\mathbf{F_1} = -\frac{Gm_1 m}{r_1^2}\mathbf{u_{r_1}} = -\frac{\mu_1 m}{r_1^3}\mathbf{r_1} \qquad \text{with } \mu_1 = Gm_1 \tag{2.14}$$

$$\mathbf{F_2} = -\frac{Gm_2 m}{r_2^2}\mathbf{u_{r_2}} = -\frac{\mu_2 m}{r_2^3}\mathbf{r_2} \qquad \text{with } \mu_2 = Gm_2 \tag{2.15}$$

Replacing these forces into Equation (2.13), the inertial acceleration vector yields:

$$\ddot{\mathbf{r}} = -\frac{\mu_1}{r_1^3}\mathbf{r_1} - \frac{\mu_2}{r_2^3}\mathbf{r_2} \tag{2.16}$$

Finally, replacing Equation (2.12) into the left-hand side of Equation (2.16) and $\mathbf{r_1}$ and $\mathbf{r_2}$ from Equation (2.6) into the right-hand side of Equation (2.16), it yields:

$$\begin{pmatrix} \ddot{x} - 2\omega\dot{y} - \omega^2 x \\ \ddot{y} + 2\omega\dot{x} - \omega^2 y \\ \ddot{z} \end{pmatrix} = -\frac{\mu_1}{r_1^3}\begin{pmatrix} x - x_1 \\ y \\ z \end{pmatrix} - \frac{\mu_2}{r_2^3}\begin{pmatrix} x - x_2 \\ y \\ z \end{pmatrix}$$

Considering the normalized variables presented in section 2.3.3, it is known that:

$$\boxed{m_1 \rightarrow 1-\mu} \qquad \boxed{m_2 \rightarrow \mu}$$

$$\boxed{r_{12} = 1} \qquad \boxed{\omega = 1} \qquad \boxed{G = 1}$$

$$\boxed{\mu_1 = Gm_1 = 1-\mu} \qquad \boxed{\mu_2 = Gm_2 = \mu}$$

Then:

$$\begin{pmatrix} \ddot{x} - 2\dot{y} - x \\ \ddot{y} + 2\dot{x} - y \\ \ddot{z} \end{pmatrix} = -\frac{1-\mu}{r_1^3}\begin{pmatrix} x + \mu \\ y \\ z \end{pmatrix} - \frac{\mu}{r_2^3}\begin{pmatrix} x + \mu - 1 \\ y \\ z \end{pmatrix} \tag{2.17}$$

Where r_1 and r_2 are the distances from the secondary mass m to the primary body 1 and 2, respectively:

$$r_1 = \sqrt{(x - x_1)^2 + y^2 + z^2} = \sqrt{(x + \mu)^2 + y^2 + z^2} \tag{2.18}$$

$$r_2 = \sqrt{(x - x_2)^2 + y^2 + z^2} = \sqrt{(x + \mu - 1)^2 + y^2 + z^2} \tag{2.19}$$

From Equation (2.17), the three **scalar equations of motion** of the CR3BP are obtained:

$$\ddot{x} - 2\dot{y} - x = -\frac{1-\mu}{r_1^3}(x+\mu) - \frac{\mu}{r_2^3}(x+\mu-1) \tag{2.20}$$

$$\ddot{y} + 2\dot{x} - y = -\frac{1-\mu}{r_1^3}y - \frac{\mu}{r_2^3}y \tag{2.21}$$

$$\ddot{z} = -\frac{1-\mu}{r_1^3}z - \frac{\mu}{r_2^3}z \tag{2.22}$$

These equations of motion are coupled via the r_i^{-3} $(i = 1, 2)$ terms, which make them impossible to be solved analytically [14]. Then, numerical integration will be used to solve the equations.

Also, it is important to note that in the present thesis only the planar case of the problem is going to be considered, and not the three-dimensional case. Notice that if $z = 0$, the previous equations of motion lead to the condition that $\ddot{z} = 0$. As there is no acceleration in the z-axis, if the initial velocity in this axis is also $\dot{z} = 0$, then the motion is contained in the x-y plane ($z = 0$) and governed by the equations of motion (2.20) and (2.21).

It is important to note that the previous procedure and discussions to obtain the equations of motion have been extracted from both Ulrich Walter [14] and Howard D. Curtis [22] books.

2.4 Jacobi's integral

Although the equations of motion can not be analytically solved, they can be integrated once [14]. In order to do that, the equations of motion (2.20), (2.21) and (2.22) should be multiplied by their respective velocity components $\dot{x}$, $\dot{y}$ and $\dot{z}$ [22]:

$$\ddot{x}\dot{x} - 2\dot{y}\dot{x} - x\dot{x} = -\frac{1-\mu}{r_1^3}(x\dot{x} + \mu\dot{x}) - \frac{\mu}{r_2^3}(x\dot{x} + \mu\dot{x} - \dot{x})$$

$$\ddot{y}\dot{y} + 2\dot{x}\dot{y} - y\dot{y} = -\frac{1-\mu}{r_1^3}y\dot{y} - \frac{\mu}{r_2^3}y\dot{y}$$

$$\ddot{z}\dot{z} = -\frac{1-\mu}{r_1^3}z\dot{z} - \frac{\mu}{r_2^3}z\dot{z}$$

Summing the left-hand and right-hand sides of the previous equations yields:

$$\ddot{x}\dot{x} + \ddot{y}\dot{y} + \ddot{z}\dot{z} - x\dot{x} - y\dot{y} = -\left(\frac{1-\mu}{r_1^3} + \frac{\mu}{r_2^3}\right)(x\dot{x} + y\dot{y} + z\dot{z}) - \mu\left(\frac{1-\mu}{r_1^3} + \frac{\mu-1}{r_2^3}\right)\dot{x}$$

Rearranging terms:

$$\ddot{x}\dot{x} + \ddot{y}\dot{y} + \ddot{z}\dot{z} - x\dot{x} - y\dot{y} = -\frac{1-\mu}{r_1^3}(x\dot{x} + y\dot{y} + z\dot{z} + \mu\dot{x}) - \frac{\mu}{r_2^3}(x\dot{x} + y\dot{y} + z\dot{z} - (1-\mu)\dot{x}) \tag{2.23}$$

It is important to note the following [22]:

$$\ddot{x}\dot{x} + \ddot{y}\dot{y} + \ddot{z}\dot{z} = \frac{1}{2}\frac{d}{dt}(\dot{x}^2 + \dot{y}^2 + \dot{z}^2) = \frac{1}{2}\frac{d}{dt}(v^2) \tag{2.24}$$

And also that [22]:

$$x\dot{x} + y\dot{y} = \frac{1}{2}\frac{d}{dt}(x^2 + y^2) \tag{2.25}$$

Where v is the modulus of the velocity of the mass m, measured with respect to the rotating reference frame.

Then, the distances from the secondary mass to the primary masses are already known (see Equations (2.18) and (2.19)), and from them the following relations can be found [22]:

$$\frac{d}{dt}\left(\frac{1}{r_1}\right) = -\frac{1}{r_1^3}(x\dot{x} + y\dot{y} + z\dot{z} + \mu\dot{x}) \tag{2.26}$$

$$\frac{d}{dt}\left(\frac{1}{r_2}\right) = -\frac{1}{r_2^3}(x\dot{x} + y\dot{y} + z\dot{z} - (1-\mu)\dot{x}) \tag{2.27}$$

Replacing Equations (2.24), (2.25), (2.26) and (2.27) into Equation (2.23), it yields:

$$\frac{1}{2}\frac{d}{dt}(v^2) = \frac{1}{2}\frac{d}{dt}(x^2 + y^2) + (1-\mu)\frac{d}{dt}\left(\frac{1}{r_1}\right) + \mu\frac{d}{dt}\left(\frac{1}{r_2}\right)$$

$$\frac{d}{dt}\left[\frac{1}{2}v^2 - \frac{1}{2}(x^2 + y^2) - \frac{1-\mu}{r_1} - \frac{\mu}{r_2}\right] = 0$$

The indefinite integral of this last equation is the following expression:

$$\boxed{\frac{1}{2}v^2 - \frac{1}{2}(x^2 + y^2) - \frac{1-\mu}{r_1} - \frac{\mu}{r_2} = C} \tag{2.28}$$

This is called the **Jacobi's integral**, and the integration constant C is called the **Jacobi constant**. This shows, in normalized variables, that the energy of the secondary mass m is conserved, as C can be interpreted as its total energy relative to the synodic reference frame [14] [22]. In fact, the first term on the left of Equation (2.28) represents the secondary body's kinetic energy, while the third and fourth terms represent the gravitational potential energies relative to the two primaries. Regarding the second term on the left, it can be interpreted as the rotational energy of the secondary mass, i.e. the potential energy of the centrifugal force generated by the rotating reference frame [14] [22].

Next, and for future purposes, it is interesting to define the **effective potential** [14]:

$$\boxed{U := \frac{1}{2}(x^2 + y^2) + \frac{1-\mu}{r_1} + \frac{\mu}{r_2} > 0} \tag{2.29}$$

This **positive** effective potential has an important shape regarding stability and energy issues related to the

libration points. This shape can be seen in Figure 2.3, obtained from Koon, W. et al. book [23].

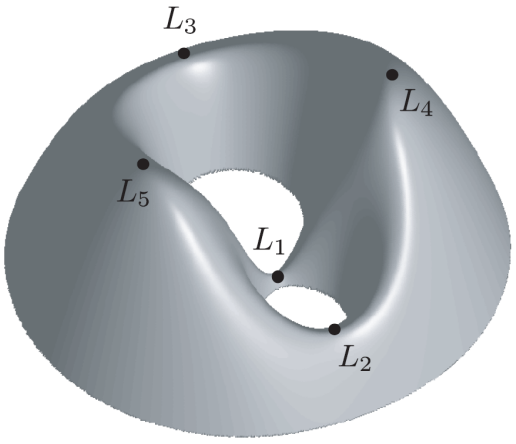

Figure 2.3: Effective potential shape and libration points in the CR3BP. Credit: Koon, W. et al. [23]

With this effective potential, Jacobi's integral can be redefined as [14]:

$$\boxed{\frac{1}{2}v^2 - U = C} \tag{2.30}$$

Some features can be observed in Figure 2.3. First of all, near both m_1 and m_2 a potential well is found. Then, far away from the primaries is where the centrifugal force dominates (first term in Equation (2.29)), so another potential well is found. And finally, there are also five locations where the slope of the effective potential is zero: three saddle points (L1, L2 and L3) and two points in hilltops (L4 and L5). While Lagrange points L4 and L5 are located in hilltops with repulsion forces in all directions (see Figure 2.1), Lagrange points L1, L2 and L3 have destabilizing forces in the direction of the x-axis but attractive forces in the perpendicular direction, leading to the shape of a saddle. Notice that if a spacecraft is perfectly stopped in the exact location of a Lagrange point, it will not move: they are equilibrium points because the sum of the gravitational force vectors and the centrifugal force vector is 0 [28].

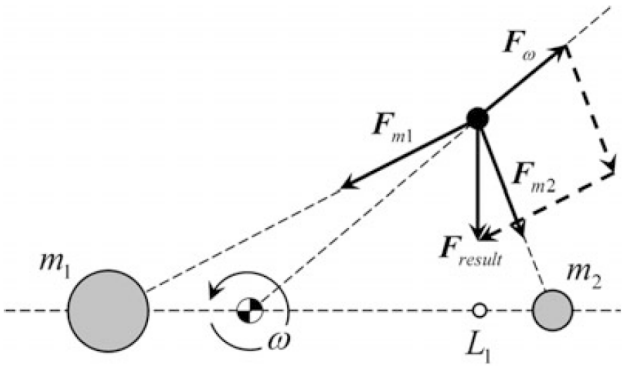

Figure 2.4: Gravitational forces F_{m1} and F_{m2} and the centrifugal force F_ω leading to a resultant restoring force F_{result} acting on a body near L1. Credit: Walter, U. [14]

However, considering the dynamic evolution of motion around these libration points, L1, L2 and L3 turn to be

dynamically unstable, i.e. a satellite will eventually drift away after being subjected to a small perturbation; while L4 and L5 turn to be dynamically stable, i.e. a satellite will remain near L4 or L5 after suffering a perturbation [28]. As already explained in Section 2.1, this dynamically stable condition for both L4 and L5 is only satisfied if the mass ratio between the primaries exceeds $m_1/m_2 = 24.96$ (or $\mu \leq 0.03852$). The stability itself is achieved thanks to the Coriolis force that acts on a body when increasing its velocity, which sends the satellite into a stable orbit around these equilibrium points [6].

2.5 Location of the Lagrange points

Once it is known that there are five points where equilibrium can be reached in the synodic reference system, it is interesting to find their exact locations. Equilibrium is understood as a position where a test mass m would have zero velocity as well as zero acceleration. In the synodic reference frame, m would appear to be at rest with respect to the primaries m_1 and m_2, and, therefore, permanently staying in the equilibrium point [22]. Then, the conditions to impose in order to find the location of the equilibrium points are both zero relative velocity and zero relative acceleration with respect to the rotating reference frame:

$$\dot{x} = \dot{y} = \dot{z} = \ddot{x} = \ddot{y} = \ddot{z} = 0$$

Replacing these conditions into the equations of motion (2.20), (2.21) and (2.22), the following expressions are found:

$$-x = -\frac{1-\mu}{r_1^3}(x+\mu) - \frac{\mu}{r_2^3}(x+\mu-1) \tag{2.31}$$

$$-y = -\frac{1-\mu}{r_1^3}y - \frac{\mu}{r_2^3}y \tag{2.32}$$

$$0 = -\frac{1-\mu}{r_1^3}z - \frac{\mu}{r_2^3}z \tag{2.33}$$

The first result is obtained directly from Equation (2.33):

$$\left(\frac{1-\mu}{r_1^3} + \frac{\mu}{r_2^3}\right) z = 0 \tag{2.34}$$

It is clear that both terms $\frac{1-\mu}{r_1^3}$ and $\frac{\mu}{r_2^3}$ are always positive. Then, the only way to satisfy Equation (2.34) is by imposing $\mathbf{z = 0}$. This means that the equilibrium points are located in the x-y plane, i.e. the orbital plane [22].

Then, two different paths can be followed in order to solve Equations (2.31) and (2.32). The first one considers that $y \neq 0$ in Equation (2.32), so the next relation can be stated in this case:

$$1 = \frac{1-\mu}{r_1^3} + \frac{\mu}{r_2^3} \tag{2.35}$$

This can be replaced in Equation (2.31):

$$x = (x+\mu)\left(\frac{1-\mu}{r_1^3}+\frac{\mu}{r_2^3}\right)-\frac{\mu}{r_2^3} \qquad \rightarrow \qquad x = x+\mu-\frac{\mu}{r_2^3} \qquad \rightarrow \qquad 1 = \frac{1}{r_2^3} \tag{2.36}$$

With this relation in Equation (2.36) and Equation (2.35), it can be seen that $r_1 = r_2 = 1$. Recovering Equations (2.18) and (2.19) and imposing this relation and that $z = 0$, the following expressions are obtained:

$$r_1 = 1 = \sqrt{(x+\mu)^2+y^2} \tag{2.37}$$

$$r_2 = 1 = \sqrt{(x+\mu-1)^2+y^2} \tag{2.38}$$

Equating them, the system of equations can be solved:

$$(x+\mu)^2+y^2 = (x+\mu-1)^2+y^2$$
$$(x+\mu)^2 = (x+\mu-1)^2$$
$$x^2+2\mu x+\mu^2 = x^2+2(\mu-1)x+\mu^2-2\mu+1$$
$$0 = -2x-2\mu+1$$

From where the following result is obtained:

$$\boxed{x = -\mu+\frac{1}{2}} \tag{2.39}$$

And replacing it in Equation (2.37):

$$\boxed{y = \pm\frac{\sqrt{3}}{2}} \tag{2.40}$$

Equations (2.39) and (2.40) show the dimensionless coordinates of **Lagrange points L4 and L5**, the equilateral libration points, as they form two equilateral triangles with the two primaries m_1 and m_2, as can be seen with $r_1 = r_2 = 1$ and knowing that $r_{12} = 1$ when normalized, too [22].

Next, the other path to follow when solving Equations (2.31) and (2.32) is going to be considered, which imposes now that $y = 0$ in Equation (2.32) (this equation is satisfied) [22]. Replacing $y = 0$ as well as $z = 0$ in the expressions of r_1 (2.18) and r_2 (2.19), the following expressions are obtained:

$$r_1 = |x+\mu| \tag{2.41}$$

$$r_2 = |x+\mu-1| \tag{2.42}$$

Substituting Equations (2.41) and (2.42) into Equation (2.31), it yields:

$$\boxed{\frac{1-\mu}{|x+\mu|^3}(x+\mu)+\frac{\mu}{|x+\mu-1|^3}(x+\mu-1)-x = 0} \tag{2.43}$$

This is a function that depends on μ and x, $f(\mu, x)$, which satisfies the condition of equilibrium point along the x-axis (for $y = z = 0$) when $f(\mu, x) = 0$ [22]. Then, for a given μ, the idea is to find the roots of this function, which are three and are the locations of the collinear **Lagrange points L1, L2 and L3** [22]. This problem can be solved by means of a bisection method or similars.

NASA's JPL [26], as already stated in (2.2), gives a $\mu = 3.05420 \times 10^{-6}$. It also gives, according to this μ, the locations of the three collinear Lagrange points, as well as of the two equilateral Lagrange points, which match the expressions (2.39) and (2.40).

Lagrange point	x	y	z
L1	0.989970	0.0	0.0
L2	1.010090	0.0	0.0
L3	-1.000001	0.0	0.0
L4	0.499997	0.866025	0.0
L5	0.499997	-0.866025	0.0

Table 2.1: Coordinates of the five libration points given by JPL for the Earth-Sun system [26].

2.6 Energy and Hill's region

In the CR3BP Jacobi's integral (Equation (2.28)) is a useful equation to understand how the motion of the test mass m is restricted, thus offering information about its motion, something that can not be achieved in the more general n-body problem [14]. In fact, the Jacobi constant is to the CR3BP what the specific total energy is to the two-body problem. The latter restricts the orbital motion and also defines types of orbits that meet the same characteristics: elliptic, parabolic and hyperbolic orbits [14].

Any trajectory in the CR3BP is included in an invariant manifold. It represents the phase space of the dynamics of the system with that Jacobi constant, and as it has to remain constant, i.e. energy is conserved, any test mass m in this phase space starting in one of the invariant manifolds will continue in it [14].

In the following sections some of the different types of invariant manifolds are going to be studied. There are center manifolds, which represent the phase space of periodic and quasi-periodic orbits, and hyperbolic manifolds or saddle manifolds, which can be stable or unstable and represent the phase space of orbits that wind on or off the periodic and quasi-periodic orbits, respectively [14].

The motion of all of them is restricted by the Jacobi constant C. Not all space is accessible to them. In fact, where the velocity is zero, a boundary is found between allowed and forbidden regions. A satellite can reach this boundary if it only touches it with zero velocity, but it can never cross it and reach the forbidden region of motion. Imposing $v = 0$ in Equation (2.28), this boundary's curve is obtained, which satisfies $-U = C$. Then, it can be seen that this curve seem to be the contour of the effective potential pictured in Figure 2.3. This curve is also called the **zero-velocity curve**, or the **Hill curve** after astronomer Hill, who studied this issue in detail in the 19th century [14] [22].

Then, for a given Jacobi constant C the boundary curves can be obtained, which separate the allowed region, where $-U \leq C$, from the forbidden region, where $-U > C$. According to Equation (2.29), the allowed region is found where r_1 and r_2 are small, i.e. the spacecraft is located near either of the two primaries, or also where $\frac{1}{2}(x^2 + y^2)$ is big, i.e. being far away from the primaries, where the centrifugal forces are higher [14].

Finally, regarding the locations of the five libration points, five different cases of the Hill's region (the allowed region of motion) can be observed. Denoting by E_i the energy of the test mass m at rest at the Lagrange point L_i, where $i = 1, ..., 5$ [23]:

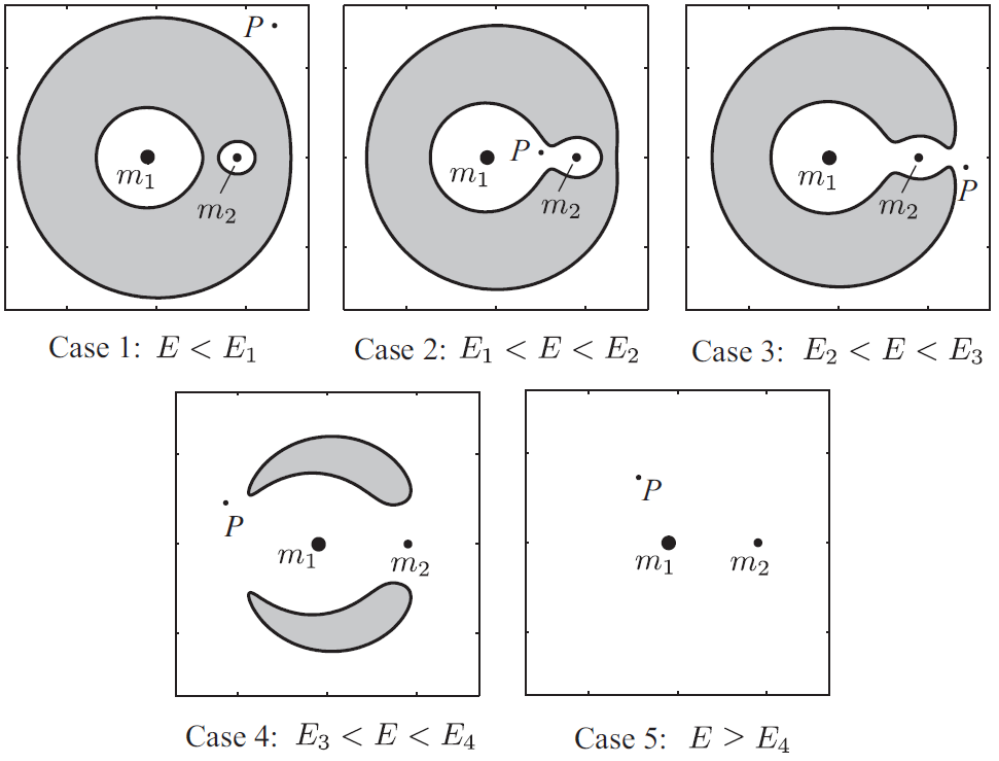

Figure 2.5: The five cases of the Hill's region. The zero-velocity curves are plotted in the x-y plane separating the Hill's region (in white) from the forbidden region of motion (shaded) for the particle P. Credit: Koon, W. et al. [23]

- **Case 1:** L1 is the Lagrange point with the lowest energy. Then, if the energy of the test mass (or particle P) E is below E_1, the particle can move around the vicinity of any of the primaries or in the realm far away from them which extends to infinity, but never between realms.
- **Case 2:** When the energy E is higher than E_1 but lower than E_2, a corridor opens through L1 so that the particle can move between the realms of m_1 and m_2. However, these two realms are still isolated from the exterior realm.
- **Case 3:** When E is higher than E_2, the same occurs as in the previous case, but now the corridor opens through L2, allowing the particle P to move between all the three realms through this point.
- **Case 4:** A new corridor between the realm around m_1 and the exterior realm is opened through L3, as E is higher than E_3.

- **Case 5:** Finally, if the energy of the particle is higher than the energy at L4 and L5, $E > E_4 = E_5$, it can reach both L4 and L5. These are the two points of highest energy, and therefore the forbidden region disappears, allowing the spacecraft to move without restrictions through all the x-y plane.

Of course, these energies represent the restrictions imposed by the Jacobi constant C.

2.7 Types of trajectories

2.7.1 Chaotic trajectories

It has been seen that the conservation of the Jacobi constant is the only restriction imposed to the motion of a test mass. Then, any trajectory of a body has no limits except the zero-velocity curves. As no further information can be obtained regarding the kind of motion of the body, the only way to determine a trajectory consists of solving, numerically, the equations of motion of the CR3BP for a specific set of initial conditions, or a specific initial state vector. However, when changing just slightly the initial conditions, it is found that the deviations from the original trajectory increase, ending up in a totally different path. This is called **deterministic chaos**, the behaviour of being very sensitive to the variations of the initial conditions, which is deterministic in the short run, but not in the long run, converting the trajectories into chaotic ones [14].

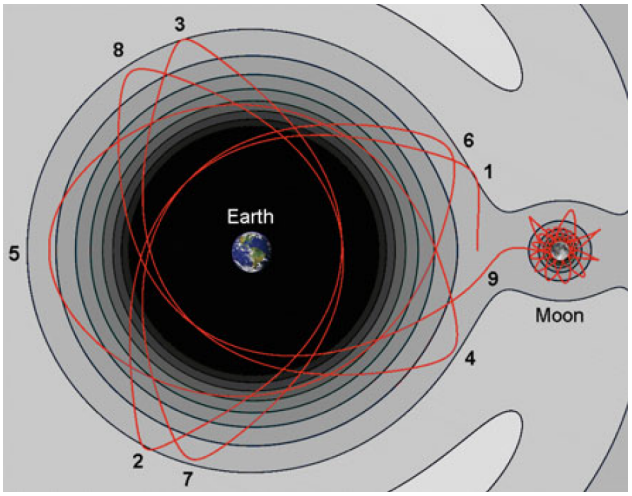

Figure 2.6: Example of a chaotic trajectory in the Earth-Moon system with a final Moon capture. Credit: Walter, U. [14]

2.7.2 Trajectories around the collinear libration points

After obtaining the equations of motion of a test mass m moving in the vicinity of the Lagrange point L1, L2 or L3 and relative to one of them in the synodic reference frame, from the equations of motion of the CR3BP (2.20), (2.21) and (2.22), the types of solutions and their behaviours can be studied from their linear part

[14]:

$$\ddot{x} - 2\dot{y} - (1 + 2c_2)x = 0 \tag{2.44}$$

$$\ddot{y} + 2\dot{x} - (1 - c_2)y = 0 \tag{2.45}$$

$$\ddot{z} + c_2 z = 0 \tag{2.46}$$

These are the linearized equations of motion around a collinear equilibrium point, where c_2 is a coefficient that depends on the Lagrange point that is being orbited. For further information consult Ulrich Walter's book [14].

Before solving them, it is seen that the equation of motion in the z-axis decouples from the other two displaying the motion of a harmonic oscillator with a certain frequency $\omega_z = \sqrt{c_2}$. And after solving the equations of motion in the x- and y-axis, the solutions are mainly driven by some coefficients A_1, A_2, A_{xy}, A_z, ω_{xy} and ω_z, as the solutions can be written as follows [14]:

$$x = A_1 e^{s\tau} + A_2 e^{-s\tau} + A_{xy} \cos(\omega_{xy}\tau + \phi) \tag{2.47}$$

$$y = a(A_1 e^{s\tau} - A_2 e^{-s\tau}) + bA_{xy} \sin(\omega_{xy}\tau + \phi) \tag{2.48}$$

$$z = A_z \cos(\omega_z \tau + \psi) \tag{2.49}$$

Then, when $A_1, A_2 = 0$ stable periodic solutions are found (these are the center manifolds), but when $A_1, A_2 \neq 0$ unbounded solutions are found (these are the hyperbolic or saddle manifolds) [14].

Center Manifold Orbits

Regarding the center manifolds (when $A_1, A_2 = 0$), two types of **periodic** orbits are found [14]:

- **Vertical Lyapunov orbits:** Found when $A_{xy} = 0$ but $A_z \neq 0$. They are vertical periodic motions along the z-axis oscillating with a frequency ω_z.
- **Horizontal Lyapunov orbits:** Found when $A_{xy} \neq 0$ but $A_z = 0$. They are near-elliptic orbits in the x-y plane oscillating with a frequency ω_{xy}. The semi-major axis extends along the y-axis, and it is approximately 3.2 times the semi-minor axis, which extends along the x-axis.

However, when both amplitudes $A_{xy}, A_z \neq 0$, quasi-periodic 2D tori orbits named as **Lissajous orbits** are found. They revolve either vertical or horizontal Lyapunov orbits, and, in general, they do not close. Usually, $\omega_{xy} > \omega_z$, but more energetic Lissajous orbits (for increasing both amplitudes and frequencies) can have cases where ω_{xy}/ω_z becomes a rational value, meaning that the Lissajous orbits close and become periodic orbits [14].

Finally, there is a special case when $\omega_{xy} = \omega_z$, i.e. the test mass oscillates with the same frequencies both in the x-y plane and in the z-axis. One new type of periodic orbit appears then, the **halo orbits**, which bifurcate from the horizontal Lyapunov orbits. When, however, $\omega_{xy} \approx \omega_z$, quasi-periodic orbits around the

halo orbits are found, which are therefore called **quasi-halo orbits**. Between these and the Lissajous orbits, chaotic trajectories are found [14].

A summary of all the center manifolds around a collinear libration point is given in Figure 2.7, which is a **Poincaré map** provided in Ulrich Walter's book [14]. A Poincaré map of an orbit is the set of its points that intersect a specific plane, which in Figure 2.7 is the x-y plane. This allows picturing a 3D orbit only in 2D [14].

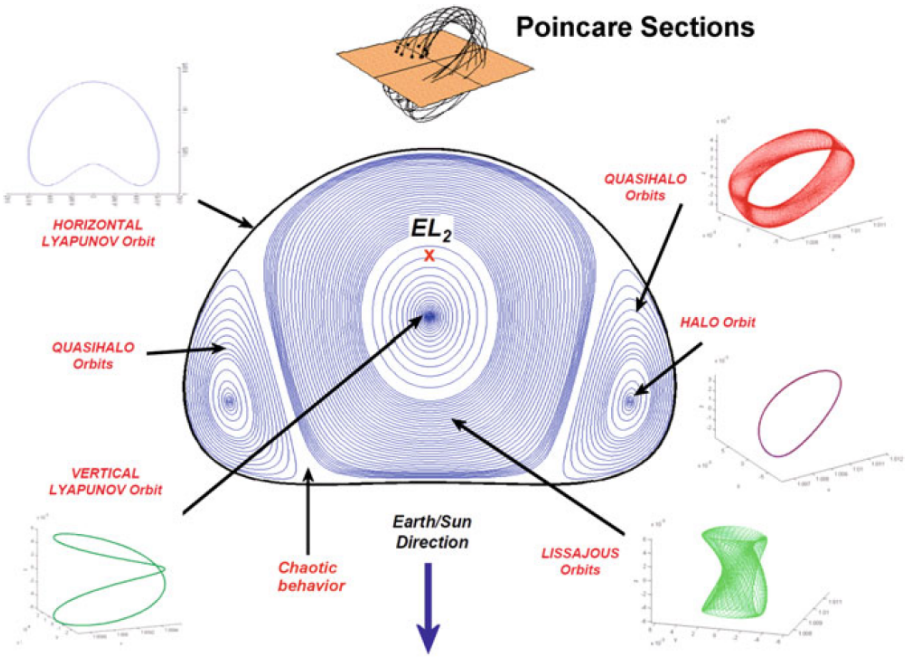

Figure 2.7: Poincaré maps of center manifold orbits around the collinear libration point L2. Credit: Walter, U. [14]

It is important to remember that all these orbits appear from the linearized equations of motion. In fact, when the non-linear factors are also considered, all the coefficients that describe these trajectories change, varying the frequencies and increasing the amplitudes of the orbits [14].

As in the present thesis the planar CR3BP is used, only planar orbits whose motions happen in the x-y plane can be considered. These are the **horizontal Lyapunov orbits**, and they will be used as the departing orbits to reach L4 and L5. However, as already explained, it can be seen that the rest of orbits could be considered when taking into account the oscillating motion in the z-axis with a frequency ω_z (in the case of the horizontal Lyapunov orbits, $\omega_z = 0$).

Hyperbolic Manifolds

All the previous periodic and quasi-periodic orbits have instabilities, as they are located around the unstable collinear points, and when $A_{xy} \neq 0$, hyperbolic or saddle manifolds appear [14]:

- **Stable manifolds:** If $A_1 = 0$ but $A_2 \neq 0$, there appear trajectories that wind onto periodic center manifolds (such as Lyapunov or halo orbits), asymptotically (not in finite time).

- **Unstable manifolds:** If $A_1 \neq 0$ but $A_2 = 0$, there appear trajectories that wind off center manifolds, also asymptotically.

Their motions can happen in the x-y plane if $A_z = 0$, but if $A_z \neq 0$ only an oscillation with ω_z would appear in the z-axis [14].

In the present thesis, unstable manifolds will be used in order to take advantage of the instabilities of the problem to get to L4 and L5 from L1 and L2. Furthermore, both all possible stable and unstable manifolds form tubes that separate the manifolds according to their energy, which can be seen in the following Figure 2.8:

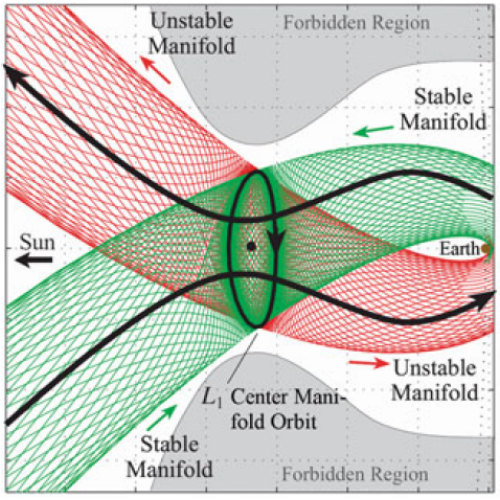

Figure 2.8: Stable manifolds (green) and unstable manifolds (red), coming up to or from a center manifold orbit around, in this case, L1 of the Earth-Sun system. Credit: Walter, U. [14]

2.7.3 Trajectories around the equilateral libration points

Finally, in the Lagrange points L4 and L5 similar features are found when trying to solve the equations of motion in the vicinity of these libration points and relative to them. Again, the vertical motion is decoupled and it also describes a harmonic oscillation, but this time with a frequency ω_z equal to the angular velocity of the synodic reference frame, defined in Equation (2.1) [14]. The linearized equations of motion are the following according to Ulrich Walter's book [14] (the upper minus sign is associated to L4, and the lower plus sign to L5):

$$\ddot{x} - 2\dot{y} - \frac{3}{4}x \mp \frac{3\sqrt{3}}{4}(1-2\mu)y = 0 \tag{2.50}$$

$$\ddot{y} + 2\dot{x} - \frac{9}{4}y \mp \frac{3\sqrt{3}}{4}(1-2\mu)y = 0 \tag{2.51}$$

$$\ddot{z} + z = 0 \tag{2.52}$$

Then, when solving the linearized equations for the motion in the x-y plane, two modes associated to two periodic motions about L4 or L5 are found when their two frequencies ω_1 and ω_2 are real, and not imaginary, which happens when the fraction between the primary masses is of $m_1/m_2 = 24.96$ or higher (or $\mu \leq 0.03852$),

the condition of stability regarding these equilateral libration points. In fact, this is related to a minimum curvature of the effective potential U at both L4 and L5 for which enough acceleration and velocity are caused so that the resulting Coriolis force can curve the test mass trajectory and insert it onto a bounded periodic orbit [6] [14].

Regarding the two modes of periodic motion, they are a short-term mode with a similar period to that of the system and a long-term mode with a smaller frequency. Both of them combine and the resulting trajectory can be considered as a short-term elliptic epicycle moving on a long-term ellipse around L4 or L5 [14].

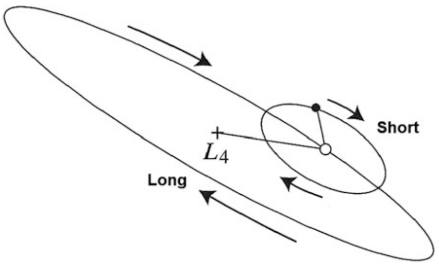

Figure 2.9: Combination of the short and long periodic motions around L4. Credit: Walter, U. [14]

However, when the motion deviates too far from the equilateral points, the resulting orbits differ from these combinations of short and long term modes, which now can only be obtained from the numerical resolution of the non-linear equations of motion. Then, for lower energy orbits and with higher initial tangential velocities the orbits become more elongated and depart further from L4 or L5. Although the short-term mode remains, the ellipse of the long-term mode converts its semi-major axis onto a circular arc along the path of the orbit of m_2 around m_1. These are called **tadpole orbits**. And for even lower Jacobi constants and higher initial tangential velocities, these tadpole orbits around L4 and L5 elongate and arc more until finally meeting at L3 and merging, which are then called **horseshoe orbits** [14].

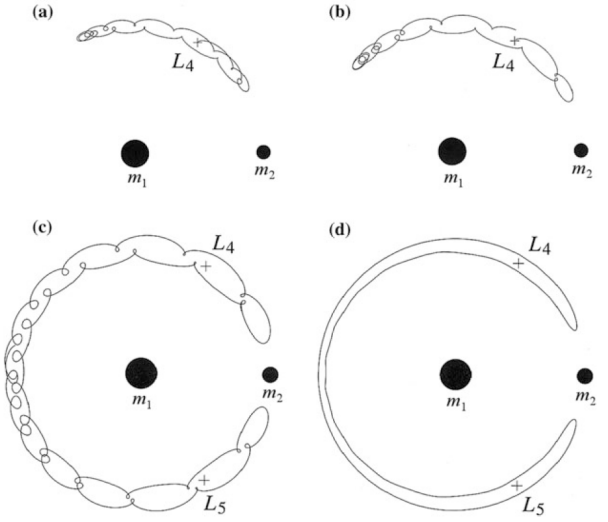

Figure 2.10: Resulting types of orbits around the equilateral libration points: **(a)**, **(b)**. Tadpole orbits. **(c)**, **(d)**. Horseshoe orbits. Credit: Walter, U. [14]

In the present thesis, the objective is to get to the RPS around L4 and L5. They are defined as the regions from where a test mass m starting with zero synodic velocity does not leave the vicinity of these equilateral libration points for 1000 years or more [2] [8]. The resulting trajectories, however, will be seen to match the behaviour stated in these previous types of orbits, which will be obtained directly from solving numerically the non-linear equations of motion of the planar CR3BP, which are Equations (2.20) and (2.21). However, when defining the PSD only the orbits that remain in the vicinity of L4 or in that of L5 will be taken, so no merging, horseshoe orbits will be considered, only tadpole orbits.

All these types of orbits can touch the zero-velocity curves at some points with zero velocity, although it does not have to happen, but never can cross them [14]. Then, for higher Jacobi constants, i.e. higher energy, the forbidden regions are smaller, and, therefore, these orbits get closer to L4 or L5 [14], something that will be confirmed later in the study.

Finally, it is important to note that a vertical oscillation can be added to these orbits with a frequency ω_z if the initial condition has a component of the velocity in the z-axis [14].

For further information about the obtaining and resolution of the linearized equations of motion, consult Ulrich Walter's *Astronautics: The Physics of Space Flight* book [14].

2.8 Invariant manifolds computation

It is important to know how to get and compute the stable and unstable manifolds of a periodic orbit in order to insert the spacecraft in one of them to take advantage of the natural dynamics of the CR3BP. In the present thesis, the idea is to depart from horizontal Lyapunov orbits around L1 and L2 in order to get to the vicinities of L4 and L5 by means of the unstable manifolds of these Lyapunov orbits. In fact, all the motion through the region where the periodic orbit resides has to occur through the previously mentioned manifold tubes. If a particle's initial conditions that belong to an unstable or stable manifold are propagated forward or backward, respectively, in time, it will be found that the particle will move from one realm to the other through these manifold tubes [23].

Following Koon et al. book's [23] nomenclature, where the CR3BP trajectory with $x(t_0) = x_0$ is denoted by $\Phi(t; x_0)$ (it represents the trajectory of a particle from its initial location x_0 at time t_0 to its final location at time t), it can be seen that it satisfies the equations of motion (which can be defined as $\dot{x} = f(x)$):

$$\frac{d\Phi(t; x_0)}{dt} = f(\Phi(t; x_0)) \qquad \text{with } \Phi(t_0; x_0) = x_0 \tag{2.53}$$

Then, the deviation of a trajectory that starts from the perturbed initial condition $\bar{x}_0 + \delta\bar{x}_0$ at time t_0 with respect to the reference trajectory $\bar{x}(t)$ can be computed over time as follows [23]:

$$\delta\bar{x}(t) = \Phi(t; \bar{x}_0 + \delta\bar{x}_0) - \Phi(t; \bar{x}_0) \tag{2.54}$$

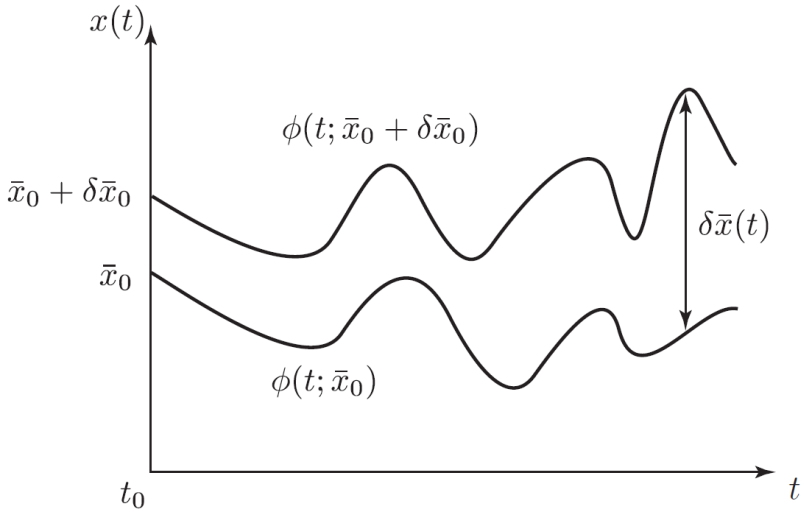

Figure 2.11: Deviation between the initially perturbed trajectory $\Phi(t;\bar{x}_0+\delta\bar{x}_0)$ and the reference trajectory $\Phi(t;\bar{x}_0)$. Credit: Koon, W. et al. [23]

Which at time t_1 will be the following:

$$\delta\bar{x}(t_1) = \Phi(t_1;\bar{x}_0+\delta\bar{x}_0) - \Phi(t_1;\bar{x}_0) \tag{2.55}$$

This can be expanded in Taylor series:

$$\delta\bar{x}(t_1) = \frac{\partial\Phi(t_1;\bar{x}_0)}{\partial x_0}\delta\bar{x}_0 + \textit{higher order terms} \tag{2.56}$$

From here, an interesting term is obtained: the **State Transition Matrix (STM)**, which is the matrix $\frac{\partial\Phi(t_1;\bar{x}_0)}{\partial x_0}$. It is an interesting matrix because it gives the linear relationship between the slight initial variations of the initial location $\bar{x}_0$ and the final variations with respect to the reference trajectory's final location $\bar{x}_1$. Abbreviating the STM as $\Phi(t_1,t_0)$, this can be seen in the following expression:

$$\delta\bar{x}(t_1) = \Phi(t_1,t_0)\delta\bar{x}(t_0) \tag{2.57}$$

It is important to note that Equation (2.57) is also the solution to the **variational equations** of the equations of motion of the CR3BP [23]. Therefore:

$$\delta\dot{\bar{x}}(t) = Df(\bar{x}(t))\delta\bar{x} \tag{2.58}$$

These are the linearized equations for the evolution of the variations $\delta\bar{x}$, where $Df(\bar{x}(t))$ is the Jacobian matrix of the flow field f of the equations of motion evaluated along the reference trajectory $\bar{x}(t)$ [23].

In order to compute the STM along a desired reference trajectory $\bar{x}(t)$, Equation (2.53) (which states that

the trajectory satisfies the equations of motion) can be differentiated with respect to x_0:

$$\frac{d}{dt}\frac{\partial\Phi(t;\bar{x}_0)}{\partial x_0} = Df(\Phi)\frac{\partial\Phi(t;\bar{x}_0)}{\partial x_0} \tag{2.59}$$

And the initial condition yields $\frac{\partial\Phi(t_0;x_0)}{\partial x_0} = I_n$, where I_n is the $n \times n$ identity matrix. For the CR3BP this is a 6×6 matrix, and for the planar CR3BP, as in the case of the present thesis, this is a 4×4 matrix. Then, the STM is the solution for the following initial value problem [23]:

$$\dot{\Phi}(t,t_0) = Df(\bar{x}(t))\Phi(t,t_0) \qquad \text{with } \Phi(t_0,t_0) = I_n \tag{2.60}$$

However, as the Jacobian matrix $Df(\bar{x}(t))$ is time dependent, this problem can not be solved analytically, as the CR3BP does not offer analytical solutions for reference trajectories $\bar{x}(t)$. Therefore, the equations of this problem have to be solved numerically together with the first order equations of motion $\dot{x} = f(x)$, so that the STM can be finally computed [23]. The first-order equations of motion of the planar CR3BP can be obtained from Equations (2.20) and (2.21), and are the following:

$$\dot{x} = v_x \tag{2.61}$$

$$\dot{y} = v_y \tag{2.62}$$

$$\dot{v_x} = 2v_y + x - \frac{1-\mu}{r_1^3}(x+\mu) - \frac{\mu}{r_2^3}(x+\mu-1) \tag{2.63}$$

$$\dot{v_y} = -2v_x + y - \frac{1-\mu}{r_1^3}y - \frac{\mu}{r_2^3}y \tag{2.64}$$

If the effective potential U from Equation (2.29) is considered, the first-order equations of motion can also be written as [23]:

$$\dot{x} = v_x \tag{2.65}$$

$$\dot{y} = v_y \tag{2.66}$$

$$\dot{v_x} = 2v_y + \frac{\partial U}{\partial x} \tag{2.67}$$

$$\dot{v_y} = -2v_x + \frac{\partial U}{\partial y} \tag{2.68}$$

Then, the Jacobian matrix of the flow field f of the first-order equations of motion of the planar CR3BP,

$Df(\bar{x}(t))$, is the following (evaluated along a reference trajectory $\bar{x}(t)$) [23]:

$$Df(\bar{x}(t)) = \begin{pmatrix} 0 & 0 & 1 & 0 \\ 0 & 0 & 0 & 1 \\ \frac{\partial^2 U}{\partial x^2} & \frac{\partial^2 U}{\partial x \partial y} & 0 & 2 \\ \frac{\partial^2 U}{\partial y \partial x} & \frac{\partial^2 U}{\partial y^2} & -2 & 0 \end{pmatrix}_{\bar{x}(t)} \tag{2.69}$$

With all that, the initial value problem of Equation (2.60) can be solved numerically, integrating both the variational equations with the identity 4×4 matrix as the initial condition as well as the 4 first-order equations of motion of the planar CR3BP, with initial conditions the initial state vector in the orbit.

However, in order to perform a stability analysis of a periodic orbit and to obtain its stable and unstable manifolds, the **Monodromy matrix** of that orbit whose period is T is needed. The Monodromy matrix is the STM after one orbital period T, which therefore determines if the initial perturbations in the periodic orbit decay or grow after one period [23].

Once the Monodromy matrix of a periodic orbit is obtained (solving the previous initial value problem between times 0 and T), its invariant manifolds can be computed. In order to do that, first of all the eigenvalues and eigenvectors of the Monodromy matrix have to be computed numerically. For horizontal Lyapunov orbits in the planar CR3BP, one real pair and one pair equal to unity of eigenvalues are obtained [23]:

$$\lambda_1 > 1 \qquad \lambda_2 = \frac{1}{\lambda_1} \qquad \lambda_3 = \lambda_4 = 1$$

According to Koon et al. book [23], the eigenvector of the Monodromy matrix associated to λ_1 is in the direction of the unstable manifold, while the eigenvector associated to λ_2 is in the direction of the stable manifold. From further analysis of the Monodromy matrix, it is found that a periodic orbit in the CR3BP must have at least two eigenvalues equal to one, which are λ_3 and λ_4 [23].

With both normalized stable and unstable eigenvectors, $Y^s(X_0)$ and $Y^u(X_0)$ respectively, a first local approximation for both manifolds of the Lyapunov orbit can be found:

$$X^s(X_0) = X_0 + \epsilon Y^s(X_0) \tag{2.70}$$

$$X^u(X_0) = X_0 + \epsilon Y^u(X_0) \tag{2.71}$$

X_0 is the initial state vector in the Lyapunov orbit, and $X^s(X_0)$ and $X^u(X_0)$ are, respectively, the first local approximations of the state vector at X_0 for the stable and unstable manifolds. The ϵ parameter is a small displacement from the initial state vector in the periodic orbit X_0, which should be small enough to validate the linear estimate of the local approximations for the manifolds, but at the same time big enough so that the time of flight it takes to drift away from the orbit does not become excessively large. In order to satisfy both

restrictions, ϵ should be a positive value around 10^{-6} [23], although in the present thesis it will be considered to reach values up to 10^{-5}. It has to be noted that there are two possible directions for both the unstable and stable manifolds, which can be locally approximated by using ϵ or $-\epsilon$ [23].

Finally, once the initial state vectors for both the stable and unstable manifolds are known ($X^s(X_0)$ and $X^u(X_0)$, respectively), they can be propagated in time with the equations of motion to compute both manifolds: forward for the unstable manifold, but backward for the stable one [23].

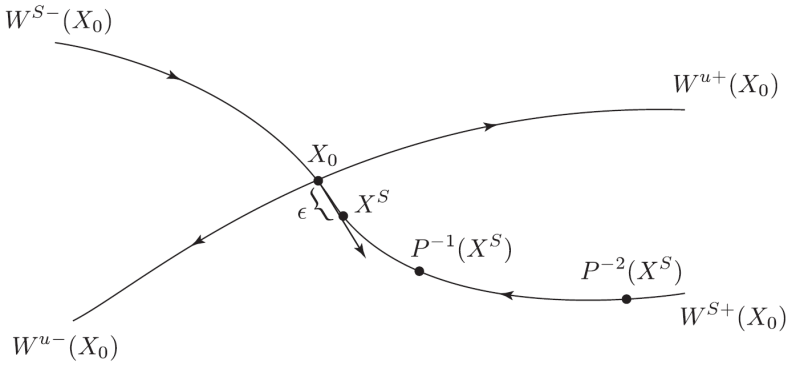

Figure 2.12: Linear local approximation of the stable (W^s) and unstable (W^u) manifolds at X_0 of a periodic orbit. Credit: Koon, W. et al. [23].

With this procedure, the manifolds that wind off or onto a periodic orbit can be computed for the state vector X_0 in it. However, it has been mentioned that all the trajectories of a manifold form a tube. In order to find not just one, but many trajectories of the tube, two different computations can be carried out:

- Compute the initial state vectors for the manifolds for an interval of different values of ϵ, for example, 100 values between 10^{-5} and 10^{-6}. Without violating the linear approximation, different values of ϵ suppose starting points in different locations of the manifold tubes.
- Compute the initial state vectors for the manifolds always with the same ϵ, but at different initial state vectors in the Lyapunov orbit. The STM can be used to transport the eigenvectors from X_0 to a new initial state vector $X(t)$ as shown next [23]:

$$Y^s(X(t)) = \Phi(t,0)Y^s(X_0) \tag{2.72}$$

$$Y^u(X(t)) = \Phi(t,0)Y^u(X_0) \tag{2.73}$$

  The new eigenvectors have to be normalized again due to the fact that the STM does not maintain its norm [23].

With that, this theory chapter can be considered to cover all the necessary concepts to start finding for the most optimal trajectories up to L4 and L5.

Chapter 3

Methodology

In this section, all the necessary procedures carried out in order to define the RPS around L4 and L5, to describe the types of trajectories in these regions and to study the most optimal transfers to L4 and L5 are going to be explained. Some initial and preliminary results are also going to be discussed.

Find attached in the *Report Attachments* document all the MATLAB codes used in this chapter.

3.1 Practical Stability Domains

As already mentioned, L4 and L5 are stable points. Therefore, a spacecraft can orbit them with no station keeping required. However, it is difficult to reach these equilibrium points, so a very little amount of missions have taken advantage of these stable locations [8].

To try to improve this and make it easier and more affordable to get to these Lagrange points L4 and L5, the stability regions or RPS around these points are going to be considered. These are defined as the regions around L4 and L5 where the trajectory of a spacecraft starting from these regions with 0 synodic velocity (i.e. 0 velocity with respect to the synodic reference frame) does not leave the vicinity of L4 or L5 for more than 1000 years [2] [8]. Then, these RPS are defined as the sets of initial conditions (with 0 synodic velocity) from where a spacecraft starts its trajectory and, after propagating over time (more than 1000 years) these initial conditions, the spacecraft's trajectory is still inside the vicinity of L4 or L5 [8]. These stability regions are called the Practical Stability Domains.

First of all, in order to find these regions, a set of initial conditions K has to be defined in the vicinity of L4 and L5. Then, all these initial conditions have to be propagated in time up to T years. During the propagation, if the trajectory of the spacecraft leaves a larger set $K' \supset K$ that limits the vicinity of L4 and L5, the propagation is stopped and this initial condition is discarded for the RPS. Leaving this set K' defines the escaping criterion to stop the propagation of those initial conditions from the set K and to discard them for the RPS. As mentioned earlier, all these initial conditions consider 0 synodic velocity. Therefore, the Practical Stability Domains are 3D sets. However, as in the present thesis only the planar case of the CR3BP

is being used, the resulting RPS will be a slice of them in the plane of the ecliptic ($z = 0$) [2] [8].

It has been decided that the RPS to study contains all the initial conditions that do not leave the vicinity of L4 and L5 for a minimum of $T = 1000$ years. Then, in order to establish the set K of initial conditions, this is going to consider only the Lagrange point L4. The RPS around L5 will be obtained from that around L4 due to the symmetry of the problem [8] [27].

Regarding the set K of initial conditions, it is convenient to change to polar coordinates centered at the Sun, but translating the origin of this system of coordinates to L4, for both radial and angular dimensions, so that $(r, \theta) \in (-1, \infty) \times [-0.5, 0.5)$, with r and θ being the Sun radial distance to L4 (measured in AU) and the angle with respect to the L4-Sun line (measured positive counterclockwise and in $rad/(2\pi)$), respectively [2] [8]. These polar coordinates can be transformed back to Cartesian coordinates in the synodic reference frame using the following equations:

$$x = -\mu + (r + r_4)\cos(2\pi\theta + \theta_4) \tag{3.1}$$

$$y = (r + r_4)\sin(2\pi\theta + \theta_4) \tag{3.2}$$

Where r_4 and θ_4 are the polar coordinates of L4:

$$r_4 = \sqrt{(x_4 + \mu)^2 + y_4^2} \tag{3.3}$$

$$\theta_4 = \arctan\left(\frac{y_4}{x_4 + \mu}\right) \tag{3.4}$$

Now, the algorithm to find the region of stability around L4 can be started [2] [8] [27]:

- **Step 1: First approximation.**

  The set of initial conditions K can be proposed. After many tests and in order to reduce computation times and data size, a suitable set is defined as follows:

  $$K = [\theta_0, \theta_1]\, rad/(2\pi) \times [r_0, r_1]\, AU = \left[-0.15, \frac{1}{3}\right] rad/(2\pi) \times [-0.002, 0.002]\, AU$$

  This set of initial conditions is covering an area around L4 with angles, with respect to the Sun-L4 line, from -54º (near Earth's vicinity) up to 120º (Earth-Sun-L3 line), and with Sun radial distances relative to L4 from -0.002 AU to 0.002 AU, as can be seen in Figures 3.1 and 3.2.

  In order to propagate these initial conditions over $T = 1000$ years, this set K is discretized into a $N_\theta \times N_r$ grid, with $N_\theta = N_r = 100$, so that 10000 initial conditions are going to be analyzed according to the following:

  $$\theta_i = \theta_0 + i\frac{\theta_1 - \theta_0}{N_\theta - 1} \qquad \text{for } i = 0, ..., N_\theta - 1$$

  $$r_j = r_0 + j\frac{r_1 - r_0}{N_r - 1} \qquad \text{for } j = 0, ..., N_r - 1$$

Then, these initial conditions are transformed into Cartesian coordinates x and y using Equations (3.1) and (3.2), and added to their respective initial velocity conditions of zero synodic velocity: $\dot{x} = \dot{y} = 0$.

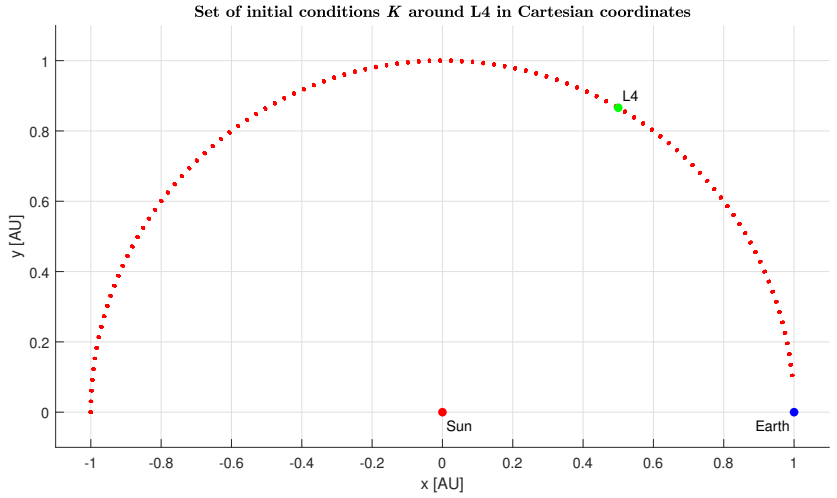

Figure 3.1: Set of initial conditions K to start the 1st approximation of the PSD (Cartesian coordinates).

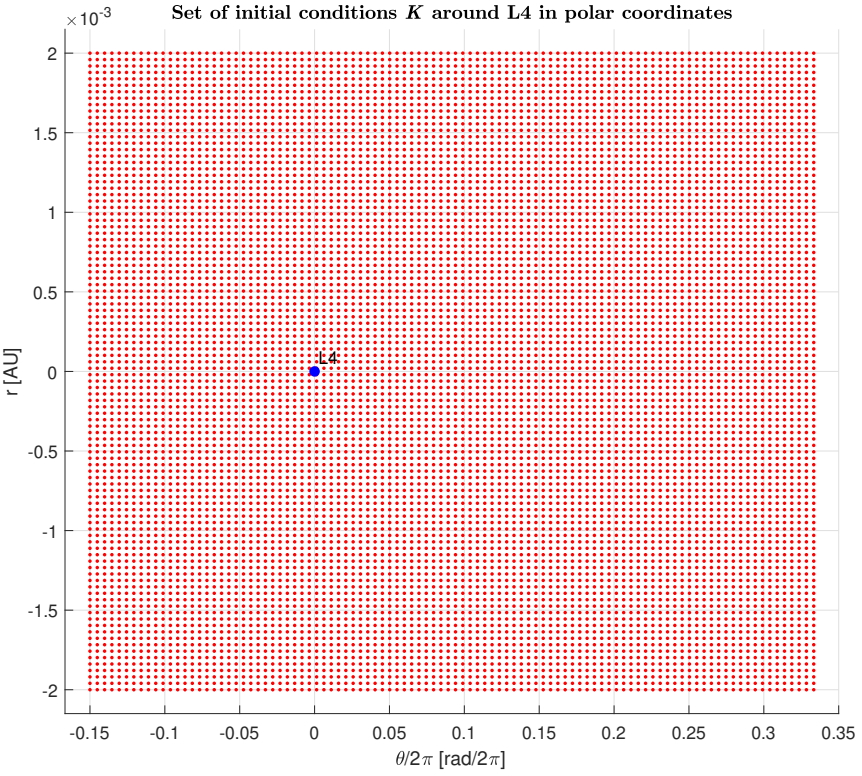

Figure 3.2: Set of initial conditions K to start the 1st approximation of the PSD (polar coordinates).

The next step consists on propagating over time up to $t = 2\pi T_0$, with $T_0 = 1000$ years, all these initial conditions. This is done by integrating the equations of motion (2.20) and (2.21) during this time span, for what the normalized mass of the Earth μ is needed. In order to use tabulated values, the one from NASA's JPL [26] is used: $\mu = 3.05420 \times 10^{-6}$ (see Section 2.3.3).

Then, if during the propagation ($t < 2\pi T_0$) the test mass meets the escaping criterion, the solving of the CR3BP is stopped and this initial condition is discarded for the PSD (it is marked with a -1). If not, the propagation continues until reaching the end of the time span ($t = 2\pi T_0$) and this initial condition is taken as part of the PSD (it is marked with a $+1$) [27].

Regarding the escaping criterion itself, it is defined as a set of conditions that describes the boundaries of the vicinity of L4 and L5 K'. Focusing only on the region around L4, the escaping criterion is met when the spacecraft leaves its vicinity. The following regions are excluded from this vicinity of L4 [27]:

- Points located far away from the system: $r_S > 1.5$ AU.
- The neighbourhood of the Sun: $r_S < 0.5$ AU.
- The neighbourhood of the Earth: $r_E < 2 \cdot R_{Earth}$ and $-D_{Angle} \leq \theta \leq D_{Angle}$.
- Points close to the domain of L5: $y < -0.585$ and $252^{\text{o}} \leq \theta \leq 324^{\text{o}}$.

Where r_S is the distance from the Sun to the spacecraft, r_E from the Earth to the spacecraft, R_{Earth} is the Earth radius, θ is the angle that the spacecraft forms with the Sun and D_{Angle} is an exclusion angle (measured from the Sun) defined with two times Earth's radius:

$$r_S = \sqrt{(x+\mu)^2 + y^2}$$
$$r_E = \sqrt{(x-(1-\mu))^2 + y^2}$$
$$\theta = \arctan\left(\frac{y}{x+\mu}\right)$$
$$D_{Angle} = \arctan\left(\frac{2 \cdot R_{Earth}}{1}\right)$$

Finally, as the CR3BP is being solved in dimensionless variables, the R_{Earth} to be used has to be defined also in dimensionless units. In the CR3BP, distances are dimensionless with respect to the mutual distance between the primaries r_{12}, which in the case of the Earth-Sun system it is $r_{12} = 149.597871 \times 10^9$ m [26]. Then, knowing that Earth's radius is of 6.378×10^6 m [26]:

$$R_{Earth} = \frac{6.378 \times 10^6}{149.597871 \times 10^9}$$

Now that the escaping criterion is defined, the first approximation of the PSD can be started to be computed and saved.

- **Step 2: Refinement.**

  From the points that are part of the PSD (marked with a $+1$), those in the region's boundary shall be

reiterated within a larger time span to make sure whether they are escaping the stability region. In order to do this, the boundary of depth d has to be defined. This is the set of initial condition points (r_j, θ_i) that are part of the PSD (labeled with a +1) but that have, at least, one point (r_{j+m}, θ_{i+n}) which is outside the region (labeled with a -1), where $n, m = -d, -d+1, ..., d-1, d$. Then, all the points of the boundary of depth are propagated, again, but this time for $T_1 > T_0$ years (until $t = 2\pi T_1$). Also, the escaping criterion is checked for every point during the propagation, and all of them are finally labeled as non-escaping points (+2) or escaping points (-2). With that, the boundary of the first approximation of the PSD will have changed [8] [27].

This refinement step can be repeated as many times as desired, but with the purpose to make sure that none of the points of the boundary escape before T_1 years [8]. However, 10000 initial conditions is a relatively small grid of points, and as the most interesting points are those that remain closer to L4 (PSD points nearer to L4, thus further to PSD's boundary), only one refinement is carried out.

The number of years to propagate this boundary of depth has been set to $T_1 = 10000$ years, while the boundary of depth to $d = 2$. According to [8], $d = 2$ is a good approach for Hamiltonian cases, regarding the rate of escape of orbits. Hamiltonian cases are those which possess at least one constant first integral, which in the case of the CR3BP is the conservation of the Jacobi constant [8]. In fact, with only one refinement and with this boundary of depth, it has been found that none of the points of the boundary actually escapes the vicinity of L4. Then, the resulting PSD can be assumed to be correct and precise enough for the next operations.

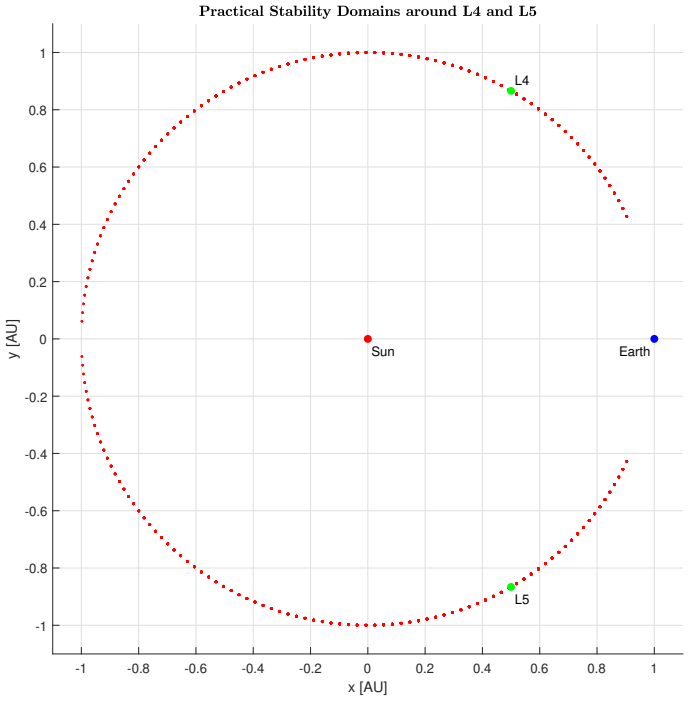

Figure 3.3: Practical Stability Domains around L4 and L5 in the Earth-Sun system (in Cartesian coordinates).

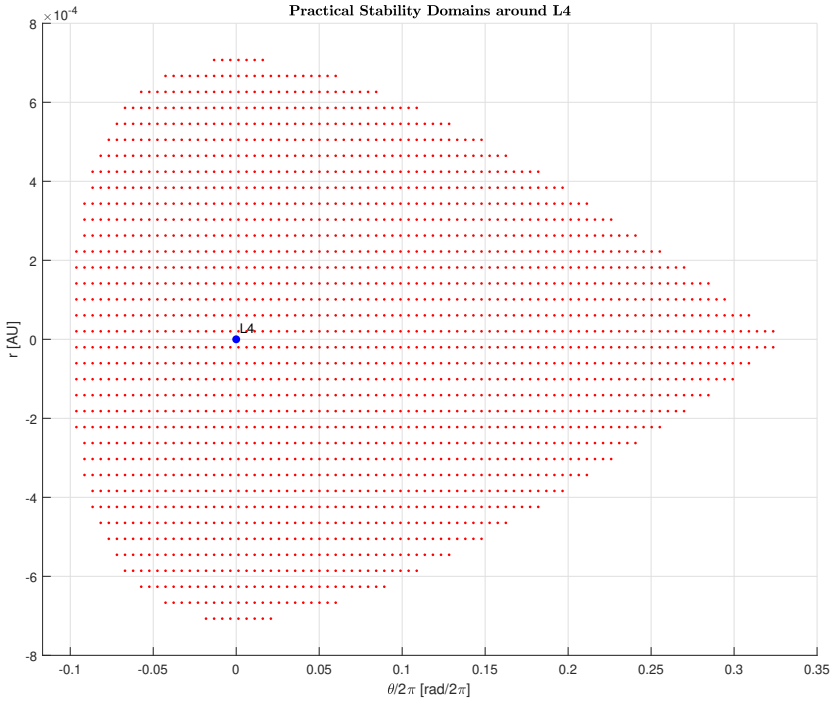

Figure 3.4: Practical Stability Domains around L4 in the Earth-Sun system (in polar coordinates).

After finding the first approximation of the PSD and refining it, the resulting one can be seen in Figures 3.3 and 3.4. From the 10000 initial conditions considered in the initial set K, only 2062 form the PSD around L4 (other 2062 for the PSD around L5). The rest of initial conditions are those that escape the vicinity of L4 or L5 before 1000 years, either drifting away from the system or colliding with one of the two primaries (Sun or Earth).

Once the PSD have been found, the next objective consists of understanding the types of trajectories in these regions around L4 or L5.

The codes used in this and the following section are the ones in Sections A.2 and A.3 in the *Report Attachments* document.

3.2 Types of trajectories in the PSD

Now that the PSD are known, the initial conditions for those trajectories that do not escape L4 or L5's vicinity are also known (it is important to remember that these initial conditions also consider 0 initial synodic velocity). Then, in order to calculate and save the trajectories, these initial conditions shall be propagated over time until a final instant $t = 2\pi T$.

In order to monitor and understand the motion of these orbits, the coordinates (r, θ) are going to be measured for all the propagation time span. Then, due to the shape of the trajectories, it is interesting to calculate

how much both polar coordinates vary during one trajectory revolution [8]:

$$\Delta r = r_{max} - r_{min}$$
$$\Delta \theta = \theta_{max} - \theta_{min}$$

As the PSD have been saved for L4, r_{max} and r_{min} are the maximum and minimum Sun radial distances measured from L4, respectively, and θ_{max} and θ_{min} are the maximum and minimum angles measured from the Sun but with origin in the L4-Sun line, also respectively.

For all of the 2062 initial conditions of the PSD, it has been found that after $T = 650$ years all of them have made, at least, one revolution. With that, the parameters Δr and $\Delta \theta$ can be computed for all the trajectories and saved with their respective initial conditions.

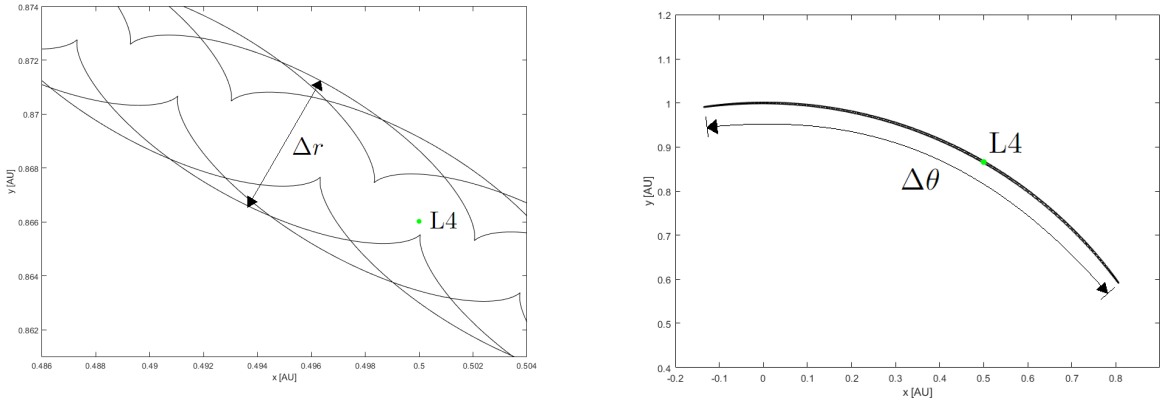

Figure 3.5: Schematic definition of the polar coordinates variations Δr and $\Delta \theta$ in a PSD orbit.

It is expected that for trajectories departing from closer points to L4, the variations of their polar coordinates will be smaller than for departing points further away from L4 [8].

After propagating for 650 years all the initial PSD conditions, for all the resultant trajectories it has been found that the maximum variation of r is of $\Delta r_{max} = 99.42557 \times 10^{-4}\ AU$, while the maximum variation of θ is of $\Delta \theta_{max} = 0.429101\ rad/2\pi$. In order to visualize each trajectory's Δr and $\Delta \theta$, the plot of the PSD can be pictured again, but this time indicating these parameters for each initial condition. Dividing the increments in 6 intervals and according to their maximums Δr_{max} and $\Delta \theta_{max}$, each interval should cover a range of $\Delta r = 0.0017\ AU$ and $\Delta \theta = 0.0715\ rad/2\pi$, as done in [8].

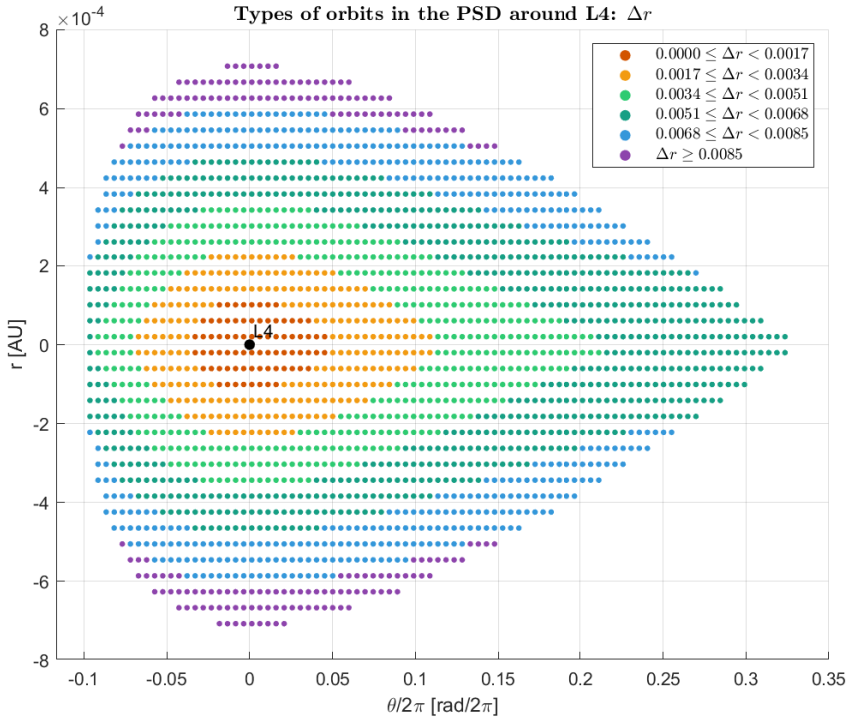

Figure 3.6: Δr for all the trajectories of the PSD.

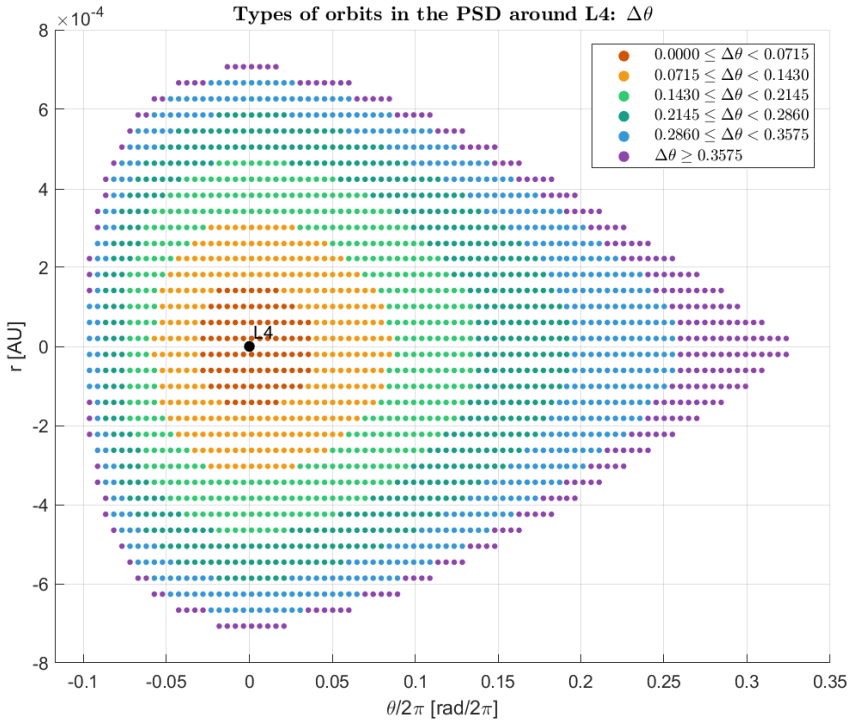

Figure 3.7: $\Delta \theta$ for all the trajectories of the PSD.

Indeed, it can be observed that when closer to L4, the resulting trajectories will have smaller variations of

their polar coordinates r and θ, while when further, the variations will be larger. However, it is important to note that the distribution of Δr and $\Delta\theta$ is slightly different over the PSD: Δr increases as the initial condition is further from L4 in the radial direction r, so it does not have to be a maximum in the region's boundary when $r = 0$, whereas $\Delta\theta$ generally increases when closer to the boundary [8].

Moreover, just in the location of the Lagrange point L4, a minimum for both variations Δr and $\Delta\theta$ can be expected, as these variations vary continuously [8].

Depending on the objective of a mission whose spacecraft is going to be placed at either L4 or L5 will lead to decide if trajectories that remain closer to L4 or that move away from it are desired. Orbits with both small Δr and $\Delta\theta$ offer a relatively static positioning of the spacecraft with respect to the Earth and the Sun. Therefore, the spacecraft would be easy to locate and communicate with from the Earth, and it could carry out observations of the Sun always from the same point of view. However, orbits with larger Δr and $\Delta\theta$ cover a large distance around the Sun in the region between almost L3 and L4 (or L5) along Earth's orbit path. Then, the spacecraft would not be located in a constant position as seen from the Earth and it would not observe the Sun always from the same point of view, but from a large angular range.

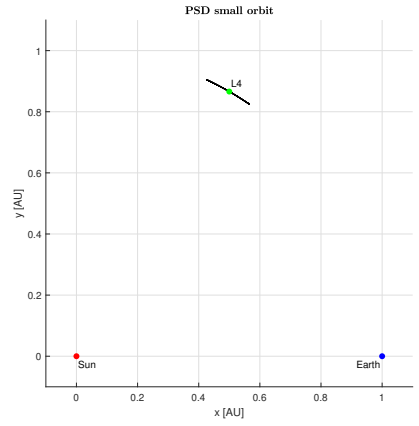

(a) $\Delta r = 8.514339 \times 10^{-4}\ AU$ and $\Delta\theta = 0.025778\ rad/2\pi$.

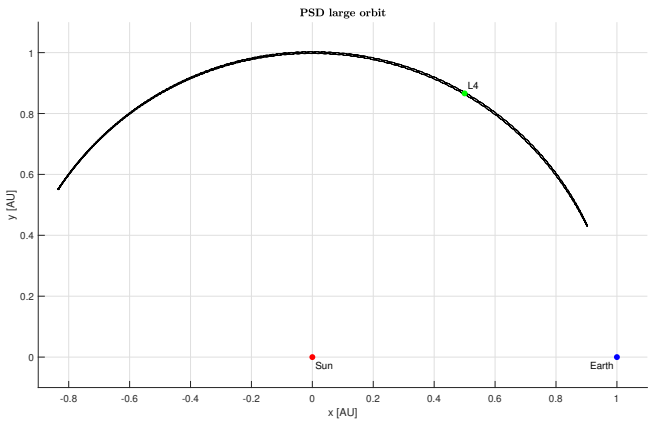

(b) $\Delta r = 68.47888 \times 10^{-4}\ AU$ and $\Delta\theta = 0.336458\ rad/2\pi$.

Figure 3.8: Examples of small and large PSD orbits in the Earth-Sun system.

Finally, the plot of the PSD is shown again, but this time with the Jacobi constants of each of the orbits starting with the initial conditions that define the PSD. The maximum Jacobi constant of all the 2062 orbits is of $C_{max} = -1.4999984738$, while the minimum is of $C_{min} = -1.5000015228$. As done in Figures 3.6 and 3.7, all the initial conditions of the PSD are divided in 6 intervals regarding their Jacobi constants, so each interval should cover a variation of $\Delta C = 5.0817 \times 10^{-7}$ according to C_{max} and C_{min}.

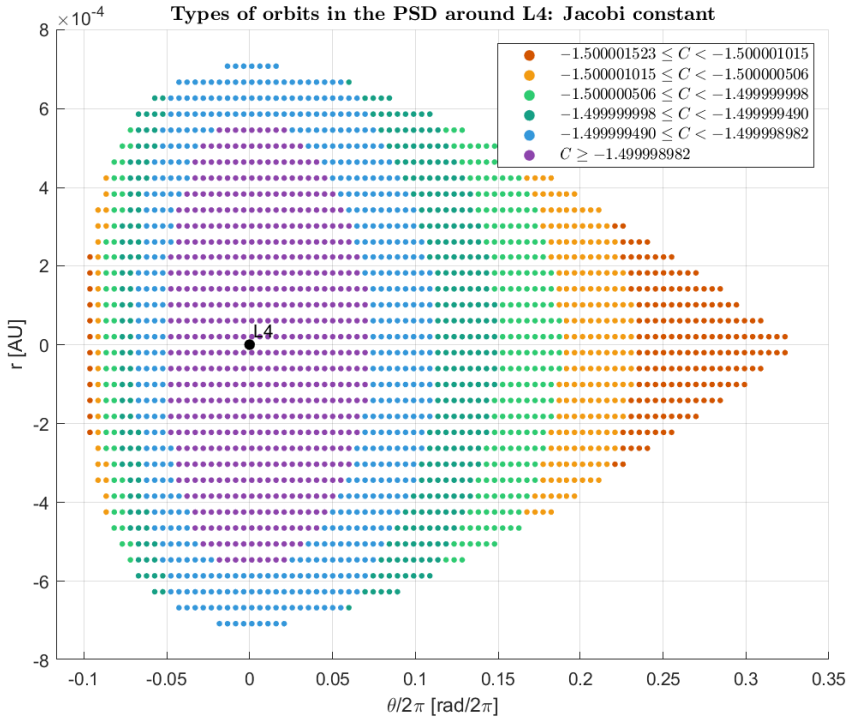

Figure 3.9: Jacobi constants for all the trajectories of the PSD.

Here, it can be seen that the Jacobi constant mainly increases when approaching L4 in the θ coordinate, although some increase can also be seen when approaching L4 in the radial direction r. Then, according to Figures 3.6 and 3.7, orbits with larger $\Delta\theta$ (and larger Δr) and further away from L4 in θ are less energetic orbits, i.e. they have smaller Jacobi constants.

All the different 2062 orbits are saved in order to have a large variety of trajectories to choose as the destination around L4 or L5, departing from either L1 or L2, whose trajectories are going to be studied in the next section.

3.3 Departure trajectories

For this section, the code used is the one in Section A.4 in the *Report Attachments* document.

As the objective of the present thesis is to find the most optimal transfers to reach L4 and L5, regarding the required impulses (which are desired to be as economical as possible), using the natural dynamics of the system is the thought way to do it. It is going to be demonstrated that, from L1 and L2 orbits, the natural dynamics of the system lead spacecraft to reach regions close to L4 or L5 without the need of performing an impulse, just by drifting away from L1 or L2 due to their instabilities. Only a ΔV shall be applied when reaching the destination point in order to get into the final PSD orbit, and another one, but which is going to be neglected, in order to drift away from the departing orbit around L1 or L2.

As the planar CR3BP is the model used, Lyapunov orbits around L1 and L2 are going to be the departing

orbits. Then, their instabilities are going to be studied in order to reach the regions around L4 and L5. These are the unstable invariant manifolds.

3.3.1 Lyapunov orbits around L1 and L2

It is known that the only planar/horizontal orbits around Lagrange points L1 and L2 are the horizontal Lyapunov orbits. These are periodic orbits that only oscillate in the x-y plane with a near-elliptic motion [14].

NASA's JPL offers a catalog of precomputed periodic orbits from different families and in different three-body systems [26]. Then, it also offers a catalog of Lyapunov orbits around L1 and L2 in the Earth-Sun system, in the framework of the CR3BP, giving their initial conditions (coordinates and velocities) as well as other parameters (such as the dimensionless Jacobi constant, the dimensionless period or the period in days) in order to propagate them. The catalog offers up to 1129 Lyapunov orbits around L1 and 1157 Lyapunov orbits around L2. Some of them and their approximate properties can be seen in the following tables and figures (in dimensionless variables, except the period, which is shown in days, for some orbit IDs):

Lyapunov orbits around L1					
ID	$\mathbf{x_0}$	$\mathbf{y_0}$	$\mathbf{vx_0}$ $[\times 10^{-15}]$	$\mathbf{vy_0}$ $[\times 10^{-2}]$	**Period (d)**
100	0.994771	0.0	−2.821417	−2.699161	199.62
200	0.996472	0.0	−1.853153	−3.817543	228.34
400	0.998017	0.0	1.702564	−5.475840	286.11
600	0.998800	0.0	−1.192244	−7.178739	343.86
800	0.999326	0.0	−16.13577	−9.648551	401.16

Table 3.1: Approximate initial conditions and periods of some of the Lyapunov orbits around L1 [26]. More precision can be obtained from NASA's JPL database [26].

Lyapunov orbits around L2					
ID	$\mathbf{x_0}$	$\mathbf{y_0}$	$\mathbf{vx_0}$ $[\times 10^{-15}]$	$\mathbf{vy_0}$ $[\times 10^{-2}]$	**Period (d)**
100	1.012590	0.0	−0.982741	−2.124622	202.82
200	1.013517	0.0	−6.055312	−2.636373	231.71
400	1.015757	0.0	−179.9427	−3.215636	289.68
600	1.018811	0.0	−243.9286	−3.772618	347.62
800	1.023504	0.0	525.7503	−4.585431	405.36

Table 3.2: Approximate initial conditions and periods of some of the Lyapunov orbits around L2 [26]. More precision can be obtained from NASA's JPL database [26].

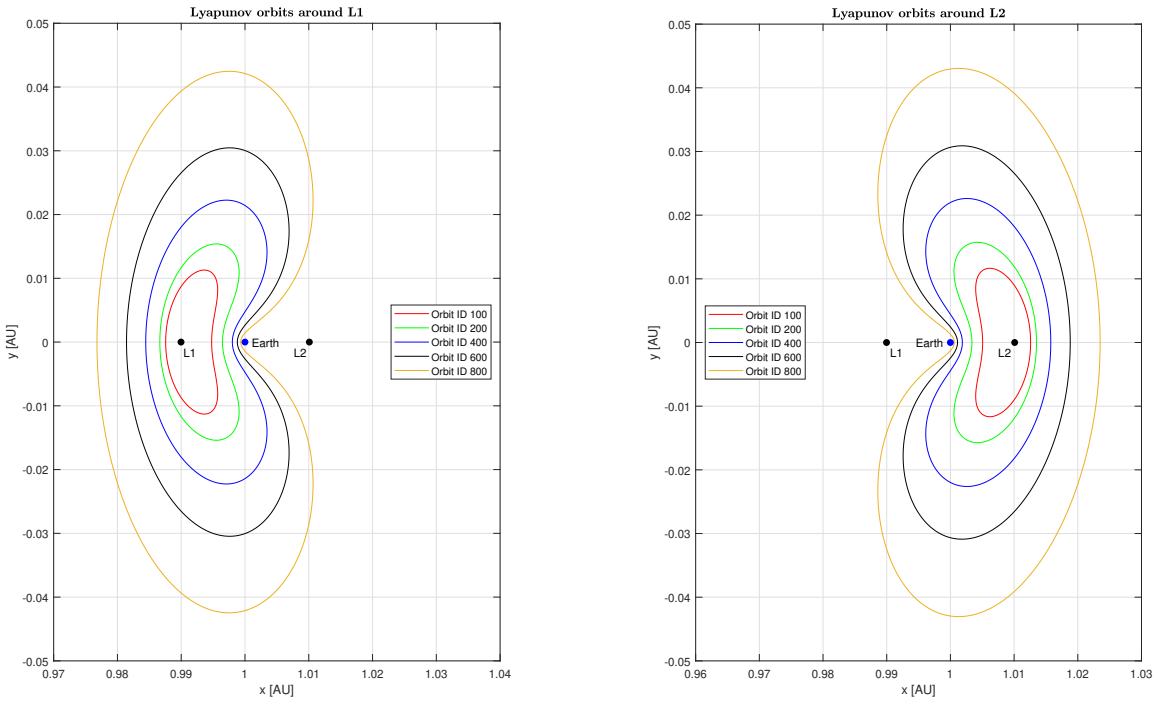

(a) Lyapunov orbits around L1.

(b) Lyapunov orbits around L2.

Figure 3.10: Some examples of Lyapunov orbits around L1 and L2.

Furthermore, it will be useful to plot the Jacobi constant (its initial value) for each of the Lyapunov orbits around L1 and L2, so that a suitable set of orbits with similar energies to those of the destination PSD orbits can be taken.

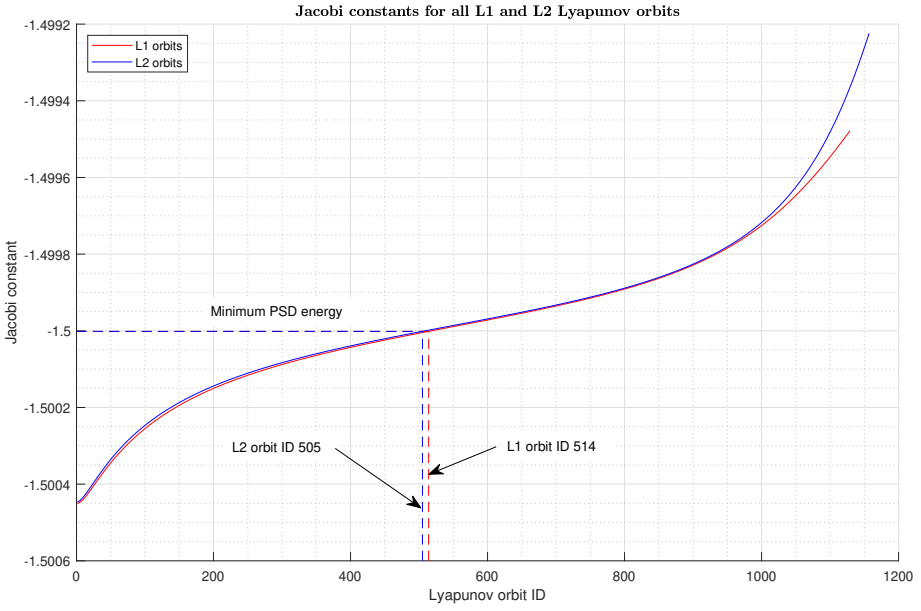

Figure 3.11: Jacobi constants of all the Lyapunov orbits around L1 and L2.

With that, energy requirements can be analyzed. When defining the necessary parameters to plot Figure 3.9 of Section 3.2, it was found that the minimum Jacobi constant of all the 2062 PSD orbits saved is of $C_{min} = -1.5000015228$. This is the minimum Jacobi constant to consider when trying to reach these PSD orbits from the departing Lyapunov orbits. Then, it has been found that L1 Lyapunov orbit ID 514 and L2 Lyapunov orbit ID 505 are the first ones to reach this minimum energy. With that, when choosing the departure orbits, those of IDs higher than 514 for L1 and higher than 505 for L2 are the only orbits to be considered in order to reach the PSD, as the difference in energy will not be as big as if lower energy Lyapunov orbits were chosen. This will allow reducing the ΔV required, as no significant energy changes will be needed.

Once the Lyapunov orbits are saved and understood, a stability analysis can be carried out.

For each of the Lyapunov orbits, the equations of motion can be solved together with the variational equations in order to find the STM of each orbit. As these are periodic and their solutions are obtained after propagating for one period, the STMs result to be the Monodromy matrices. From them, their eigenvalues and eigenvectors can be computed in order to study which are the directions of the stable and unstable manifolds of each of the Lyapunov orbits. It is important to note that, for these planar orbits in the CR3BP, four eigenvalues of the Monodromy matrix appear: one real pair and one pair equal to unity [23].

$$\lambda_1 > 1 \qquad \lambda_2 = \frac{1}{\lambda_1} < 1 \qquad \lambda_3 = \lambda_4 = 1$$

From these eigenvalues, the eigenvector corresponding to that greater than 1 represents the unstable direction, while the eigenvector corresponding to that smaller than 1 represents the stable direction [23]. These vectors have 4 elements (in the planar CR3BP): the first two represent the direction of the invariant manifold (to translate the test mass coordinates), and the second two the direction of the velocity in the manifold (to modify the velocity vector of the test mass). Indeed, this can be found when solving for all the Lyapunov orbits. Some examples can be seen next:

Lyapunov L1 orbit ID: 1

Eigenvalues:

$\left(2050.9,\ 4.8758 \times 10^{-4},\ 1,\ 1\right)$

Two first eigenvectors:

$(0.3202,\ -0.1773,\ 0.8188,\ -0.4422)$

$(0.3202,\ 0.1773,\ -0.8188,\ -0.4422)$

Lyapunov L1 orbit ID: 200

Eigenvalues:

$(404.34,\ 0.0025,\ 1,\ 1)$

Two first eigenvectors:

$(0.0506,\ -0.1600,\ 0.9352,\ -0.3119)$

$(0.0506,\ 0.1600,\ -0.9352,\ -0.3119)$

Lyapunov L2 orbit ID: 1

Eigenvalues:

$\left(1964.8,\ 5.0895 \times 10^{-4},\ 1,\ 1\right)$

Two first eigenvectors:

$(0.3367,\ -0.1682,\ 0.8180,\ -0.4350)$

$(0.3367,\ 0.1682,\ -0.8180,\ -0.4350)$

Lyapunov L2 orbit ID: 200

Eigenvalues:

$(379.19,\ 0.0026,\ 1,\ 1)$

Two first eigenvectors:

$(0.5036,\ -0.3544,\ 0.6500,\ -0.4453)$

$(-0.5036,\ -0.3544,\ 0.6500,\ 0.4453)$

In fact, there are two unstable manifolds and two stable manifolds. Both directions can be found with the respective eigenvector and with its opposite one.

Therefore, it can be seen that for Lyapunov orbits around L1, there is one unstable manifold which drifts away from L1 in the direction of increasing x and decreasing y (i.e. falls down to Earth), and there is another unstable manifold in the opposite direction, for decreasing x and increasing y (i.e. drifting away from L1 towards L4). Regarding the stable manifold, its path winds onto the Lyapunov orbit from both higher x and y coordinates in the direction of both decreasing x and y coordinates (i.e. coming up from Earth). Then, the opposite stable direction comes from lower x and y in the direction of increasing both coordinates (i.e. coming from L5 to L1).

And regarding Lyapunov orbits around L2, some similar outcomes can be obtained. Unstable manifolds are found in the directions of increasing x and decreasing y (from L2 to L5) or of decreasing x and increasing y (falling down to Earth), while stable manifolds are found in the directions of both decreasing x and y from higher x and y (up from L4 towards L2) or in the direction of both increasing x and y from smaller x and y (coming up from Earth).

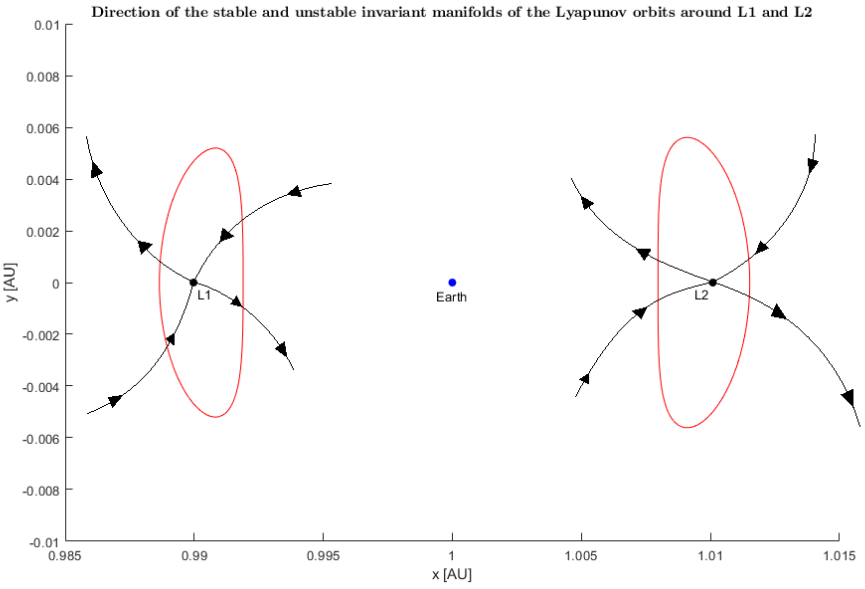

Figure 3.12: Schematic representation of the stable and unstable invariant manifolds of the Lyapunov orbits around L1 and L2.

Then, as the objective is to drift away from L1 and L2 by means of the unstable invariant manifolds so that no ΔV impulses are applied, from the previous results it can be seen that, in order to reach the RPS around L4, there is an available unstable manifold drifting away from L1. But if it is desired to reach the RPS around L5, the available unstable manifold is found to drift away from L2. Then, two important outcomes have been found in this section:

If the destination is L4 → The departing point is L1

If the destination is L5 → The departing point is L2

3.3.2 Unstable invariant manifolds

Now that the eigenvectors and eigenvalues for all the Lyapunov orbits are known, the desired unstable invariant manifolds can be computed.

First of all, according to [23], the unstable invariant manifold can be locally approximated by means of a state vector from the unstable eigenvector:

$$X^u(X_0) = X_0 + \epsilon Y^u(X_0) \tag{3.5}$$

Vector $X^u(X_0)$ is the initial guess or first approximation for the initial conditions of the test mass in order to start moving in the unstable manifold, drifting away from the periodic Lyapunov orbit at its initial conditions, which are defined by vector X_0. $Y^u(X_0)$ is the normalized eigenvector associated to the unstable eigenvalue ($\lambda_1 > 1$), which is added to the state vector of initial conditions X_0 in the periodic orbit proportionally to the parameter ϵ. This parameter sets a small displacement from the initial conditions X_0 towards the direction of the unstable manifold, specified by the eigenvector. Equation (3.5) results in a linear approximation of the manifold, so in order to not invalidate it and to not have an unfeasibly large flight time, ϵ is going to take values between 10^{-5} and 10^{-6} [23].

Once the initial conditions $X^u(X_0)$ to let drift away the test mass from the periodic orbit are known, they can be propagated over time by solving the CR3BP equations of motion. This will result in the test mass following the path of an unstable invariant manifold [23].

It is known that the sets of both unstable and stable invariant manifolds of a periodic orbit form tubes [14]. Then, the idea is to know whether these tubes intersect any point of the PSD orbits. If not, it may be because the periodic orbits around L1 or L2 may have lower energies than necessary to reach the PSD. This is why it is important to choose orbits with similar energies to those in the PSD.

There are two ways to plot these tubes: inserting the test mass in the unstable manifold with different values for ϵ from the same periodic orbit state vector X_0 (the test mass is inserted in the manifold at different distances with respect to X_0), or inserting the test mass in it with the same ϵ (same distance from the orbit) but from different positions in the periodic orbit (eigenvectors have to be propagated around the orbit with the STM). Both ways finally give the same manifold (code in Section A.6 in the *Report Attachments* document). Although the first method will be used in order to find the transfers to L4 and L5, the second one is used for the next graphics and drawings.

Next, the unstable manifold tubes (composed of 100 manifold trajectories) are pictured for both Lyapunov orbits ID 10 around L1 and L2, drifting away from L1 to L4 and from L2 to L5. Also, the propagated trajectory of one of the PSD initial conditions is also pictured (a PSD orbit with $\Delta r = 69.74797 \times 10^{-4}\ AU$ and $\Delta\theta = 0.394647\ rad/(2\pi)$).

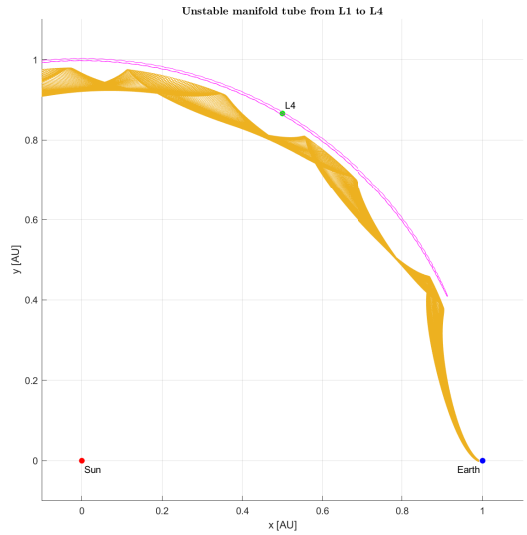

(a) Unstable manifold tube from L1 to L4.

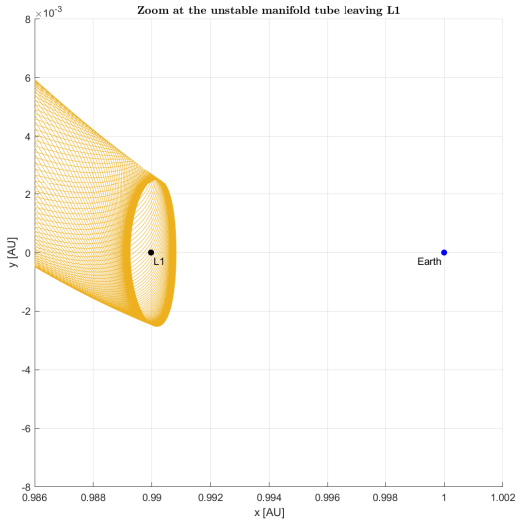

(b) Zoom at the tube when leaving L1.

Figure 3.13: Unstable manifold tube from Lyapunov L1 orbit ID 10 to L4.

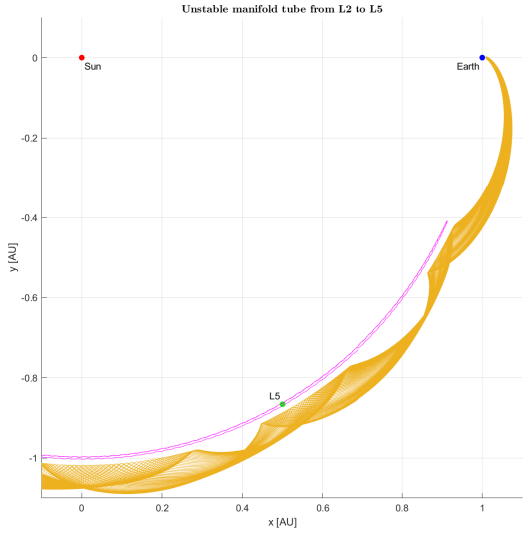

(a) Unstable manifold tube from L2 to L5.

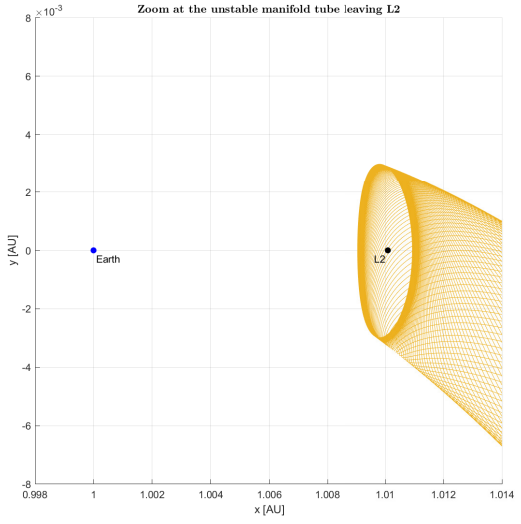

(b) Zoom at the tube when leaving L2.

Figure 3.14: Unstable manifold tube from Lyapunov L2 orbit ID 10 to L5.

From Figures 3.13a and 3.14a, it can be seen that the Jacobi constants of the departing orbits are not enough if it is desired to reach the PSD (i.e. the Lyapunov orbits do not have enough energy; the PSD remain in the forbidden region).

According to Figure 3.11, other and more energetic Lyapunov orbits can be chosen as the departing trajectories. Repeating the previous process with the same PSD initial conditions propagated but with Lyapunov orbits around L1 and L2 of ID: 1000, the following unstable manifold tubes are obtained (10 manifold trajectories are shown):

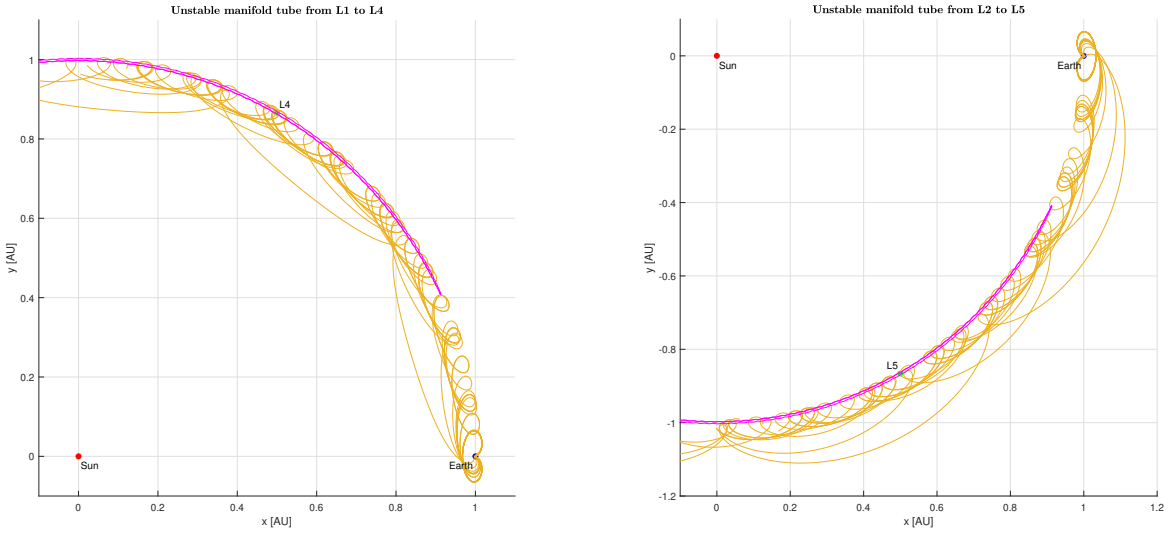

(a) Unstable manifold tube from L1 to L4.

(b) Unstable manifold tube from L2 to L5.

Figure 3.15: Unstable manifold tubes from Lyapunov L1/L2 orbits ID 1000 to L4/L5.

In these cases, it can be seen that the PSD trajectories are reached by the manifold tubes, as they are more energetic than in the previous case.

This type of manifolds can be useful to carry the spacecraft from the Lyapunov orbits to the PSD around L4 or L5 without any mid-course correction, i.e. any ΔV impulse, which means that no fuel is necessary. However, when intersecting the propagated PSD trajectory, it will be necessary to perform an impulse in order to adapt the final orbit. This final impulse is the one desired to be computed and optimized, what will be done in the following sections.

3.4 Transfers to L4 and L5

Reaching the stability regions around L4 and L5 by means of the unstable invariant manifolds can be thought to be the most inexpensive way, in terms of impulses and fuel, as the test mass (the spacecraft) takes full advantage of the natural dynamics of the CR3BP, which lead to the intrinsic instabilities of Lagrange points L1 and L2. However, as already mentioned, once the PSD are reached the spacecraft will need to perform an impulsive maneuver in order to insert itself in the final desired orbit around L4 or L5. If this impulse is not applied, the spacecraft would continue its journey through the invariant manifold, travelling around the Earth-Sun system and, eventually, maybe, colliding with any of the primaries. Then, some work has to be done in order to find which is the most optimal manifold trajectory to fly the spacecraft up to the chosen destination point in the PSD with the minimum possible ΔV.

All the propagated positions for all the trajectories that belong to the PSD are known, especially the starting points, as they have been well identified and saved as the initial conditions with 0 synodic velocity that actually define the PSD. Therefore, the first method to find some possible trajectories from L1/L2 to L4/L5 can consist of finding the best unstable manifold trajectory from a desired Lyapunov departing orbit to an

initial condition of the PSD as the destination point. As this destination point satisfies the condition of 0 synodic velocity, the ΔV impulse that the spacecraft shall apply will be equal to the modulus of its velocity in the manifold trajectory when it reaches this destination point.

3.4.1 Finding the manifolds to the PSD

In this section, a root finding problem is proposed. Given a departing Lyapunov orbit, the objective is to find which of all the possible unstable manifold trajectories drifting away from that periodic orbit reaches the desired destination point, which as mentioned earlier, will be an initial condition of the PSD.

Propagating over time a set of unstable manifold trajectories, the root finding problem is carried out regarding the distances from any point in those trajectories to the aiming point. If this distance is zero, it means that that trajectory passes through the aiming point, which means that it is in a suitable unstable manifold and, therefore, departing Lyapunov orbit, to go to the RPS around L4 or L5. The root that is desired to find is, then, when the distance d between a point in the manifold trajectory and the aiming point is $d = 0$:

$$d = \sqrt{(x_{end} - x_{fL})^2 + (y_{end} - y_{fL})^2} \tag{3.6}$$

Where (x_{end}, y_{end}) are the coordinates of the final point in the manifold trajectory, i.e. the closest point to the aiming point, and (x_{fL}, y_{fL}) are the coordinates of the aiming point.

In order to solve this root finding problem, the Newton-Raphson method [29] is going to be used (see code in Section A.5 in the *Report Attachments* document). For a given Lyapunov orbit, different absolute values of ϵ to approximate the initial state vector of the unstable manifold are going to be used, which will be the variable to find that makes the distance $d(\epsilon) = 0$. The Newton-Raphson method states that, in order to find the root position, the algorithm has to be applied iteratively as follows:

$$\epsilon_{n+1} = \epsilon_n - \frac{d(\epsilon_n)}{d'(\epsilon_n)} \tag{3.7}$$

Where n is the current iteration, so $n + 1$ is the following one, and $d'(\epsilon_n)$ is the derivative of the distance function $d(\epsilon)$ described in Equation (3.6) with respect to the ϵ variable and evaluated at the iteration n, when $\epsilon = \epsilon_n$. As only positive values for ϵ are desired, the absolute value of ϵ_{n+1} will be the one considered for the $n + 1$ iteration.

However, as the CR3BP does not have analytical solutions for the trajectory of a body, an analytical expression for $d'(\epsilon)$ can not be obtained. Then, the derivative is approximated through finite differences. Before doing that, it is important to note that finding the root of $d(\epsilon)$ from Equation (3.6) is the same as finding the root of:

$$f(\epsilon) = d^2(\epsilon) = (x_{end} - x_{fL})^2 + (y_{end} - y_{fL})^2 \tag{3.8}$$

Then, the derivative of $f(\epsilon)$ with respect to ϵ can be used instead of $d'(\epsilon_n)$, which becomes:

$$\left|\frac{df(\epsilon)}{d\epsilon}\right|_n = 2(x_{end,n} - x_{fL})\left|\frac{\partial x_{end}}{\partial \epsilon}\right|_n + 2(y_{end,n} - y_{fL})\left|\frac{\partial y_{end}}{\partial \epsilon}\right|_n \tag{3.9}$$

$$\left|\frac{df(\epsilon)}{d\epsilon}\right|_n = 2(x_{end,n} - x_{fL})\frac{x_{end,n} - x_{end,n-1}}{\epsilon_n - \epsilon_{n-1}} + 2(y_{end,n} - y_{fL})\frac{y_{end,n} - y_{end,n-1}}{\epsilon_n - \epsilon_{n-1}} \tag{3.10}$$

Replacing Equation (3.10) into Equation (3.7) (where $d(\epsilon_n)$ can also be replaced by $f(\epsilon_n)$), an algorithm can be programmed in order to find the roots ϵ, which only their absolute values will be taken so that the unstable manifold is the only one to be considered. And once the suitable ϵ value is found, the time of flight that takes to reach the aiming point can be computed as the time it takes the spacecraft, through the manifold trajectory, to reach the closest point to the aiming point, as well as the required ΔV, which can be computed as the modulus of the velocity at this closest point in the trajectory (it is important to remember that the aiming point is an initial condition of the PSD, so it has zero synodic velocity):

$$\Delta V = \sqrt{\dot{x}_{end}^2 + \dot{y}_{end}^2} \tag{3.11}$$

For the following cases, a minimum relative tolerance of 10^{-3} between the current and the previous iteration ϵ values has been imposed for the algorithm to converge. Also, the algorithm has been configured to not converge until the distance to the aiming point is less than 5×10^{-5}, as well as to consider values of ϵ between 5×10^{-4} and 10^{-7}, which can be considered to be within the linear approximation limits.

Then, taking the initial conditions of the smallest PSD orbit ($\Delta r = 2.905431 \times 10^{-4}$ and $\Delta\theta = 0.008946 rad/2\pi$), which are $x_{fL} = 0.492641$ and $y_{fL} = 0.870208$ for L4 or $x_{fL} = 0.492641$ and $y_{fL} = -0.870208$ for L5, due to the symmetry of these regions, and the Lyapunov orbits around L1 and L2 both of IDs 650, the algorithm converges offering the following results:

- L1 - L4 manifold: $\epsilon = 2.0896 \times 10^{-6}$, $\Delta V = 280.53$ m/s, $\Delta t = 8.78$ years.
- L2 - L5 manifold: $\epsilon = 1.8664 \times 10^{-6}$, $\Delta V = 288.88$ m/s, $\Delta t = 8.68$ years.

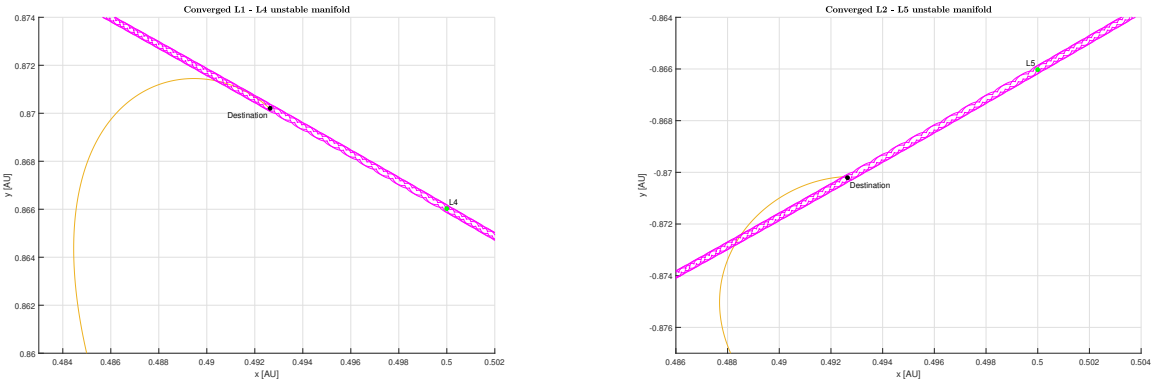

(a) L1 - L4 manifold.

(b) L2 - L5 manifold.

Figure 3.16: Zoom in the PSD orbit where the manifold trajectories reach the aiming points trying to make the distance equal to zero, from departing Lyapunov orbits of IDs 650.

And only changing the departing Lyapunov orbits to those of IDs 850 for both orbits around L1 and L2, the following results are obtained once the algorithm has converged:

- L1 - L4 manifold: $\epsilon = 9.9700 \times 10^{-6}$, $\Delta V = 489.95$ m/s, $\Delta t = 7.07$ years.
- L2 - L5 manifold: $\epsilon = 1.2875 \times 10^{-6}$, $\Delta V = 494.29$ m/s, $\Delta t = 8.82$ years.

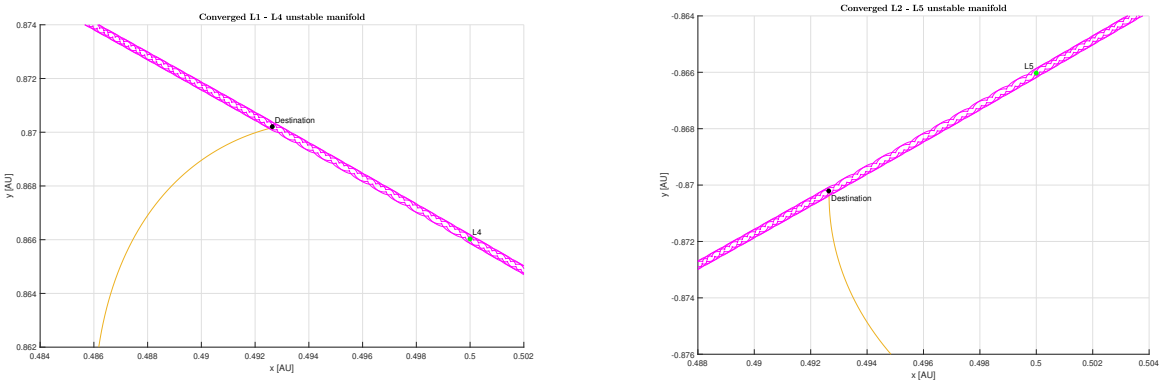

(a) L1 - L4 manifold.

(b) L2 - L5 manifold.

Figure 3.17: Zoom in the PSD orbit where the manifold trajectories reach the aiming points trying to make the distance equal to zero, from departing Lyapunov orbits of IDs 850.

For the Newton-Raphson algorithm to start iterating, two initial values have to be given to try to converge. In both of the previous cases, ϵ values of 10^{-5} and 10^{-6} are given as starting points.

Although the objective is to find the most optimal transfer trajectories that suppose the minimum ΔV, this method focuses more on the finding of the suitable manifold trajectories to reach the desired points than on reducing the needed ΔV. In fact, as all the destination points are PSD initial conditions, it has always been considered that the spacecraft, in order to adapt the final orbit, has to brake until reaching 0 synodic velocity from its final velocity in the manifold trajectory. Then, if it is not necessary to fully brake the spacecraft, the required ΔVs may be smaller.

Reducing the ΔV stands for reducing the change of velocity. In order to do that, the final velocity vector in the manifold trajectory should be very similar, in both direction and modulus, to the destination point's velocity vector in the PSD trajectory. This means that both vectors should be almost tangent to each other in the destination point and with similar modulus (see Figure 3.18). Although this last condition may be more difficult to satisfy due to differences in the types of trajectories and motion, the condition of having almost tangent and coincident velocity vectors in the aiming point can be tried to be satisfied manually.

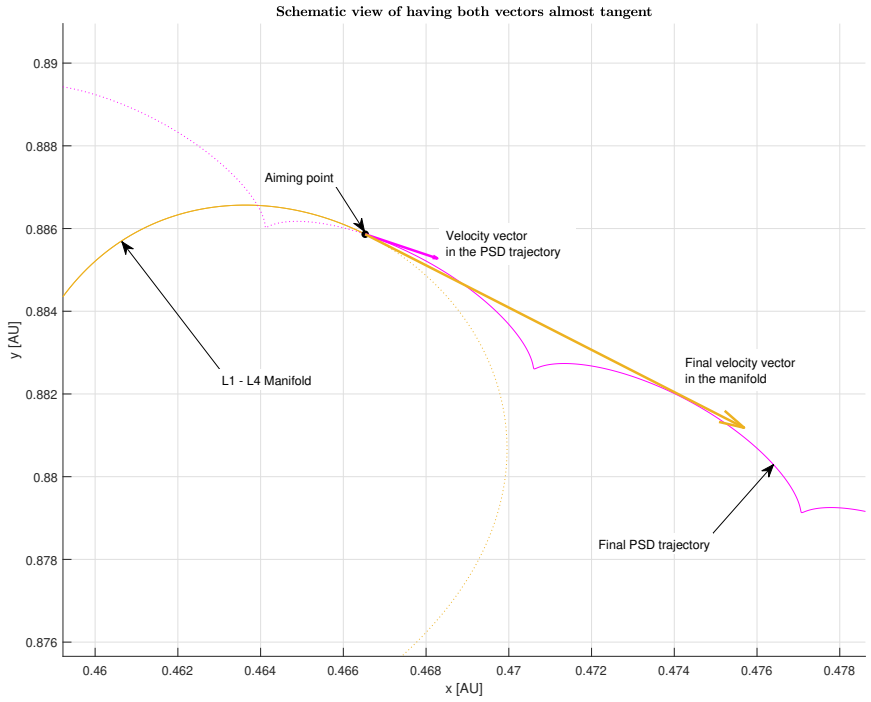

Figure 3.18: A schematic view of having an aiming point with both manifold and PSD trajectory's velocity vectors almost tangent.

3.4.2 Manual optimization with only one impulse

After many tests and tries, some conclusions have been obtained regarding the velocity behaviour in both the manifolds and the PSD orbits:

- The shapes of both types of trajectories are composed of "loopings" and less curved parts. In the loopings is where the velocity modulus gets to its minimum values, while in the middle of the less curved parts is where it gets to its maximums.

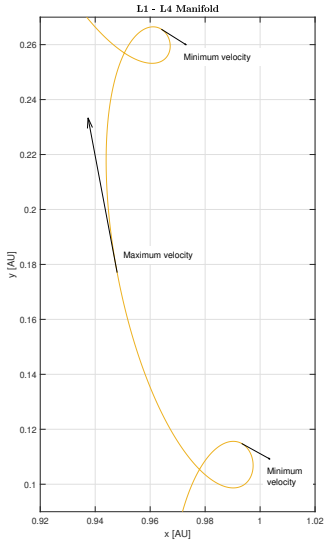

(a) Maximum and minimum velocities in a L1 - L4 manifold trajectory section.

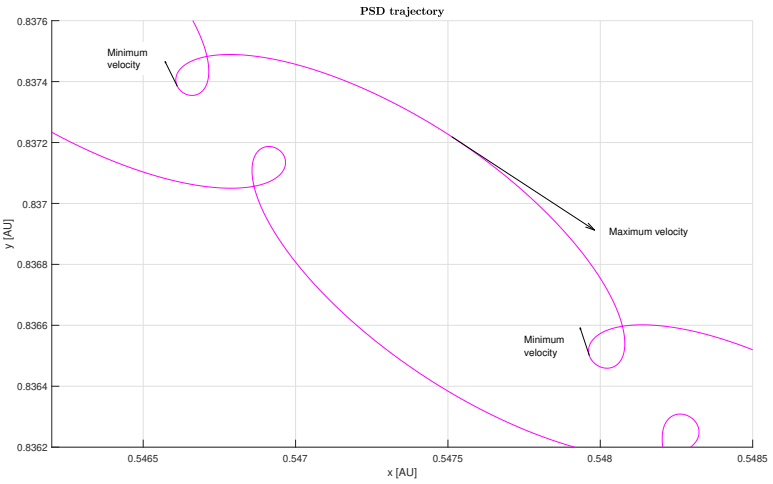

(b) Maximum and minimum velocities in a PSD orbit section.

Figure 3.19: Maximum and minimum velocities in the manifolds and in the PSD trajectories. It can be seen that the minimum velocities are located in the loopings, while the maximums in the less curved parts (vectors length scaled to the modulus of the velocity).

- For the PSD orbits, as higher is the Jacobi constant, lower is its maximum velocity (in modulus).

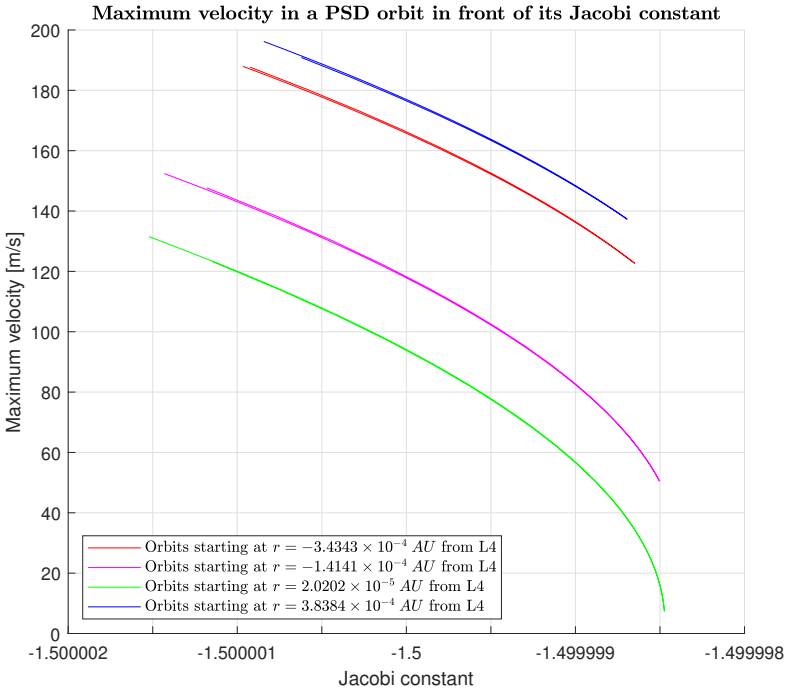

Figure 3.20: Maximum velocity in some PSD orbits depending on the Jacobi constant of that orbit. Each point of the four plotted lines refers to an orbit whose initial conditions start at the coordinates r shown in the legend but at different coordinates θ from the set K of initial conditions that define the PSD (see Section 3.1). Then, each plotted line is associated to a horizontal line of points in Figures 3.6, 3.7 and 3.9.

It is important to remember that PSD orbits with larger $\Delta\theta$ (and Δr) and further away from L4 in θ have lower energies (lower Jacobi constants, see Figure 3.9). Then, from Figure 3.20, it can be assumed that for orbits starting at the same initial condition coordinate r, when their Jacobi constants are smaller and their maximum velocities higher, their variations $\Delta\theta$ are also higher (they are orbits that cover a larger range in θ around the Sun), as they are orbits starting further away from L4 in θ.

- Regarding the minimum velocities in the manifolds, their modulus seem to increase for Lyapunov orbits of higher Jacobi constants, although this tendency is not always observed.

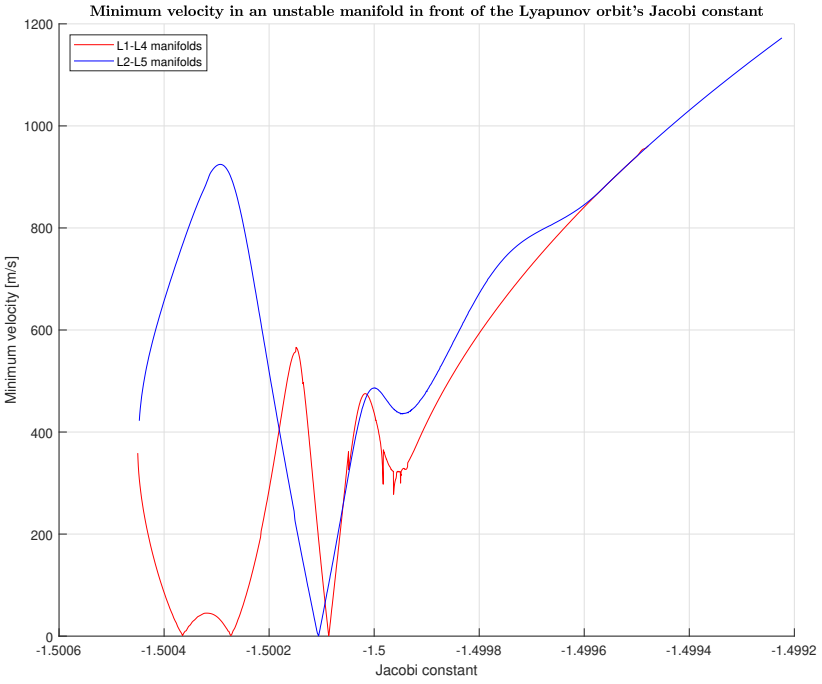

Figure 3.21: Minimum velocities in the unstable manifolds L1-L4 and L2-L5 near L4 (when $y \geq 0.3$ and $x \geq -0.5$) or L5 (when $y \leq -0.3$ and $x \geq -0.5$) with respect to the Jacobi constant of the departing Lyapunov orbit. The manifold trajectories have been propagated with $\epsilon = 10^{-5}$. However, it can be seen that there are variations in the tendencies, and the modulus of the minimum velocities only follow a growth tendency from Jacobi constants around -1.4999 and higher. Note that this graph is purely schematic to show the tendency, so the peaks that appear can be ignored.

The maximum velocities in the PSD orbits are, in general, smaller than the minimum velocities in the loopings of the unstable manifold trajectories. Then, these values limit the minimum modulus difference in the velocity vectors, and with that it is desired to try to make them tangent where this minimum difference is found: at the intersection between a manifold trajectory looping and a less curved part of a PSD trajectory. These both tangent and intersection conditions have to be found manually, as it is difficult to implement an automatic algorithm capable of doing so, because the PSD orbits should be parameterized and due to their non-periodicity is a difficult task.

Once the destination point is found (where it is desired to make the velocity vectors tangent while reducing the difference between their modulus), the time of flight is computed as the time the spacecraft takes to reach

this point through the unstable manifold from its departing Lyapunov orbit, and defining $(\dot{x}_{mf}, \dot{y}_{mf})$ and $(\dot{x}_{PSD}, \dot{y}_{PSD})$ as the velocity vectors in the aiming point just before and after applying the ΔV, i.e. in the manifold trajectory and in the final PSD orbit, respectively, the ΔV is:

$$\Delta V = \sqrt{(\dot{x}_{mf} - \dot{x}_{PSD})^2 + (\dot{y}_{mf} - \dot{y}_{PSD})^2} \tag{3.12}$$

Next, some transfers from L1/L2 to L4/L5 are shown with some of the most important parameters: departing orbit ID and Jacobi constant, ϵ parameters for the manifold trajectories, required ΔV and time of flight (codes in Sections A.6 and A.9 in the *Report Attachments* document). It is also important to remember that the PSD around L5 as well as L5's propagated orbits are obtained from those around L4. For a point (x, y) in an orbit around L4, an equivalent point can be found around L5, due to the symmetry of the problem, in the coordinates $(x, -y)$ (L4 and L5 are located symmetrically at the same place with respect to the x-axis). However, if the point (x, y) in the L4 orbit has the velocity vector (v_x, v_y), it has been seen that in the point $(x, -y)$ in the L5 orbit, the velocity vector is $(-v_x, v_y)$. This has to be taken into account for the sign of $\dot{x}_{PSD}$ in Equation (3.12).

First of all, the PSD orbit that remains closer to L4/L5 (the most energetic one in the computed PSD) is considered as the destination trajectory:

PSD destination orbit	
Jacobi constant	-1.4999984738
$\mathbf{\Delta r}$ $[AU]$	2.905431×10^{-4}
$\mathbf{\Delta\theta}$	$0.008946\, rad/2\pi = 3.2207°$

Table 3.3: Parameters of the smallest PSD orbit (see Figures 3.6 and 3.7).

According to Figure 3.20, for higher Jacobi constants, the maximum velocity in the PSD orbit is lower. Then, in order to make the required ΔV as small as possible, the minimum velocity in the manifold trajectory should also be the smallest possible. According to Figure 3.21 and to the Jacobi constant of this PSD orbit, this can be tried to be achieved departing from Lyapunov orbits of Jacobi constants around -1.5 or higher, but trying not to depart from high energy orbits, as it can be seen that the minimum velocities are, then, higher. According to Figure 3.11, this makes sense with the fact that orbits ID above 500 have to be chosen. However, L1-L4 and L2-L5 manifold trajectories, propagating them with ϵ parameters between 10^{-6} and 10^{-5}, do not intersect the aiming orbit for, approximately, the first 600 Lyapunov orbits, so the minimum velocities in the manifolds can be expected to be higher than desired, thus increasing the ΔV.

Next, and taking into account all the previous considerations, some of the found transfers are tabulated (note that C refers to the Jacobi constant of the departure Lyapunov orbit of ID also shown in the tables below):

Transfers L1 - L4				
ID	**C**	ϵ $[\times 10^{-6}]$	**ΔV** $[m/s]$	**Δt [y]**
638	-1.4999584521	3.625	261.17	8.75
642	-1.4999570179	3.250	264.12	8.76
644	-1.4999562984	2.500	268.24	8.78
720	-1.4999273428	8.500	349.68	6.92
740	-1.4999189967	9.250	369.33	6.94

Table 3.4: Transfers from L1 to the PSD destination orbit around L4.

Transfers L2 - L5				
ID	**C**	ϵ $[\times 10^{-6}]$	**ΔV** $[m/s]$	**Δt [y]**
626	-1.4999599735	1.750	254.40	8.61
629	-1.4999589194	1.375	257.68	8.60
655	-1.4999496420	2.875	287.14	7.68
703	-1.4999315965	4.000	338.04	6.74
777	-1.4998999570	5.125	411.21	5.84

Table 3.5: Transfers from L2 to the PSD destination orbit around L5.

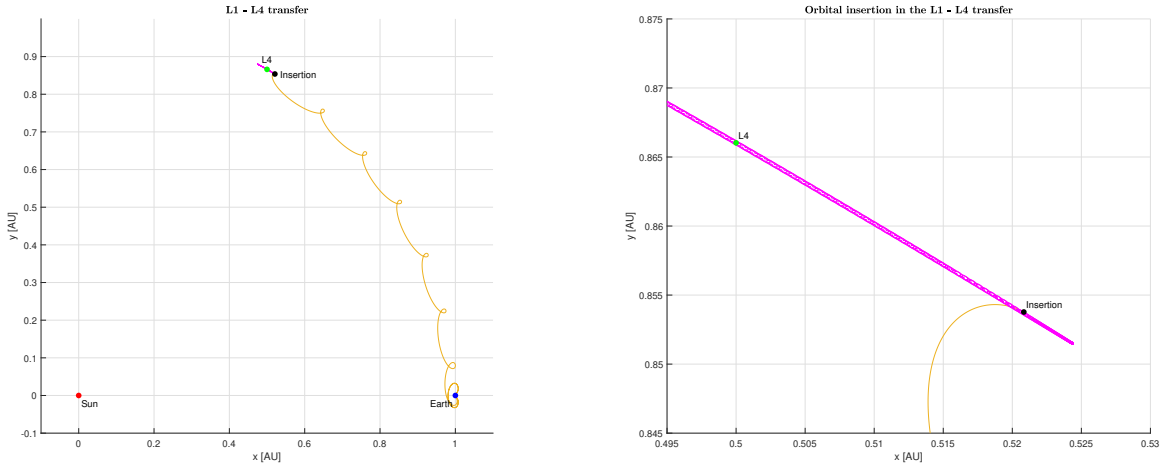

(a) L1-L4 transfer.

(b) Orbital insertion in the L1-L4 transfer.

Figure 3.22: L1-L4 transfer from Lyapunov L1 orbit ID 638 with $\epsilon = 3.625 \times 10^{-6}$.

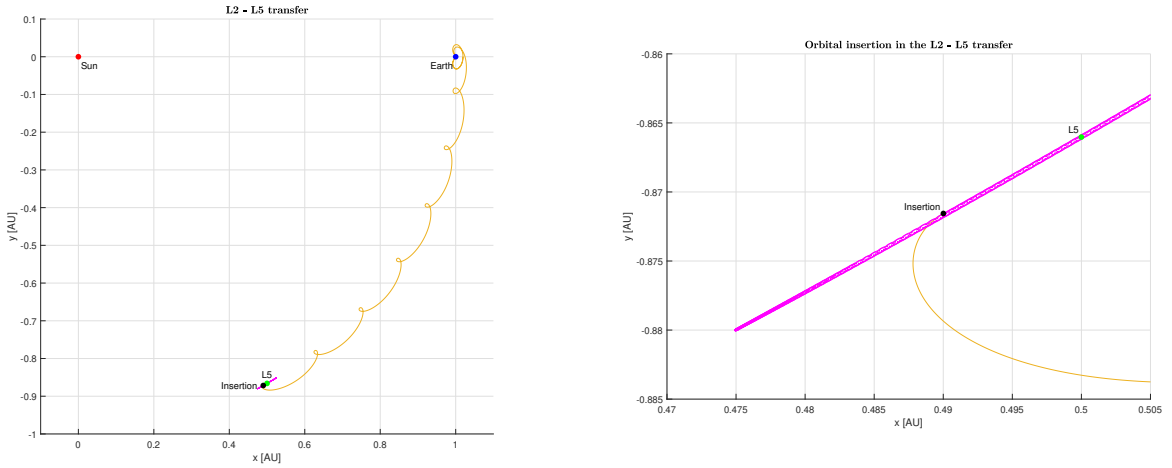

(a) L2-L5 transfer.

(b) Orbital insertion in the L2-L5 transfer.

Figure 3.23: L2-L5 transfer from Lyapunov L2 orbit ID 626 with $\epsilon = 1.750 \times 10^{-6}$.

In order to get to the smallest PSD orbit in terms of Δr and $\Delta\theta$, it can be seen that a minimum ΔV of the order of 260 m/s is required when going to L4 from L1, or of the order of 250 m/s when going to L5 from L2. Furthermore, in both cases it can be seen that the time of flight is of approximately more than 8.5 years when travelling through the most optimal transfers. Moreover, when increasing the departure orbit's energy (higher orbit's IDs), and as mentioned previously in Figure 3.21, the minimum velocities in the manifolds are higher, so that explains why the ΔVs are, then, higher. However, in those cases the time of flight is reduced.

Now, another PSD orbit is going to be considered as the destination. In this case, it is going to be another small orbit in terms of Δr and $\Delta\theta$, but of lower energy than the previous one:

PSD destination orbit	
Jacobi constant	-1.4999984786
$\mathbf{\Delta r}$ $[AU]$	4.042469×10^{-4}
$\mathbf{\Delta\theta}$	$0.014940\, rad/2\pi = 5.3785°$

Table 3.6: Parameters of a PSD orbit of $\Delta\theta \approx 5°$ (see Figures 3.6 and 3.7).

According to Figure 3.20, for a PSD orbit of lower energy its maximum velocity is higher. Departure orbits of lower Jacobi constant should also be possible to reach this destination trajectory, and, again, according to Figure 3.21, the minimum velocities in the manifolds should also be expected to be lower, thus reducing the ΔV. However, as it is desired to reach the upper part of the PSD trajectories to make the velocity vectors tangent in the same direction and Δr has increased for this orbit compared with the previous one, departure orbits of slightly higher Jacobi constants are eventually needed. The next cases have been found as the first manifold trajectories to intersect the destination's PSD orbit in the desired way (tangential velocity vectors):

Transfers L1 - L4				
ID	**C**	ϵ $[\times 10^{-6}]$	**ΔV** $[m/s]$	**Δt [y]**
642	-1.4999570179	2.875	262.38	8.76
644	-1.4999562984	3.250	263.93	8.78
644	-1.4999562984	2.500	265.00	8.76

Table 3.7: Transfers from L1 to the PSD destination orbit around L4.

Transfers L2 - L5				
ID	**C**	ϵ $[\times 10^{-6}]$	**ΔV** $[m/s]$	**Δt [y]**
629	-1.4999589194	1.750	255.56	8.61
634	-1.4999571559	1.375	261.28	8.60
642	-1.4999543150	2.500	274.97	7.64

Table 3.8: Transfers from L2 to the PSD destination orbit around L5.

With that, no noticeable changes in both the ΔVs and the time of flight can be seen. Therefore, it can be expected that the most optimal way to reach the PSD requires around 260 m/s and 8.5 years of flight time.

Next, one bigger destination orbit and, then, of lower energy is going to be studied and compared with the previous cases:

PSD destination orbit	
Jacobi constant	-1.4999984787
Δr $[AU]$	8.514339×10^{-4}
$\Delta\theta$	$0.025778\, rad/2\pi = 9.2800°$

Table 3.9: Parameters of a PSD orbit of $\Delta\theta \approx 10°$ (see Figures 3.6 and 3.7).

Transfers L1 - L4				
ID	**C**	ϵ $[\times 10^{-6}]$	**ΔV** $[m/s]$	**Δt [y]**
653	-1.4999530402	2.875	263.70	8.79
654	-1.4999526760	3.250	264.48	8.79
656	-1.4999519462	3.625	266.63	8.80

Table 3.10: Transfers from L1 to the PSD destination orbit around L4.

Transfers L2 - L5				
ID	**C**	ϵ $[\times 10^{-6}]$	**ΔV** $[m/s]$	**Δt [y]**
640	-1.4999550275	1.750	256.86	8.63
642	-1.4999543150	2.125	261.95	8.64
646	-1.4999528850	1.375	263.67	8.62

Table 3.11: Transfers from L2 to the PSD destination orbit around L5.

Again, no noticeable changes are observed for both the ΔVs and the flight times, despite a slight increase in the ΔVs as the destination PSD orbit is bigger in terms of Δr and $\Delta\theta$.

Finally, in order to see if these results change more noticeably, an even bigger PSD orbit is studied:

PSD destination orbit	
Jacobi constant	-1.4999985484
Δr $[AU]$	26.38214×10^{-4}
$\Delta\theta$	$0.082381\, rad/2\pi = 29.657°$

Table 3.12: Parameters of a PSD orbit of $\Delta\theta \approx 30°$ (see Figures 3.6 and 3.7).

Transfers L1 - L4				
ID	**C**	ϵ $[\times 10^{-6}]$	**ΔV** $[m/s]$	**Δt [y]**
696	-1.4999368950	6.625	270.91	8.86
700	-1.4999353341	4.375	276.00	8.88

Table 3.13: Transfers from L1 to the PSD destination orbit around L4.

Transfers L2 - L5				
ID	**C**	ϵ $[\times 10^{-6}]$	**ΔV** $[m/s]$	**Δt [y]**
688	-1.4999373919	2.125	271.74	8.72
705	-1.4999308112	2.875	286.62	7.71

Table 3.14: Transfers from L2 to the PSD destination orbit around L5.

It is important to note that, in this type of larger PSD trajectories (bigger $\Delta\theta$), one same manifold trajectory intersects it in different suitable points. Although the required ΔV in these points may all be similar, applying it further away from L4/L5 would reduce or increase the time of flight, depending on the fact that the destination point would be reached before or after L4/L5, respectively. However, being further from L4/L5 would also lead to be inserted into a larger final orbit, in terms of $\Delta\theta$, which may not be desired if the objective is to remain as close as possible to the libration point. Furthermore, it is important to note that every oscillation or section between two loopings in both the manifold trajectory and the PSD trajectory

takes one period of the synodic system, i.e. one year, so making the orbital insertion closer to L4 or L5 would help to remain closer to these libration points during a long period of time, which may be desired instead of inserting onto orbit farther from the equilibrium point.

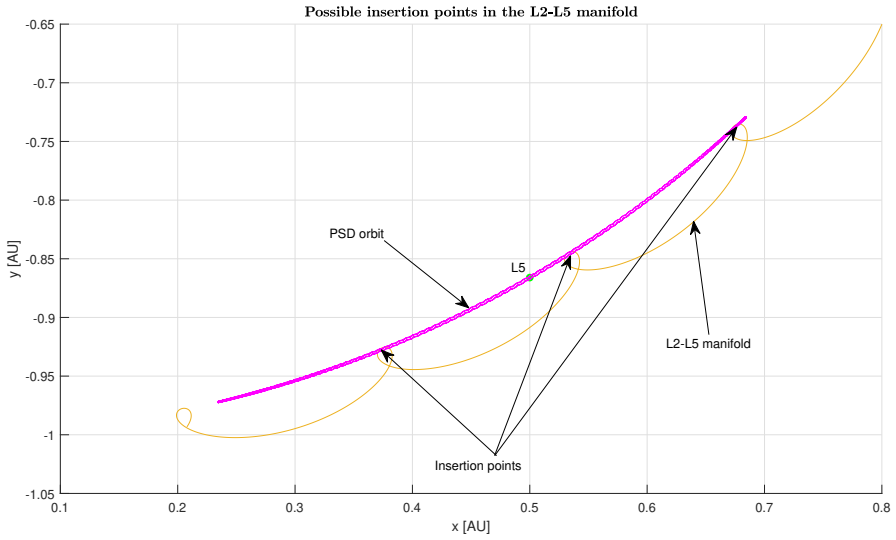

Figure 3.24: Different possible insertion points from the L2-L5 manifold of the Lyapunov L2 orbit ID 705.

Besides this, the previous results are all similar to the other situations: ΔVs of the order of 260 m/s and flight times between 8.5 and 9 years are required in order to reach the RPS around L4 or L5 from L1 or L2.

3.4.3 Manual optimization with two impulses

In this last section, a two impulse maneuver is going to be considered in order to try to improve the most optimal transfers found in the previous section (see codes in Sections A.7, A.8 and A.9 in the *Report Attachments* document). Besides the final orbital insertion ΔV (now referred to as ΔV_2), another ΔV_1 is going to be applied as a mid-course correction burn before getting to the RPS. This ΔV_1 is going to be carried out tangentially to the spacecraft's trajectory at 30° above and below the Sun-Earth segment, for L1-L4 and L2-L5 manifolds, respectively.

Three different impulses of 25, 50 and 100 m/s are going to be analyzed for this case.

As in the previous section, the first PSD orbit to reach for is the most energetic one, having the smallest Δr and $\Delta\theta$ (see Table 3.3).

First of all, performing a ΔV_1 impulse of 25 m/s, the following two most optimal transfers to L4 and L5 are obtained:

Transfers to L4 and L5					
ID	**C**	ϵ $[\times 10^{-6}]$	**ΔV** $[m/s]$	**t_1 [y]**	**Δt [y]**
L1 491	-1.5000094450	1.375	276.35	5.11	8.51
L2 476	-1.5000114227	1.000	269.62	4.82	8.42

Table 3.15: Transfers from L1/L2 to the PSD destination orbit around L4/L5.

Here, ΔV accounts for the sum of both ΔV_1 and ΔV_2 and Δt for the sum of both t_1 and t_2 (this one not shown in the tables), which are defined as the flight time needed by the spacecraft to reach, through the manifold trajectory, the point where ΔV_1 is applied and the flight time needed to reach the aiming point in the final orbit since the application of ΔV_1, respectively. Therefore, Δt accounts, again, for the whole flight time.

From Table 3.15, it can be concluded that the results do not differ from the ones obtained in the previous section. However, the spacecraft is able to depart from lower energy Lyapunov orbits. In fact, the mid-course ΔV_1 adds the necessary energy so that the spacecraft can then reach the PSD orbit.

Next, the same computations are carried out taking as the destination a 10° orbit in the PSD, whose characteristics have already been defined in Table 3.9.

Transfers to L4 and L5					
ID	**C**	ϵ $[\times 10^{-6}]$	**ΔV** $[m/s]$	**t_1 [y]**	**Δt [y]**
L1 507	-1.5000038507	1.750	286.22	5.08	8.54
L2 489	-1.5000068845	1.000	267.02	4.87	8.43

Table 3.16: Transfers from L1/L2 to the PSD destination orbit around L4/L5.

Again, similar results are obtained.

As the application of the ΔV_1 allows the test mass to depart from lower energy orbits, if their manifold trajectories maximum velocities are higher, it may help to travel faster until reaching the ΔV_1 application point, thus reducing the total flight time. Therefore, applying higher ΔV_1s may allow the spacecraft to depart from even lower energy Lyapunov orbits and to reduce the time of flight (if the maximum velocities are higher).

Similarly to Figure 3.21, the maximum velocities in the unstable manifolds with respect to the Jacobi constant of their Lyapunov orbits can be plotted:

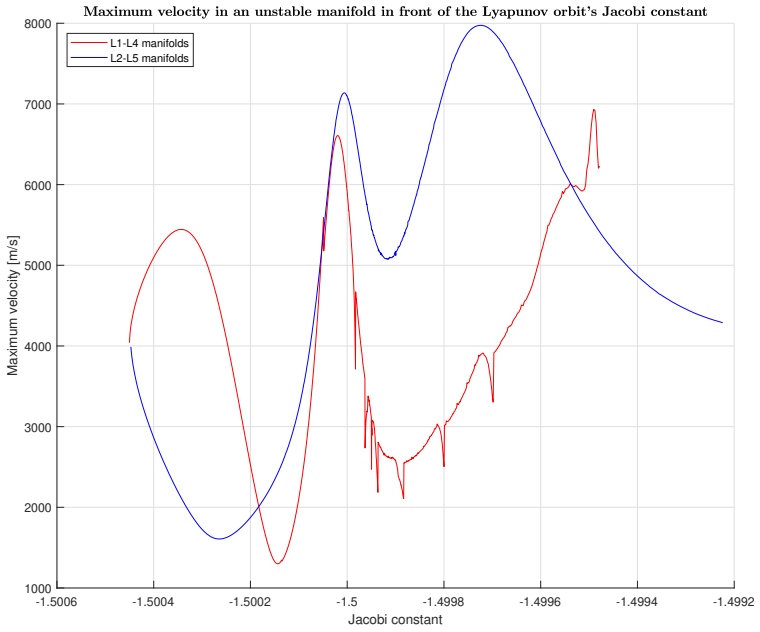

Figure 3.25: Maximum velocities in the unstable manifolds L1-L4 and L2-L5 near L4 (when $y \geq 0.3$ and $x \geq -0.5$) or L5 (when $y \leq -0.3$ and $x \geq -0.5$) with respect to the Jacobi constant of the departing Lyapunov orbit for all orbits IDs. The manifold trajectories have been propagated with $\epsilon = 10^{-5}$. Also note that this graph is purely schematic to show the tendency, and the peaks that appear can be ignored.

Applying $\Delta V_1 = 50\, m/s$ in order to get to the PSD orbit defined in Table 3.3, the following transfers are obtained:

Transfers to L4 and L5					
ID	**C**	ϵ $[\times 10^{-6}]$	**ΔV** $[m/s]$	**t_1 [y]**	**Δt [y]**
L1 374	-1.5000537865	1.375	290.98	4.86	8.28
L2 372	-1.5000506023	1.375	560.22	2.77	4.36

Table 3.17: Transfers from L1/L2 to the PSD destination orbit around L4/L5.

Here, two different situations can be seen: the first one has similar results to the previous ones, but the second one, although having a relatively small minimum manifold velocity according to both Figures 3.11 and 3.21 (Lyapunov orbit around L2 of ID 372), it has a higher maximum velocity, as seen in Figure 3.25. This reduces t_1, and also t_2 because ΔV_1 is applied near the point of maximum velocity in the manifold trajectory. However, this also increases the minimum velocity, and with that, the difference in modulus at the orbital insertion point.

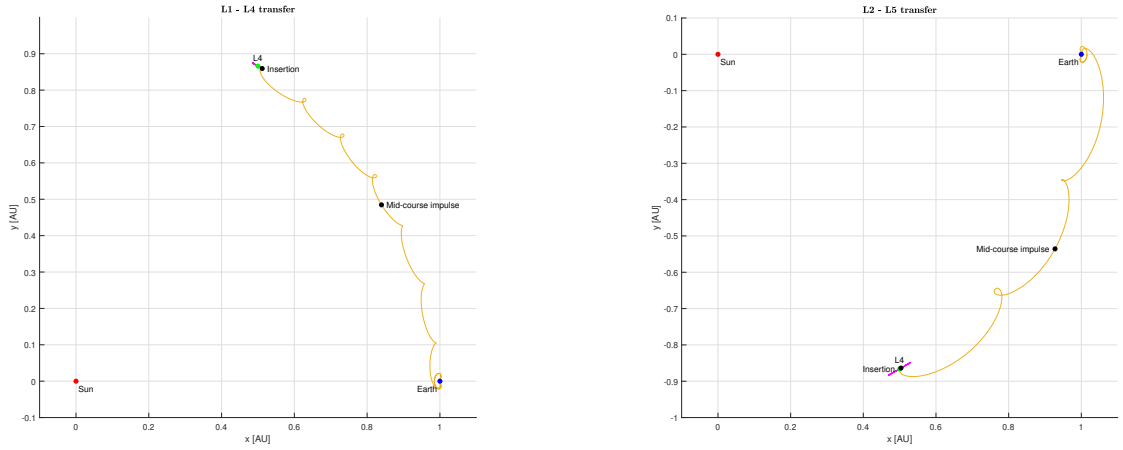

(a) L1-L4 transfer.

(b) L2-L5 transfer.

Figure 3.26: Different situations for the L1-L4 and L2-L5 transfers applying a 50 m/s mid-course impulse.

Therefore, the most suitable departing Lyapunov orbits can be considered to be those with the highest maximum manifold velocities, in order to reduce the time of flight, but that once ΔV_1 is applied, the resulting manifold trajectories could intersect the destination orbit so that ΔV_2 would be reduced.

Then, a $\Delta V_1 = 100\, m/s$ is going to be applied to get to the same PSD orbit as in the previous case.

Transfers to L4 and L5					
ID	**C**	ϵ $[\times 10^{-6}]$	**ΔV** $[m/s]$	**t_1 [y]**	**Δt [y]**
L1 115	-1.5002346489	10.00	643.99	1.99	3.45
L1 266	-1.5001063974	8.875	400.14	3.61	6.18
L2 115	-1.5002264979	4.000	565.40	2.35	3.99
L2 151	-1.5001862120	7.375	460.73	2.59	5.09

Table 3.18: Transfers from L1/L2 to the PSD destination orbit around L4/L5.

These results do not show any improvement regarding the earlier mentioned hypothesis. This may be due to the position where ΔV_1 is applied, as depending on the type of unstable manifold trajectory, it would be better to apply it at one or at another location. In order to find this point, an automatic algorithm may be needed to study its effect in all the possible manifolds for all the Lyapunov orbits.

Nonetheless, the tendency that has been observed until now during all the previous situations maintains: greater ΔVs lead to shorter flight times.

Finally, before finishing this chapter, an impulse of $\Delta V_1 = 100\, m/s$ is going to be applied in order to reach the same smallest PSD orbit (Table 3.3), but at 50° above and below the Sun-Earth segment instead of at 30°, to take advantage of lower energy and, possibly, faster unstable manifolds during a longer part of the transfer, trying to reduce the total flight time. Some of the transfers found are the following:

Transfers to L4 and L5					
ID	**C**	ϵ $[\times 10^{-6}]$	**ΔV** $[m/s]$	**t_1 [y]**	**Δt [y]**
L1 115	-1.5002346489	8.500	595.58	2.98	3.45
L1 209	-1.5001434950	3.625	478.86	4.52	5.07
L2 97	-1.5002509535	1.750	768.74	2.55	3.01
L2 115	-1.5002264979	4.375	541.61	3.43	4.00

Table 3.19: Transfers from L1/L2 to the PSD destination orbit around L4/L5.

The firsts manifold trajectories to intersect the destination PSD orbit show slightly shorter times of flight, but then needing high ΔVs. Notwithstanding this, both L1 and L2 orbits of ID 115 seem to provide better results when compared to the previous ones in Table 3.18, as the same flight times are maintained with smaller ΔVs, claiming that the application of ΔV_1 has been better placed for this case.

All the results obtained in this section show that when increasing the ΔV, the time of flight will be shorter, although performing a mid-course ΔV impulse does not seem to improve significantly the results when compared to the case with only one impulse. Apart from this, it is important to note that a big amount of possibilities are open in order to decide which is the most suitable for a spacecraft and for its mission, being the cheaper ones an impulse of the order of 260 m/s and a flight time of over 8.5 years, without any mid-course impulse. With all these results, further conclusions are being stated in the following sections.

Chapter 4

Results discussion

In this section, a summary of all the previous results is going to be made as well as a discussion about them. Moreover, the tolerances and options used in the solvers and codes are going to be summarized in order to state the validation of the results.

4.1 Summaries and comparisons

The most important conclusion that has been obtained from all the results in Section 3.4 may be that there are not limited transfers to reach L4 and L5, but that there is a large variety of possible transfer trajectories to choose according to the mission requirements and spacecraft specifications and depending on the energy of the departure orbits. It has been seen that it is possible both to perform low ΔV impulsive maneuvers with long times of flight as well as higher ΔV impulsive maneuvers with shorter times of flight. For all the results obtained, the following Tables cover a summary of the average ΔVs and times of flight (note that they are shown to help get an idea about the required values):

Summary of transfers from L1 to L4	
ΔV [m/s]	**Δt [years]**
260 - 270	8.75 - 8.80
270 - 290	8.25 - 8.50
300 - 400	6.00 - 7.50
450 - 600	3.50 - 5.00

Summary of transfers from L2 to L5	
ΔV [m/s]	**Δt [years]**
250 - 260	8.50 - 8.65
270 - 280	7.70 - 8.50
300 - 400	6.00 - 7.50
450 - 750	3.00 - 5.00

Table 4.1: Summary of the ΔVs and times of flight required for the transfers from L1/L2 to L4/L5, including both one and two impulsive maneuvers.

Furthermore, the most optimal transfers found, in terms of the ΔV, from L1 to L4 and from L2 to L5 are the following (from Tables 3.4 and 3.5):

- **L1 - L4 transfer:** $\Delta V = 261.17\, m/s$ and $\Delta t = 8.75\, y$
- **L2 - L5 transfer:** $\Delta V = 254.40\, m/s$ and $\Delta t = 8.61\, y$

Although both transfers to L4 and L5 have similar ΔV budgets and flight times, it seems that flying from L2 to L5 is the cheapest way in terms of ΔV, while also reducing the time of flight when compared to the most optimal transfer from L1 to L4.

With these results, it can be checked that, indeed, L4 and L5 are difficult locations to reach due to the long flight times required when performing the lowest ΔV impulses. However, times of flight between 8 and 9 years can be comparable to other current and past interplanetary missions. For instance, the recently launched Jupiter Icy Moons Explorer (Juice) ESA mission is going to spend around eight years cruising to Jupiter while completing several flybys of Venus, Earth and the Moon [30], and its spacecraft is designed for a high ΔV capability of $2700\, m/s$ [31]. Moreover, the NASA/ESA/ASI Cassini-Huygens mission took 7 years to get to Saturn [32] [33], and the NASA Juno mission to Jupiter needed 5 years of cruise flight, completing an Earth flyby [34]. Closer to Earth, the NASA's OSIRIS-REx spacecraft traveled to the near-Earth asteroid Bennu after launch in 2016, and it is expected to bring back samples to Earth in 2023, covering a flight time of also around 7 years [35]. Furthermore, only in its first deep space maneuver, the OSIRIS-REx spacecraft performed an impulse of $431\, m/s$ of ΔV [36]. Therefore, it can be seen that both the times of flight and the ΔVs required are comparable to current space missions.

L1 and L2 are locations easier to reach (the JWST only needed 29 days to reach its orbit around L2 [37]) and the orbits around them require very small station-keeping maneuvers (low ΔV). However, L4 and L5 orbits are stable, so no station-keeping is required: the spacecraft does not need to carry more fuel to maintain its orbit, but just for any possible maneuver or orbit readjustment.

To sum up, long times of flight are required to reach the RPS around L4 and L5, which could be expected knowing how far away they are. However, it has been seen that both times of flight and ΔVs are reasonable when compared to other interplanetary missions, and if it is desired to reduce the flight times, the required ΔVs would still be reasonable.

4.2 Validation of the results

As the resolution of the CR3BP is done numerically, it is important to check and validate the results within a certain tolerance. In this problem, it has been seen that the Jacobi constant, i.e. the total energy in a trajectory, has to remain constant. Then, this is the best way to check the validity of the results: if the Jacobi constant does not vary during all the propagation of an initial set of conditions, within a certain tolerance, the results can be considered to be accurate enough. In the present thesis, a minimum tolerance of 10^{-8} was defined in the requirements section 1.4.

In the MATLAB codes used, the following options were chosen:

- **Solver:** *ode89*. According to MATLAB documentation, this is a solver capable of solving nonstiff differential equations with a high order method. It implements Verner's "most robust" Runge-Kutta 9(8) pair with an 8th-order continuous extension [38]. It is a high precision solver such as the *ode78* (it implements Verner's "most efficient" Runge-Kutta 8(7) pair with a 7th-order continuous extension [39]), but the *ode89* is designed to be more accurate when propagating for larger periods of time and/or for stricter tolerances [40], which is the case.
- **Relative tolerance:** $RelTol = 10^{-13}$. A more stricter tolerance than 10^{-8} is defined to get even more accurate results and to avoid variations of the Jacobi constant.
- **Maximum step size:** $MaxStep = 10^{-1}$.

It is important to note that not all codes are defined with these options. When computing the PSD first and second approximations as well as the orbits in these regions, the relative tolerance has been set to 10^{-8} as defined in the requirements. Then, for the PSD approximations an automatic maximum step size is set by the *ode89* solver, while for the PSD orbits is set to $MaxStep = 2 \times 10^{-1}$, as they have to be saved and well mapped. This is done in order to reduce the amount of memory used during the computations as well as the computation times, due to the large amount of initial conditions that are considered.

All these parameters make the results accurate enough, as the Jacobi constant does not change significantly, which can be seen in the following Figures (the variation of the Jacobi constant is plotted with respect to its first value in the propagation):

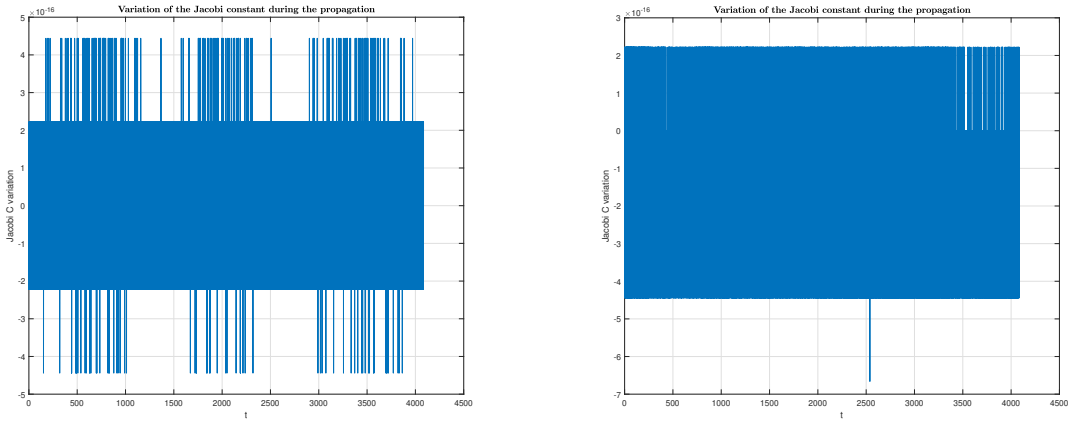

(a) Variation of the Jacobi constant for the smallest PSD orbit ($\Delta r = 2.905431 \times 10^{-4}\ AU$ and $\Delta\theta = 0.008946\ rad/2\pi$).

(b) Variation of the Jacobi constant for one of the biggest PSD orbit ($\Delta r = 99.42557 \times 10^{-4}\ AU$ and $\Delta\theta = 0.417716\ rad/2\pi$).

Figure 4.1: Variations of the Jacobi constant for PSD orbits, with $RelTol = 10^{-8}$ and $MaxStep = 2 \times 10^{-1}$.

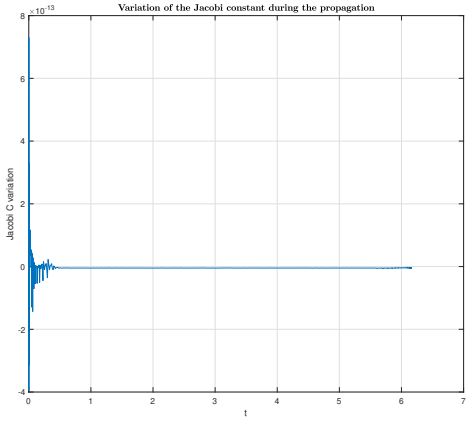

(a) Variation of the Jacobi constant for Lyapunov orbit ID 650 around L1.

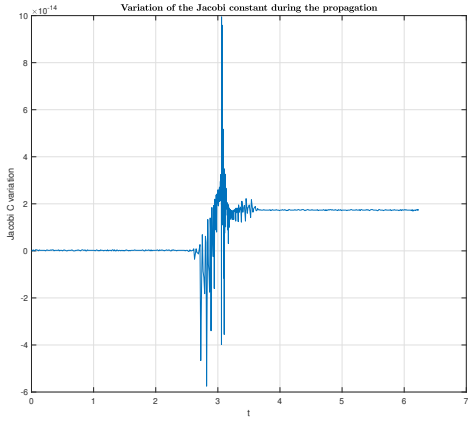

(b) Variation of the Jacobi constant for Lyapunov orbit ID 650 around L2.

Figure 4.2: Variations of the Jacobi constant for Lyapunov orbits around L1 and L2, with $RelTol = 10^{-13}$ and $MaxStep = 10^{-1}$.

The maximum oscillations of the order of between 10^{-13} and 10^{-16} can be considered to be accurate enough.

Finally, it is important to note that, from all the eigenvalues obtained for all the cataloged Lyapunov orbits, not all of them satisfy the fact that there appear one real pair and one pair equal to unity. In some cases, the pair of eigenvalues that should be equal to unity are different from 1, although they are in the same order of magnitude. For example, for Lyapunov orbit around L1 ID: 1116, these eigenvalues are not equal and equal to unity, but they are 1.3169 and 0.7594. During the development of the codes for the present thesis, the precision of the solver was changed several times, although the relative tolerance was eventually increased to 10^{-13} for the resolution of the variational equations and the maximum step size was decreased to a minimum of 0.1, as said earlier. However, the time step of the solver seemed to influence in the trajectory results, and in some orbits the periodicity is not precisely achieved, leading to the problem that eigenvalues λ_3 and λ_4 are different from 1. Nonetheless, eigenvalues λ_1 and λ_2 satisfy their characteristics, and as they are the values to consider in order to work with the manifolds, no other changes were made. In fact, for this Lyapunov L1 orbit 1116, the distance between the initial point and the final propagation point is of 1.336×10^{-10}, smaller than the required minimum tolerance of 10^{-8} specified in the requirements. Then, the periodicity of this orbit can be validated, as well as that of the rest of orbits, as it has been found that this orbit 1116 is the one showing less periodicity precision.

The values in the Monodromy matrices of orbits like this are very big, in the order of 10^8, so it is thought that precision is lost when computing the eigenvalues, as there are not enough decimals.

Chapter 5

Budget summary

In this chapter, the budget associated to all the costs related to the development of the present thesis and study during four months, from February to May of 2023, are stated, as well as the different costs that have been considered:

Concept	**Cost**
Human resources	4,571.52€
Hardware used	715.90€
Software used	87.34€
Electricity and Internet consumption	137.81€
TOTAL	5,512.57€

Table 5.1: Total costs for the budget of the thesis.

For further information regarding the different costs, check the *Budget* document that has been attached.

Chapter 6

Conclusions

In the present thesis, a large variety of possible transfer trajectories to reach the stability regions around L4 and L5 has been studied.

First of all, this stability region was computed, as well as the different types of orbits there, so any of them could be chosen as the destination for a spacecraft. It has been seen that when closer to L4 or L5 are the initial conditions of the spacecraft, smaller is the orbit around the libration point, i.e. it remains closer to L4 or L5. However, the energies of these PSD orbits are higher. Once these orbits were characterized, the departure Lyapunov orbits around L1 and L2 were studied. The objective was to drift away from them through their unstable invariant manifolds, so that the spacecraft could take advantage of the natural dynamics of the problem and, with that, make the transfers to L4 and L5 cheaper. Indeed, cheap trajectories have been found, but it has always been necessary to consider similar Jacobi constants both for the departure Lyapunov orbits and for the destination orbits in the stability region, which lead to find the most optimal transfers in terms of delta-V budget, thus fulfilling the objective of the present thesis.

It is also important to recall that different Jacobi constants for the departure Lyapunov orbits led to different velocities in the manifolds that where responsible of increasing or decreasing the time of flight. With that and imposing a mid-course correction maneuver, it has been seen that the times of flight can be reduced, although at higher delta-V budgets, in general.

However, the obtained times of flight as well as the delta-V budgets have been seen to be comparable to interplanetary missions, and although it is easier to get to L1 and L2 in terms of flight time, the stability regions around L4 and L5 do not require station-keeping maneuvers like in those collinear libration points. Therefore, taking into account the scientific interest of these regions and that the transfer trajectories are comparable to other interplanetary trajectories, the PSD around L4 and L5 offer great observation points to monitor the Sun and understand the variety of space weather events.

6.1 Future work

Finally, some proposals are going to be made regarding possible future work to improve the accuracy of the results as well as to offer a potentially better set of results:

- **Improve the precision of the Monodromy matrices:** In Section 4.2, it has been said that not all eigenvalues of the Monodromy matrices of the Lyapunov orbits that have to be 1 actually are. In order to increase the precision of the Monodromy matrices values, different approaches can be taken:
  - Use quadruple precision (or more precision than the double precision used in the codes of the present thesis) to compute the Monodromy matrices and, with them, their eigenvalues and eigenvectors.
  - Match the periodicity of the Lyapunov orbit at different locations and not only after one period. With that, a more accurate periodicity would be achieved, thus resulting in more accurate Monodromy matrices.
- **Parameterize the different set of PSD orbits, Lyapunov orbits and unstable manifolds:** With that, more interesting and optimal transfer trajectories may be found, as with the manual procedure to find the aiming points where both manifold trajectory and PSD orbit are tangential some better locations may have been lost. Defining an algorithm including the parameterization of the orbits would be useful to automatically find the most optimal and cheapest transfer trajectories to L4 and L5.
- **Implement more mid-course impulses or find the most optimal place:** In order to make more efficient impulses while reducing the time of flight, it may be necessary to perform more impulses during the transfer. The most suitable location to perform these impulses should also be studied.

References

1. URRUTICOECHEA, Aitor. *Study and optimization of transfer orbits to the L4 and L5 Lagrange Points of the Earth-Sun system.* [online]. Bachelor final thesis, UPC, Escola Superior d'Enginyeries Industrial, Aeroespacial i Audiovisual de Terrassa, 2023. [Visited on 21/02/2023]. Available from: http://hdl.handle.net/2117/384831.
2. FARRÉS, Ariadna; HEILIGERS, Jeannette; MIGUEL, Narcís. Road map to L_4/L_5 with a solar sail. *Aerospace Science and Technology.* 2019, vol. 95, pp. 105–458. Available from DOI: https://doi.org/10.1016/j.ast.2019.105458.
3. Encyclopaedia Britannica. *Kepler's laws of planetary motion* [online]. November 2022. [Visited on 26/01/2023]. Available from: https://www.britannica.com/science/Keplers-laws-of-planetary-motion.
4. WEISSTEIN, Eric W. *Restricted Three-Body Problem.* [online]. Wolfram Research. [Visited on 26/01/2023]. Available from: https://scienceworld.wolfram.com/physics/RestrictedThree-BodyProblem.html.
5. ESA. *What are Lagrange points?* [online]. [Visited on 27/01/2023]. Available from: https://www.esa.int/Enabling_Support/Operations/What_are_Lagrange_points.
6. NASA/WMAP Science Team. *What is a Lagrange point?* [online]. March 2018. [Visited on 27/01/2023]. Available from: https://solarsystem.nasa.gov/resources/754/what-is-a-lagrange-point/.
7. SPANNER, Holly. *What are Lagrange points?* [online]. Science Focus, February 2022. [Visited on 27/01/2023]. Available from: https://www.sciencefocus.com/space/lagrange-points/.
8. FARRÉS, Ariadna; BAÑOS, Narcís Miguel. Solar Sailing at the L4/L5 libration points. *AAS/AIAA Astrodynamics Specialist Conference* [online]. Stevenson, WA: 2017, vol. AAS 17-711 (Preprint). [Visited on 22/02/2023]. Available from: https://www.researchgate.net/publication/319875131_Solar_Sailing_at_the_L4L5_libration_points.
9. Encyclopaedia Britannica. *Newton's law of gravitation* [online]. November 2022. [Visited on 26/01/2023]. Available from: https://www.britannica.com/science/Newtons-law-of-gravitation.
10. SENGUPTA, Argha. *What Is The Three-Body Problem And Why Is It Hard To Solve?* [online]. ScienceABC, February 2022. [Visited on 26/01/2023]. Available from: https://www.scienceabc.com/pure-sciences/what-is-the-three-body-problem-and-why-is-it-hard-to-solve.html.

11. MONTGOMERY, Richard. *The Three-Body Problem*. [online]. Scientific American, August 2019. [Visited on 26/01/2023]. Available from: `https://www.scientificamerican.com/article/the-three-body-problem`.
12. WEBER, Bryan. *Circular Restricted Three-Body Problem*. [online]. Orbital Mechanics & Astrodynamics. [Visited on 26/01/2023]. Available from: `https://orbital-mechanics.space/the-n-body-problem/circular-restricted-three-body-problem.html`.
13. NSSDCA. *Planetary Fact Sheet - Metric* [online]. [Visited on 17/06/2023]. Available from: `https://nssdc.gsfc.nasa.gov/planetary/factsheet/`.
14. WALTER, Ulrich. *Astronautics: The Physics of Space Flight*. [online]. Third edition. [N.d.]. Springer International Publishing AG, March 2019. [Visited on 26/01/2023]. ISBN 9783319743738. Available from: `https://ebookcentral-proquest-com.recursos.biblioteca.upc.edu/lib/upcatalunya-ebooks/detail.action?pq-origsite=primo&docID=6313075`.
15. Wikipedia. *List of objects at Lagrange points* [online]. [Visited on 30/01/2023]. Available from: `https://en.wikipedia.org/wiki/List_of_objects_at_Lagrange_points`.
16. Wikipedia. *Wind (spacecraft)* [online]. [Visited on 30/01/2023]. Available from: `https://en.wikipedia.org/wiki/Wind_(spacecraft)`.
17. Wikipedia. *Gaia (spacecraft)* [online]. [Visited on 30/01/2023]. Available from: `https://en.wikipedia.org/wiki/Gaia_(spacecraft)`.
18. NASA Goddard Space Flight Center. *Nancy Grace Roman Space Telescope* [online]. [Visited on 17/06/2023]. Available from: `https://roman.gsfc.nasa.gov/`.
19. BRIDGMAN, Tom; SHIRAH, Greg; KAISER, Michael; KUCERA, Therese. *STEREO Visits the Lagrange Points - L4 and L5*. [online]. NASA Scientific Visualization Studio, April 2009. Reviewed on March 2021 [Visited on 19/06/2023]. Available from: `https://svs.gsfc.nasa.gov/3591`.
20. Wikipedia. *STEREO* [online]. [Visited on 30/01/2023]. Available from: `https://en.wikipedia.org/wiki/STEREO`.
21. Wikipedia. *ESA Vigil* [online]. [Visited on 30/01/2023]. Available from: `https://en.wikipedia.org/wiki/ESA_Vigil`.
22. CURTIS, Howard D. *Orbital Mechanics for Engineering Students*. [online]. Second edition. [N.d.]. Butterworth-Heinemann, 2010. [Visited on 26/01/2023]. ISBN 9780123747785. Available from: `https://www.sciencedirect.com/book/9780123747785/orbital-mechanics-for-engineering-students`.
23. KOON, Wang Sang; LO, Martin W.; MARSDEN, Jerrold E.; ROSS, Shane D. *Dynamical Systems, The Three-Body problem, and Space Mission Design*. [online]. [N.d.]. Marsden Books, October 2022. [Visited on 10/04/2023]. ISBN 9780615240954. Available from: `https://www.researchgate.net/publication/328913173_Dynamical_Systems_the_Three-Body_Problem_and_Space_Mission_Design`.
24. NSSDCA. *Sun Fact Sheet* [online]. [Visited on 04/03/2023]. Available from: `https://nssdc.gsfc.nasa.gov/planetary/factsheet/sunfact.html`.
25. NSSDCA. *Earth Fact Sheet* [online]. [Visited on 04/03/2023]. Available from: `https://nssdc.gsfc.nasa.gov/planetary/factsheet/earthfact.html`.

26. JPL. *JPL Solar System Dynamics* [online]. California Institute of Technology. [Visited on 03/03/2023]. Available from: `https://ssd.jpl.nasa.gov/`.
27. SIMÓ, C.; SOUSA-SILVA, P.; TERRA, M. Practical Stability Domains Near $L_{4,5}$ in the Restricted Three-Body Problem: Some Preliminary Facts. In: IBÁÑEZ, S.; PÉREZ DEL RÍO, J.; PUMARIÑO, A.; RODRÍGUEZ, J. *Progress and Challenges in Dynamical Systems. Springer Proceedings in Mathematics & Statistics* [online]. Springer, July 2013, vol. 54, pp. 367-382. [Visited on 22/02/2023]. ISBN 978-3-642-38830-9. Available from DOI: `https://doi.org/10.1007/978-3-642-38830-9_23`.
28. ROVIRA, Adrià. *Space Engineering - Module 3: Astrodynamics.* [online]. 2022. Notes from the Space Engineering subject of the Aerospace Technology Engineering degree, taught in ESEIAAT, UPC. [Visited on 30/01/2023].
29. WEISSTEIN, Eric W. *Newton's Method.* [online]. Wolfram MathWorld [Visited on 17/04/2023]. Available from: `https://mathworld.wolfram.com/NewtonsMethod.html`.
30. ESA. *Juice factsheet* [online]. [Visited on 18/06/2023]. Available from: `https://www.esa.int/Science_Exploration/Space_Science/Juice_factsheet`.
31. ESA. *JUpiter ICy moons Explorer. Exploring the emergence of habitable worlds around gas giants.* [online]. Definition Study Report ESA/SRE(2014)1. September 2014. [Visited on 18/06/2023]. Available from: `https://sci.esa.int/documents/33960/35865/1567260128466-JUICE_Red_Book_i1.0.pdf`.
32. JPL. *Cassini-Huygens* [online]. California Institute of Technology. [Visited on 18/06/2023]. Available from: `https://www.jpl.nasa.gov/missions/cassini-huygens`.
33. NASA. *Cassini* [online]. [Visited on 18/06/2023]. Available from: `https://www.nasa.gov/mission_pages/cassini/main/index.html`.
34. NASA. *Juno* [online]. [Visited on 18/06/2023]. Available from: `https://www.nasa.gov/mission_pages/juno/main/index.html`.
35. NASA. *OSIRIS-REx* [online]. [Visited on 18/06/2023]. Available from: `https://www.nasa.gov/osiris-rex`.
36. University of Arizona. *Word of the Week: Delta-V* [online]. asteroidmission.org. [Visited on 18/06/2023]. Available from: `https://www.asteroidmission.org/galleries/word-of-the-week/wotw-delta-v/`.
37. NASA Goddard Space Flight Center. *James Webb Space Telescope* [online]. [Visited on 18/06/2023]. Available from: `https://webb.nasa.gov/`.
38. MathWorks. *ode89* [online]. [Visited on 18/06/2023]. Available from: `https://www.mathworks.com/help/matlab/ref/ode89.html`.
39. MathWorks. *ode78* [online]. [Visited on 18/06/2023]. Available from: `https://www.mathworks.com/help/matlab/ref/ode78.html`.
40. MathWorks. *Choose an ODE solver* [online]. [Visited on 18/06/2023]. Available from: `https://www.mathworks.com/help/matlab/math/choose-an-ode-solver.html`.